

# **Precise Measurement of the Neutron Skin Thickness of $^{208}Pb$ and $^{48}Ca$**

A Dissertation Presented

by

**Weibin Zhang**

to

The Graduate School

in Partial Fulfillment of the Requirements

for the Degree of

**Doctor of Philosophy**

in

**Physics**

Stony Brook University

June 2022

**Stony Brook University**

The Graduate School

**Weibin Zhang**

We, the dissertation committee for the above candidate for the Doctor of Philosophy degree, hereby recommend acceptance of this dissertation.

Abhay Deshpande – Dissertation Advisor  
Professor, Department of Physics and Astronomy

Joanna Kiryluk – Chairperson of Defense  
Professor, Department of Physics and Astronomy

James M. Lattimer  
Professor, Department of Physics and Astronomy

Name of Outside Member  
Position  
Institution

This dissertation is accepted by the Graduate School.

Eric Wertheimer  
Dean of the Graduate School

Abstract of the Dissertation

**Precise Measurement of the Neutron Skin Thickness  
of  $^{208}Pb$  and  $^{48}Ca$**

by

**Weibin Zhang**

**Doctor of Philosophy**

in

**Physics**

Stony Brook University

2022

text of abstract

# Contents

<b>List of Figures</b>	<b>vi</b>
<b>Acknowledgements</b>	<b>xi</b>
<b>1 Introduction</b>	<b>2</b>
1.0.1 Neutron Radius and Neutron Skin . . . . .	2
1.0.2 Theoretical Models . . . . .	6
1.1 Symmetry Energy . . . . .	9
1.2 Physics Beyond the Standard Model (SM) . . . . .	13
1.3 Asymmetry . . . . .	14
1.4 Dynamics . . . . .	20
1.5 Why Pb and Ca . . . . .	21
<b>2 Experimental Setup</b>	<b>23</b>
2.1 Kinematics . . . . .	25
2.1.1 Figure Of Merits (FOM) . . . . .	26
2.2 Continuous Electron Beam Accelerator Facility (CEBAF) . . . . .	29
2.3 Polarized Electron . . . . .	32
2.3.1 Polarized Electron Source . . . . .	32
2.3.2 Polarization Control . . . . .	34
2.3.3 Polarimeters . . . . .	39
2.4 Monitors . . . . .	44
2.4.1 BPMs . . . . .	44
2.4.2 BCMs . . . . .	45
2.4.3 SAMs . . . . .	47
2.4.4 Beam Modulation . . . . .	47
2.5 Target . . . . .	48
2.5.1 Target Cooling . . . . .	50
2.5.2 Raster . . . . .	50
2.5.3 Beamline Collimator and Sieve Slit Collimators . . . . .	52
2.5.4 Septum . . . . .	53
2.5.5 High Resolution Spectrometer (HRS) . . . . .	54
2.5.6 Detector Package . . . . .	54
2.5.7 Data AcQuisition (DAQ) . . . . .	59

<b>3 Data Analysis</b>	<b>60</b>
3.1 Raw Data . . . . .	63
3.1.1 Measured Asymmetry . . . . .	63
3.1.2 Beam False Asymmetry . . . . .	63
3.2 Regression . . . . .	64
3.2.1 The Model . . . . .	64
3.3 Beam Modulation . . . . .	66
3.4 Lagragian . . . . .	66
3.5 Correction . . . . .	66
3.6 Result . . . . .	66
<b>4 Transverse Asymmetry</b>	<b>67</b>
4.1 Motivation for Transverse Asymmetry . . . . .	67
4.2 How to Measure the Transverse Asymmetry: the Method . . . . .	72
4.3 The Result . . . . .	72
4.4 Accptance Function . . . . .	73
4.4.1 Transportation Matrix . . . . .	73
4.4.2 Scattering Angle $\theta_{lab}$ . . . . .	75
4.4.3 Data . . . . .	76
4.4.4 Simulation . . . . .	78
<b>5 Results</b>	<b>84</b>
5.1 Polarization . . . . .	84
5.1.1 Moller . . . . .	84
5.1.2 Compton . . . . .	84
5.2 Final Number . . . . .	84
5.3 Physical Implication . . . . .	84
5.3.1 Theoretical Models . . . . .	84
5.3.2 Saturation Density . . . . .	85
5.4 Neutron Stars . . . . .	86
<b>Bibliography</b>	<b>87</b>
<b>A Symmetry Energy</b>	<b>93</b>
A.1 Resource . . . . .	93

# List of Figures

1.1	Characristic of FF w.r.t. different density distribution functions . . . . .	5
1.2	As we can see, the virtual photon wave absorbed by a nucleon at position $\mathbf{r}$ will travel a further distance $\mathbf{q} \cdot \mathbf{r}$ than the one absorbed at the central point, therefore a phase difference $e^{i\mathbf{q}\mathbf{r}/\hbar}$ . . . . .	7
1.3	Left: Mott cross section of electron elastically scattered off a Ca48 target. Parameters: $p = E = 757.5 \text{ MeV}$ . Middle: cross section of electron elastically scattered off Ca48 with the hard ball model (1.0.2). Parameters: $E = 757.5 \text{ MeV}$ , $R = A^{1/3} \text{ fm}$ . Right: experimental values (dots) and theoretical prediction (solid line), their calculation assumed the charge distribution as a Fermi 3-parameter function. $\rho(r) = \frac{\rho_0(1+\omega r^2/c^2)}{1+\exp((r-c)/a)}$ . The $^{48}\text{Ca}$ ( $^{40}\text{Ca}$ ) cross sections are multiplied by $10^{-1}$ (10) to seperate them. [1]	8
1.4	In nuclear Shell Model, it is assumed that nucleons occupy different eigenstates of the same spherically symmetric average potential. This potential, unlike that in atomic shell model, needed to be guessed. It turns out that the Saxon-Woods model is a good candidate: $V(r) = -\frac{V(0)}{1+\exp((r-c)/a)}$ (c is the half-height raidus and a represents diffuseness of the distribution). Because the potential is formed by all nucleons, so it is approximatively proportional to the nucleon density, therefore the same distribution for nucleon density. . . . .	8
1.5	PV asymmetry for $^{208}\text{Pb}$ and $^{48}\text{Ca}$ versus scattering angle at 850 MeV (Coulomb distortion correction included). The dotted curve assumes the same weak and charge distribution, while the solid curve is based on relativistic Mean Field Densities. The dashed curve in $^{208}\text{Pb}$ plot uses 3 parameter Fermi distribution [2] . . . . .	9
1.7	Fermi's interpretation of beta decay, current $j_{n \rightarrow p}$ convert n into p and current $j_{\nu_e \rightarrow e}$ creates $(e, \bar{\nu}_e)$ pair. . . . .	14
1.8	W-boson exchange picture of $\beta$ decay . . . . .	16
1.9	Nuclear Landscape . . . . .	21

2.1	Evolution of PVES experiments, solid lines represent the relative precision. Generation I experiments (E122 (1978) [3], MIT-12C (1989) [4] and Mainz-Be (1990) [5]) did pioneering work to pave the way for PVES. Generation II experiments (the SAMPLE collaboration [6] at the MIT-Bates accelerator, the G0 [7] and HAPPEX [8] collaboration at Jefferson Lab and the A4 collaboration [9] at the Maizer Mikrotron (MAMI) accelerator) were devoted to the exploration of strange FFs in nucleons. Generation III experiments (E158 at SLAC [10], Qweak [11] and PVDIS [12]) tested the SM at low energy and measured the neutron skin thickness of nuclei (PREX-I/II and CREX). The planned Generation IV experiments (SoLID program [13] and M OLLEr experiment [14] at JLab, P2 experiment on the future Mainz Energy-recovery Superconducting Accelerator (MESA) [15]) will continue to test the SM and explore the structure of nucleons with higher precisions. (MESA-12C is the same experiment as MESA-P2 with a different $^{12}\text{C}$ target) . . . . .	24
2.2	Scattering rate versus beam energy and scattering angle for $^{208}\text{Pb}$ and $^{48}\text{Ca}$ , the energy and scattering angle are design values. We see that rate falls quickly along both beam energy and scattering angle for both nuclei, so one would like small beam energy and small scattering angle (equivalently small $\mathbf{q}$ ) for large scattering rate. . . . .	28
2.3	Asymmetry and sensitivity plot for $^{208}\text{Pb}$ , which increases along beam energy and oscillating up along scattering angle. The sensitivity plot is calculated with 1% change in neutron radius and it shows the absolute value. So in small scattering angle region, there is a local maximum around $6^\circ$ . . . . .	29
2.4	Asymmetry and sensitivity plot for $^{48}\text{Ca}$ , the asymmetry maximize around 2500 MeV and there is a local maximum about $4.5^\circ$ . As for sensitivity, there is regional maximum around $5^\circ$ . . . . .	29
2.5	For both nuclei, FOM supports a small scattering angle. As for beam energy, FOM maximize around 950 (2200) GeV for $^{208}\text{Pb}$ ( $^{48}\text{Ca}$ ). . . . .	29
2.6	Aerial view of JLab accelerator site, yellow line tells the position of the CEBAF accelerator and the 3 experimental halls are marked out as A/B/C (Hall D locates on the top left corner, after the exit of north LINAC). The accelerator tunnel is 30 feet ( $\sim 9\text{ m}$ ) underground and 10 feet ( $\sim 3\text{ m}$ ) high, with a circumference of about 7/8 miles (1.4 km). There are 2 superconducting LINAC (red lines), each of 1/4 miles (400 m). The pink part on the mid left is the location of injector. The right 2 plots show the tunnel and experimental halls under construction. . . . .	30
2.7	Schematic plot of CEBAF. Low energy beams will be kicked into higher arc, and high energy beams will go through lower arc. The magnetic field increases from higher arc to lower arc to keep electron trajectory have the same radius. . . . .	31

2.8	3D and bird view of Hall A [16]. Originally, they were called High Resolution Hadron Spectrometer (HRHS) and High Resolution Electron Spectrometer (HRES), but they are essentially identical to each other and can be used interchangeably. so now they are called left arm (HRS-L) and right arm HRS (HRS-R) . . . . .	32
2.9	Excitation of polarized electrons . . . . .	33
2.10	The energy band diagram of GaAs near its surface. Left: bare p-type GaAs, the large positive electron affinity (PEA) prevents electrons from escaping the surface; Middle: p-type GaAs with a cesiated surface, the electron affinity (EA) is 0, but electrons still can't escape the surface easily; Right: GaAs with layer of cesium oxide; the electron vacuum energy $E_\infty$ is lowered to make a negative EA so that electrons can break free the surface easily. [17] . . . . .	33
2.11	Strained GaAs . . . . .	34
2.12	The laser system at the CEBAF injector . . . . .	35
2.13	How the laser table actually looks like . . . . .	36
2.14	Phase shift by going through the PC . . . . .	36
2.15	Schematic plot of double wien filter, electron beam travels from left to right. [18] . . . . .	38
2.16	Schematic plot of the Mott polarimeter, it has 4 symmetric detector ports (up and down, left and right – which is not shown in the plot). The back scattering angle is $172.6^\circ$ , where we have the highest analyzing power from theoretical calculation of the Sherman function. [19] . . . . .	39
2.17	The Sherman Function for different high-Z targets at 5 MeV, dots represent experimental measurement. . . . .	40
2.18	Left: Compton Chicane [20]; Right: Schematic plot of electron/photon scattering . . . . .	41
2.19	The Compton analyzing power increases with electron energy. Note that the analyzing power will change sign at $\rho \sim 0.5$ for both PREX-II and CREX beam energies. . . . .	42
2.20	Moller Polarimeter . . . . .	43
2.21	Schematic plot of Hall A beam monitor system and beam modulation system . . . . .	44
2.22	Schematic plot of stripline BPM . . . . .	45
2.23	Hall A BCM system [21] . . . . .	46
2.24	Up: Schematic plot of current convertor; Down: $TM_{010}$ and $TM_{110}$ modes, the red arrows are electric field . . . . .	46
2.25	Layout of SAMs[?] . . . . .	47
2.26	Scattering chamber of PREX-II/CREX . . . . .	49
2.27	Production target ladder and calibration ladder . . . . .	49
2.28	Raster pattern with different frequency difference between X and Y. Left: $ f_y - f_x  = 120\ Hz$ ; Right: $ f_y - f_x  = 8 * 120\ Hz$ . The raster shape is a $4 \times 4\ mm$ square. . . . .	51
2.29	Picture of Pb targets after running, one can see clearly the shape of raster. . . . .	51
2.30	How the target temperature change with size of raster area. . . . .	51

2.31	Side and top view of beamline collimator. Beam from left to right. . . . .	52
2.32	Left: a simple model of target degradation – assumming the inner foil ( $t_1$ ) is becoming thinner and the outer foil is becoming thicker ( $t_2$ ) while the total mass keeps intact. The plot showes how the power deposition on the beamline collimator change in this model. Middle and Right: actual neutron and photon radiation level monitored along charge accumulation. They show similar trends. . . . .	53
2.33	Front picture of beamline collimator and sieve slit collimators, looking downstream. One can clearly see a cylinder removed from the central collimator. The sieve planes lie after the beamline collimator and are movable like a door, it can be opened or closed remotely. . . . .	53
2.34	Left: septum (the red coils) in the pivot region; Right: picture of septum. . . . .	54
2.35	Schematic plot of HRS and particle rays inside it. [22] The 'focal plane' in the middle plot, by design, should be at an angle of $45^\circ$ w.r.t the central ray, but is actually rotated to $70^\circ$ due to lackness of sextupole winding in Q3. When we talk about the HRS focal plane, we usually refer to the VDC lower plane. . . . .	55
2.36	Picture of Q1 collimator pairs . . . . .	55
2.37	The detector package . . . . .	56
2.38	Schematic plot of VDCs showing UV wires [23] . . . . .	56
2.39	Left: CAD drawing of the quartz detector; Middle: schematic plot of Cherenkov radiation, the angle between electron and the Cherenkov radiation is $\cos \theta = \frac{v_c}{v_e} = \frac{c}{nv_e} = \frac{1}{n\beta} \approx \frac{1}{n}$ ; Right: electron flux goes through a quartz detector. . . . .	57
2.40	Simulation result of photo-electron (PE) spectrum for single electron passing through the main detectors. The wider tail in the downstream detector is due to particle showering in the upstream quartz. Plot from Devi Adhikari. . . . .	58
2.41	Data of x,y distribution on quartz. Plots from Devi Adhikari. . . . .	58
2.42	Scatter plot of electrons on the AT monitor plane. Red and blue represent events with opposite transverse polarization. . . . .	59
3.1	Charge accumulation versus time (left) and run number (right). The long plateau on the left plot is due to Covid shutdown, which is shown around run 7500 on the right plot. We see that data taking is most efficient after AT (before Covid), the last month (after Covid) is not bad while the first 2 months is not so efficient due to various problems. . . . .	61
3.2	Statistics of CREX runs . . . . .	61
3.3	For CREX, $t_{\text{settle}} = 90 \mu\text{s}$ , to allow the PC stablizes after flipping, avoiding any cross effect from last helicity state. The deputy factor is 98.92%. . . . .	62
4.1	Left: Feynman plot of transversely polarized electron scatter off unpolarized nuclei target; Right: Time reversed image of Left plot. . . . .	71
4.2	Transportation plot of HRS. One can clearly see the dispersion effect due to shift in momentum ( $\delta$ ) in the Dipole area and the convergent effect of Q3. . . . .	75

4.3	Schematic plot of HCS and TCS. The Hall center is the origin of the HCS, but the target doesn't necessary lie in the Hall center. The distance from the Hall center to the sieve plane L is constant, which is used to identify the origin of the TCS. In ideal case, the origins of both coordinate systems will overlap. . . . .	76
4.4	Schematic plot of vertex and apparent quantities. . . . .	76
4.5	Sieve pattern plots for -10% septum current and varied Q1 current, from left to right: -10%, nominal and +10% Q1 current. With different Q1 current, the sieve pattern twist, and the central hole shifts in $\theta$ , so the septum current is not a good value. . . . .	77
4.6	Sieve pattern plots for nominal (scaled from PREX-II setting) septum current and varied Q1 current, from left to right: -10%, nominal and +10% Q1 current. Top row is right arm and bottom row is left arm. With different Q1 current, the sieve pattern twist, but the central hole keeps at the same position, which means the central ray goes through the axis of the HRS. . .	78
4.7	Inner edge search on the left arm. Septum current from top left to bottom right: +2.5%, +5%, +7.5%, +10%. The inner middle hole starts to appear since +5%, and outer holes disappear since 7.5%, so the best septum current was chosed to be +5% . . . . .	79
4.8	Sieve plot of CREX tune. Centered at (-0.3, -1.5), the new beam position for the new target. . . . .	79
4.9	Sieve pattern plots from simulation with different septum current. . . . .	81
4.10	Position of the pinch point and the Q1 collimator. . . . .	81
4.11	Ratio of simulation to data average value for $\theta_{lab}$ , $Q^2$ and $\mathcal{A}$ . Top (bottom) row for left (right) arm. . . . .	82
4.12	$\theta_{lab}$ and $Q^2$ comparesion between best models and data (apparent values). . . . .	83
4.13	Acceptance function extraced using the best models. . . . .	83

# Acknowledgements

text of acknowledgement

**Remember to remove it after completing your thesis.**

- pdfpageheight (pdfforwidth) – 598.14806pt(845.90042pt) – page height and width
- baselineskip – 15.0pt – vertical distance between two nearby lines; set it to change line gap
- left (right) margin –

# Chapter 1

## Introduction

The Pb Radius EXperiment-II (PREX-II) and Ca48 Radius EXperiment (CREX) are high-precision experiments that measure the tiny parity-violating (PV) asymmetry (at part per million (ppm) level) of longitudinally polarized electrons scattered off neutron-rich targets ( $^{208}\text{Pb}$  and  $^{48}\text{Ca}$ ), from which the weak form factors, weak charge and neutron distribution, and finally neutron skin thickness of those nuclei will be extracted.

The PV asymmetry ( $\mathcal{A}_{pv}$ ) comes from the interference between the electromagnetic (EM) and (neutral) weak one-boson exchange amplitude, because weak interaction doesn't conserve the parity symmetry. While the EM interaction has been studied thoroughly, the asymmetry measurement allows us to derive the weak charge and therefore the neutron distribution in a nucleus.

Parity-violating electron scattering (PVES) experiments require high energy polarized electron beam, which was provided by the Continuous Electron Beam Accelerator Facility (CEBAF) at Thomas Jefferson National Accelerator Facility (TJNAF, also known as JLab). The excellent beam qualities and dedicated instrumentations at JLab allowed the measurements to be statistics limited.

### 1.0.1 Neutron Radius and Neutron Skin

What's the size of a nucleus? Given the development of modern physics, many people may think there is a clear answer to this basic question. Unfortunately, we don't. Of course, one may estimate a nuclear radius as  $R = cA^{1/3}$ , where  $A$  is the mass number and  $c$  is an approximative constant coefficient that can be experimentally identified ( $\sim 1.20 \text{ fm}$  [?]). But this picture is over simplified and can't help in cases where precise nucleon distribution is needed. Physicists do have calculated and precisely measured the proton radius of many nuclei, but neutron, due to its neutrality, remains as a stubborn obstacle in our understanding toward the structure of nuclei. Especially for heavy nuclei, where more neutrons than protons are needed to bound the nuclei, it is neutron radius rather than proton radius that defines the size of a heavy nucleus.

When we talk about the proton or neutron radius, it is actually a concept under the framework of Quantum Mechanics (QM), rather than the radius of any objects that we

are familiar with in our daily life. In QM, particles are represented by a probability wave function, so the neutron (proton) Root-Mean-Square (RMS) radius is defined as:

$$R_{p,n} \equiv \langle R_{p,n}^2 \rangle^{1/2} = \sqrt{\frac{\int d^3\mathbf{r} r^2 \rho_{p,n}(\mathbf{r})}{\int d^3\mathbf{r} \rho_{p,n}(\mathbf{r})}} \quad (1.1)$$

where  $\rho(\mathbf{r})$  is the nucleon density at position  $\mathbf{r}$ , which satisfies the normalization condition:

$$\int d^3\mathbf{r} \rho_{p,n}(\mathbf{r}) = 1$$

Searching through the literatures, we can find many works on the high-precision (with an error  $\leq 0.02 \text{ fm}$ ) measurement of the proton (charge) radius ( $R_p$ ) of many nuclei through atomic and nuclear experiments [24, 25] but not much precise data about the neutron radius ( $R_n$ ). The difficulties lie in that neutrons are electrically chargeless, so one can measure its size only through strong or weak interaction. Both methods suffer from their own limitations: the weak interaction is too weak (compared to the background EM interaction) to measure it directly, therefore people turn to PV asymmetry measurement, which is also tiny, much effort is needed during experiments; while the strong interaction has large theoretical uncertainties from the low energy non-perturbative Quantum Chromodynamics (QCD), the interpretation of hadronic measurement is usually model dependent. Though of these difficulties, there have been many effort from the community to explore the different aspects of neutron radius (and neutron skin thickness): the hadronic probe includes pion [?], proton [?], antiproton [?] and alpha particle [?]; atomic experiments like electric dipole polarizabilities [?] and pygmy dipole resonances [?] also provide input to our understanding. Experimentally, the best resolution we got about  $R_n$  is about 5%. (FIXME) Theoretically, The best estimates of  $R_n$  appear to come from nuclear theory, where models have been constrained primarily by data other than measurements of neutron radii. Therefore, a measurement of  $R_n$  will provide a powerful independent check of basic nuclear theory.

Experimentally, the nucleon radius is measured from their corresponding form factors (FFs). According to QM, under Born approximation, the matrix element (ME) for a

scattering process is (assuming a Coulomb-like potential):

$$\begin{aligned}
\mathcal{M}_{fi} &= \langle \Psi_f | V(\mathbf{r}) | \Psi_i \rangle = \int e^{-i\mathbf{p}_f \cdot \mathbf{r}} V(\mathbf{r}) e^{i\mathbf{p}_i \cdot \mathbf{r}} d^3 \mathbf{r} \\
&= \int e^{i(\mathbf{p}_i - \mathbf{p}_f) \cdot \mathbf{r}} d^3 \mathbf{r} \int \frac{Q_t \rho(\mathbf{r}')}{4\pi |\mathbf{r} - \mathbf{r}'|} d^3 \mathbf{r}' \\
&= \int \int e^{i\mathbf{q} \cdot \mathbf{r}} \frac{Q_t \rho(\mathbf{r}')}{4\pi |\mathbf{r} - \mathbf{r}'|} d^3 \mathbf{r} d^3 \mathbf{r}' \\
&= \int \int e^{i\mathbf{q} \cdot (\mathbf{r} - \mathbf{r}')} \frac{Q_t \rho(\mathbf{r}')}{4\pi |\mathbf{r} - \mathbf{r}'|} e^{i\mathbf{q} \cdot \mathbf{r}'} d^3 \mathbf{r} d^3 \mathbf{r}' \\
&= \int e^{i\mathbf{q} \cdot \mathbf{R}} \frac{Q_t}{4\pi |\mathbf{R}|} d^3 \mathbf{R} \int \rho(\mathbf{r}') e^{i\mathbf{q} \cdot \mathbf{r}'} d^3 \mathbf{r}' \\
&= (\mathcal{M}_{fi})_{\text{point}} F(\mathbf{q})
\end{aligned} \tag{1.2}$$

where  $Q_t$  is the total charge. The ME can be factorized into two parts: the scattering amplitude of a point-like nucleus with charge  $Q_t$  and a modification due to the inner structure of the target, which is called the FF:

$$F(\mathbf{q}) = \int \rho(\mathbf{r}) e^{i\mathbf{q} \cdot \mathbf{r}} d^3 \mathbf{r} \tag{1.3}$$

which is just the Fourier transformation of the spatial density distribution. Conversely, once we know (measure) the FF at different  $\mathbf{q}$ , we can derive the charge distribution:

$$\rho(\mathbf{r}) = \int F(\mathbf{q}) e^{-i\mathbf{q} \cdot \mathbf{r}} d^3 \mathbf{q} \tag{1.4}$$

This tells us how to measure the charge density distribution of a nucleus:

$$F(\mathbf{q}) = \frac{\mathcal{M}_{fi}}{(\mathcal{M}_{fi})_{\text{point}}} = \sqrt{\frac{\sigma_{\text{measured}}}{\sigma_{\text{Mott}}}} \tag{1.5}$$

Though of many precise data points at different  $\mathbf{q}$  (most at low  $q$  region), there is obviously no way to cover the whole space of  $\mathbf{q}$  experimentally, therefore, some phenomenological models are needed to extract charge density distribution.

For a spherically symmetric density distribution,  $\rho(\mathbf{r}) = \rho(|\mathbf{r}|) = \rho(r)$ , one can calculate the corresponding FF as:

$$\begin{aligned}
F(\mathbf{q}) &= \int \rho(r) e^{iqr \cos \theta} 2\pi r^2 \sin \theta dr d\theta \\
&= 4\pi \int r \rho(r) \frac{\sin(qr)}{q} dr
\end{aligned}$$

One can see that for a Coulomb-like potential,  $F(\mathbf{q})$  doesn't depend on the direction of  $\mathbf{q}$ , but only its length:  $q$ , and for the convention of Lorentz Invariance, people usually

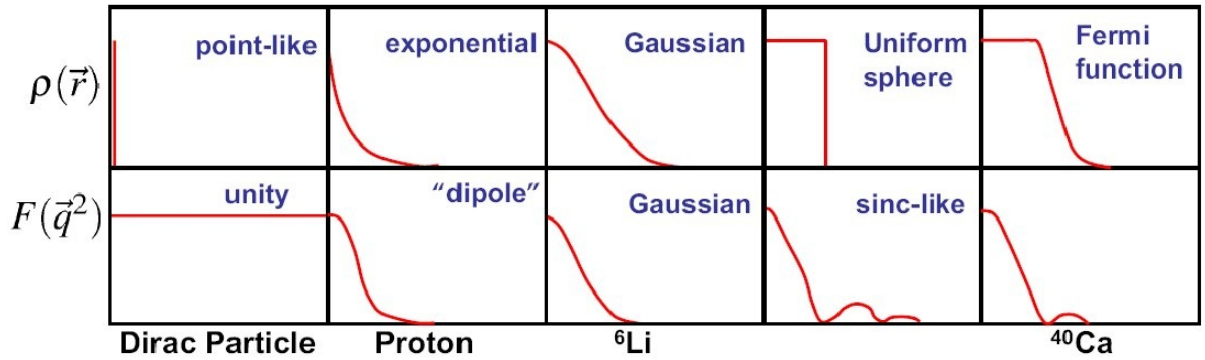


Figure 1.1: Characristic of FF w.r.t. different density distribution functions

write  $F$  in terms of  $Q^2 = -q^2$ , rather than  $q$ , so we will use  $F(q^2)$  or  $F(Q^2)$  hereafter.

Some typical spherically symmetric density distribution and their corresponding FFs are shown in Fig. ??.

At small  $q^2$  limitation, one can do the Fourier expansion:

$$\begin{aligned}
 F(q^2) &= 4\pi \int r\rho(r) \frac{\sin(qr)}{q} dr \\
 &= 4\pi \int \rho(r) r \left( r - \frac{1}{6}q^2 r^3 + \dots \right) dr \\
 &= \int \rho(r) \left( 1 - \frac{1}{6}q^2 r^2 + \dots \right) 4\pi r^2 dr \\
 &= 1 - \frac{1}{6}q^2 \langle r^2 \rangle + \dots \\
 &= F(0) + \left. \frac{dF}{dq^2} \right|_{q^2=0} \times q^2 + \dots
 \end{aligned}$$

and easily to get:

$$\langle R^2 \rangle = -6 \left. \frac{dF(q^2)}{dq^2} \right|_{q^2=0} \quad (1.6)$$

This equations prompts how to measure RMS radius: one can measure the FF at some low  $q^2$  points, extrapolate them to  $q^2 = 0$ , then the slope at  $q^2 = 0$  will be the RMS radius (that's why we use the RMS radius rather than the more physical definition of:  $\langle R \rangle = \int d^3r r \rho(r)$ ).

For charged proton, the FF will be the precisely measured EM FF:

$$\langle R_p^2 \rangle = -6 \left. \frac{dF_{EM}(q^2)}{dq^2} \right|_{q^2=0} \quad (1.7)$$

While neutron is neutral, we will measure its RMS radius from its weak charge distribu-

tion:

$$\langle R_n^2 \rangle = -6 \frac{dF_{weak}(q^2)}{dq^2} \Big|_{q^2=0} \quad (1.8)$$

The difference between them will be what we called the neutron skin thickness

$$R_{skin} = R_n - R_p \quad (1.9)$$

The neutron skin, as its name implies, is founded in neutron-rich isotopes that have more neutrons than protons. An intuitive picture is following: analog to atomic electron shell model, protons and neutrons also arrange themselves on shelves from low to high energy, without disturbing each other (nuclear shell model). The higher the energy level, the larger the orbit (radius). For most nuclei, they have similar number of proton and neutron, therefore an approximative proton and neutron radius. But for neutron-rich isotopes, the extra neutrons need to stay on higher energy shell after filling all low energy ones, forming a larger radius than proton and therefore the neutron skin.

Of course, this picture is too simple to fully understand the neutron skin. One quick question will be how can one ensure that the extra neutrons lies in the surface rather than the core area? That's related to the symmetry energy, more specifically, the density dependence of the symmetry energy. Because the core area has a higher nucleon density than the surface, and symmetry energy represents the penalty for breaking the proton-neutron symmetry: the higher the density, the larger the symmetry energy, therefore the lower the binding energy (the energy needed to break down a nuclear system:  $BE(N, Z) = M(N, Z)c^2 - Zm_p c^2 - Nm_n c^2$ ), the less stable the nuclei. So it is symmetry energy that pushes extra neutrons to the surface, which is the deeper reason for the formation of neutron skin.

Experimental hints of the existence of the neutron skin comes from optical isotope shifts (FIXME)

### 1.0.2 Theoretical Models

Though we don't know the actual neutron distribution, one would not expect too much difference between the proton and neutron distributions, and we know the proton distribution very well, through elastic ep scattering. The scattering cross section is:

$$\frac{d\sigma}{d\Omega} = \left( \frac{d\sigma}{d\Omega} \right)_{Mott} |F(q^2)|^2 \quad (1.10)$$

FF encodes information about the charge structure of a nucleon, it is an interference effect, finite size of the scattering center introduces a phase difference between different plane waves scattered from different points in space.

Consider the simplest hard ball model:

$$\rho(r) = \begin{cases} \frac{3}{4\pi R^3} & r \leq R \\ 0 & r > R \end{cases}$$

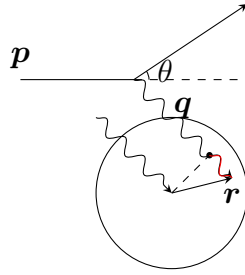


Figure 1.2: As we can see, the virtual photon wave absorbed by a nucleon at position  $\mathbf{r}$  will travel a further distance  $\mathbf{q} \cdot \mathbf{r}$  than the one absorbed at the central point, therefore a phase difference  $e^{i\mathbf{q}\mathbf{r}/\hbar}$

Then the FF will be:

$$F(q^2) = \frac{3}{(qR)^3} (\sin(qR) - qR \cos(qR))$$

where  $q = 2p \sin(\theta/2)$

Given the Mott cross section:

$$\left( \frac{d\sigma}{d\Omega} \right)_{Mott} = \begin{cases} \frac{Z^2 \alpha^2}{4E^2 \sin^4(\theta/2)} \cos^2(\theta/2) & \text{light nuclei } Z\alpha \ll 1 \\ \frac{Z^2 \alpha^2}{4E^2 \sin^4(\theta/2)} \cos^2(\theta/2) \left[ 1 + \pi Z \alpha \frac{\sin(\theta/2)(1 - \sin(\theta/2))}{\cos^2(\theta/2)} \right] & \text{medium nuclei} \end{cases} \quad (1.11)$$

We can draw the cross section, as a function of scattering angle in Fig. 1.3.

Well, the hard ball model doesn't reproduce the experimental distribution, it does characterize the real distribution and show us how FF modify the Mott cross section: the oscillating dips. As it turns out, a more realistic model will be the Saxon-Woods distribution (also called the Fermi 2-parameter model or the Fermi distribution):

$$\rho(r) = \frac{\rho(0)}{1 + \exp((r - R)/t)} \quad (1.12)$$

where  $R = (1.2A^{1/3} - 0.48) \text{ fm}$  denotes the nuclear force radius, and  $t = 0.4 - 0.5 \text{ fm}$  for  $A > 40$ . The right plot on Fig. 1.3 uses a fine tuned Fermi 3-parameter model, which fits quite well with the data. More detailed discussion about the Fermi distribution can be found in [26].

One theoretical model based on the Fermi distribution is the FSUGold [27], the neutron distribution of  $^{208}\text{Pb}$  predicted by FSUGold is shown in Fig. ??.

We also need to note that for medium and heavy nuclei, the Born approximation doesn't hold, where the incoming and outgoing waves are treated as plane waves. In reality, the waves are distorted by the intense nuclear EM field, making them no longer plane waves any more. So we have to take into account the Coulomb distortion effect, which will modify the PV asymmetry significantly. Coulomb distortion can be understood as multiple EM interactions with the same nucleus, so the distortion correction is

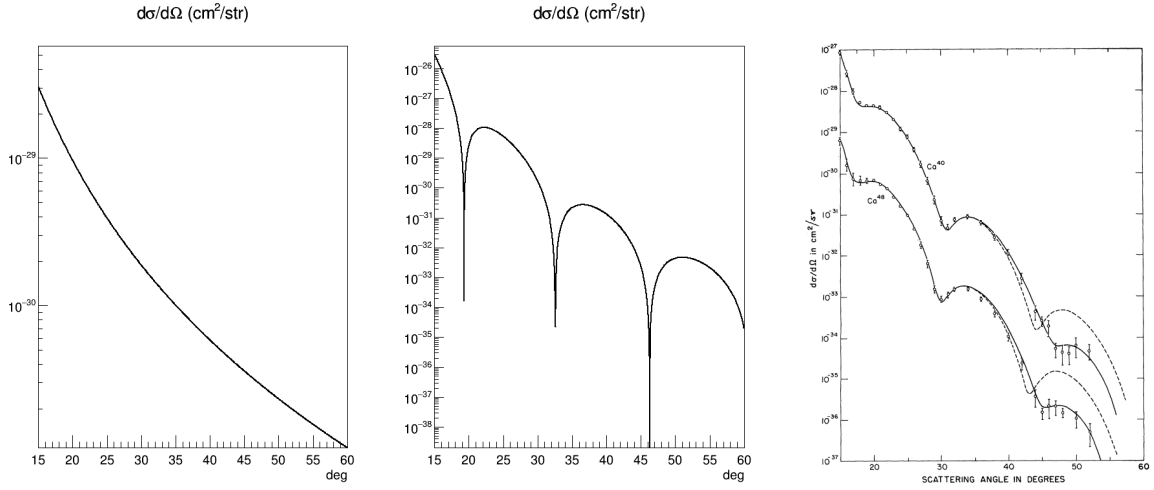


Figure 1.3: Left: Mott cross section of electron elastically scattered off a Ca48 target. Parameters:  $p = E = 757.5 \text{ MeV}$ . Middle: cross section of electron elastically scattered off Ca48 with the hard ball model (1.0.2). Parameters:  $E = 757.5 \text{ MeV}$ ,  $R = A^{1/3} \text{ fm}$ . Right: experimental values (dots) and theoretical prediction (solid line), their calculation assumed the charge distribution as a Fermi 3-parameter function.  $\rho(r) = \frac{\rho_0(1+\omega r^2/c^2)}{1+\exp((r-c)/a)}$ . The  $^{48}\text{Ca}$  ( $^{40}\text{Ca}$ ) cross sections are multiplied by  $10^{-1}$  ( $10$ ) to separate them. [1]

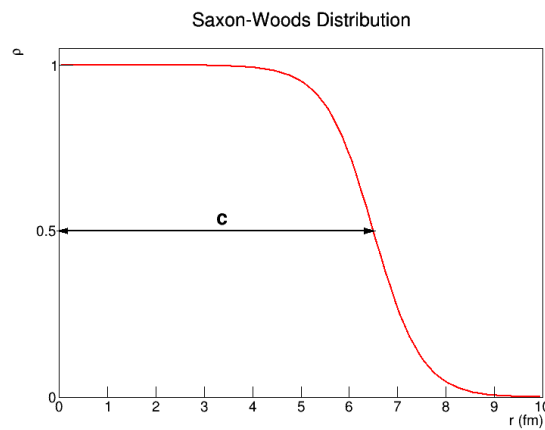
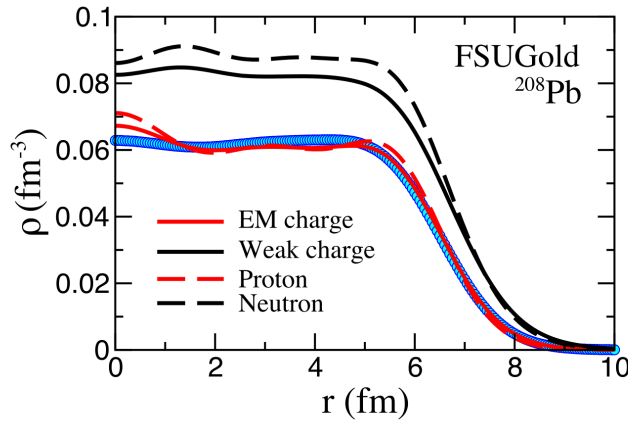


Figure 1.4: In nuclear Shell Model, it is assumed that nucleons occupy different eigenstates of the same spherically symmetric average potential. This potential, unlike that in atomic shell model, needed to be guessed. It turns out that the Saxon-Woods model is a good candidate:  $V(r) = -\frac{V(0)}{1+\exp((r-c)/a)}$  ( $c$  is the half-height radius and  $a$  represents diffuseness of the distribution). Because the potential is formed by all nucleons, so it is approximatively proportional to the nucleon density, therefore the same distribution for nucleon density.



proportional to  $Z\alpha$ . Obviously, this correction is more important for  $^{208}\text{Pb}$  because of its large  $Z$  value, Coulomb distortion could reduce the PV asymmetry by as much as 30% as we can see in the following plots.

With these information, one is able to solve the Dirac equation directly to know the PV asymmetry, as shown in the following 2 plots:

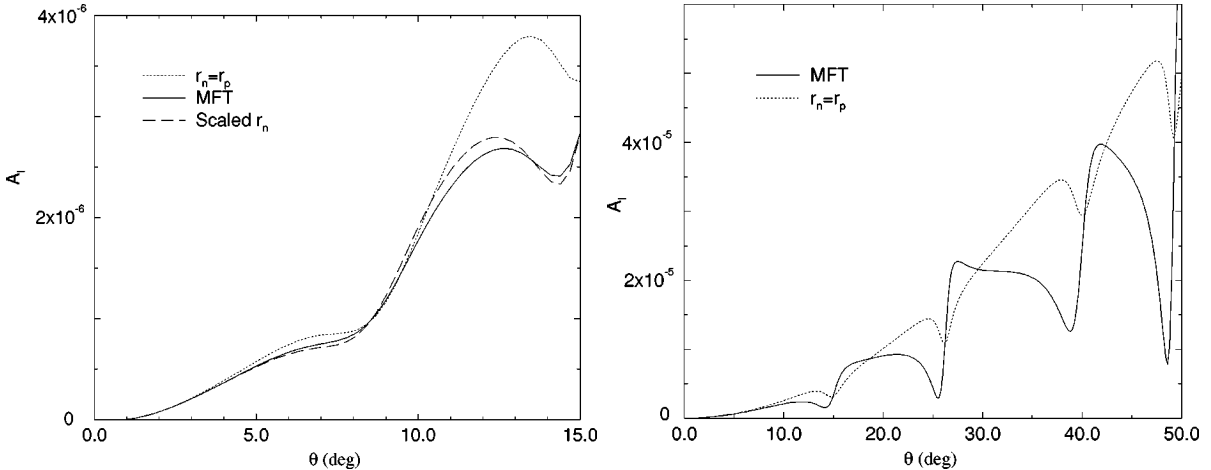


Figure 1.5: PV asymmetry for  $^{208}\text{Pb}$  and  $^{48}\text{Ca}$  versus scattering angle at 850 MeV (Coulomb distortion correction included). The dotted curve assumes the same weak and charge distribution, while the solid curve is based on relativistic Mean Field Densities. The dashed curve in  $^{208}\text{Pb}$  plot uses 3 parameter Fermi distribution [2]

## 1.1 Symmetry Energy

It has long been a hot topic for nuclear scientists to study how the asymmetry between number of proton and nucleon will affect nuclei, especially the binding energy, which hints us the limit of new isotope elements. Using the simplest Liquid Drop Model (LDM), we

will get the Bethe-Weizsacker Semi-empirical Mass Formula:

$$E \text{ (MeV)} = a_V A - a_S A^{2/3} - a_C \frac{Z(Z-1)}{A^{1/3}} - a_A \frac{(N-Z)^2}{A} + \delta(A, Z)$$

$$\delta(A, Z) = \begin{cases} +\delta_0 & Z, N \text{ even} \\ 0 & A \text{ odd} \\ -\delta_0 & Z, N \text{ odd (A even)} \end{cases} \quad (1.13)$$

- Volume term: nucleons attract nearest neighbors through strong force ( $a_V \sim 16 \text{ MeV}$ ), reflects the short-range nature of strong interaction.
- Surface term: correction to the volume term – nucleons on the surface aren't completely surrounded by other nucleons
- Coulomb term: EM charge repulsion
- Asymmetry term: Pauli exclusion principle
- Pairing term: spin coupling effect – if  $N$  and  $Z$  are even, then the nuclei will be stable thanks to the occurrence of 'paired spin'; on the other hand, nuclei with odd number of proton and neutron are usually unstable. ( $\delta_0 \sim 1 \text{ MeV}$ , slowly decreasing with  $A$ )

The first 3 terms are natural and easy to understand, while the 4th term is not so obvious. It is based only on Pauli exclusion principle. In heavy nuclei, more neutrons than protons are needed to balance the repulsion between protons. Due to the Pauli exclusion principle, these extra neutrons' energy will be higher than the rest of nucleons, therefore introducing this correction term.

Regard the nuclear system as a free Fermi gas of protons and neutrons, then the kinematic energy of this system will be:

$$E_k = E_N + E_Z = \frac{3}{5} Z E_F^p + \frac{3}{5} N E_F^n$$

Since the Fermi energy is proportional to  $n^{2/3}$

$$E_k = C(Z^{5/3} + N^{5/3})$$

Expanse it in terms of  $N-Z$   $A$ , we will get

$$E_k = 2^{-2/3} C \left( A^{5/3} + \frac{5}{9} \frac{(N-Z)^2}{A^{1/3}} \right) + O((N-Z)^4)$$

$$= \frac{3}{5} E_F A + \frac{1}{3} E_F \frac{(N-Z)^2}{A} + O((N-Z)^4)$$

The first term contributes to the volume term and the second term is minus the asymmetry term because  $E_k$  contributes to the binding energy negatively.

For a general discussion, we can ignore the 3rd term to focus on the homogeneous nuclear (residual strong) interaction between nucleons, and the 5th term which is too small. Now, we can talk about any nuclear system composed of  $Z$  protons (EM chargeless) and  $N$  neutrons, rather than just true nuclei. Now we have a simplified equation of state (EoS) for nuclear matter:

$$\begin{aligned} E &= a_V A - a_S A^{2/3} - a_A \frac{(N - Z)^2}{A} \\ e &= \frac{E}{A} = a_V - a_S A^{-1/3} - a_A \frac{(N - Z)^2}{A^2} \end{aligned} \quad (1.14)$$

Actually, we should also discard the second term. Obviously, we can't guarantee any specific shape about the nuclear system; what's more, for what people model with most – the infinite nuclear system, we don't need to consider the surface term at all.

$$\begin{aligned} E &= a_V A - a_A \frac{(N - Z)^2}{A} \\ e &= \frac{E}{A} = a_V - a_A \frac{(N - Z)^2}{A^2} = e_0(A) - a_A \beta^2 \end{aligned} \quad (1.15)$$

Here we define  $\beta = \frac{N-Z}{A}$  as asymmetry between the number of protons and neutrons.

For infinite system, density, instead of  $A$ , will be a better choice to parameterize the EoS. So we should replace  $N$ ,  $Z$  and  $A$  with their corresponding density:  $\rho_n$ ,  $\rho_p$  and  $\rho$  ( $\beta = \frac{\rho_n - \rho_p}{\rho}$ ). So we are considering an infinite uniform nuclear system at 0 temperature that interacts only via the nuclear force. For any identified  $\rho$ , eq (1.15) will be:

$$e(\rho, \beta) = e(\rho, 0) + S(\rho) \beta^2 + O(\beta^4) \quad (1.16)$$

This is an expansion of the binding energy per nucleon around  $\beta = 0$ . Due to the isospin symmetry between proton and neutron, any isoscalar quantities  $F$  will keep unchanged under  $n \leftrightarrow p$  interchange, while isovector quantities  $G$  will change sign.  $\beta$  is an isovector, so for a smooth  $F(\beta)$ , its expansion around  $\beta = 0$  has even terms only:

$$F(\beta) = F_0 + F_2 \beta^2 + F_4 \beta^4 + \dots$$

On the other hand, for a smooth  $G(\beta)$ , its expansion around  $\beta = 0$  has odd terms only:

$$G(\beta) = G_1 \beta + G_3 \beta^3 + \dots$$

$e$  is an isoscalar, it doesn't change under  $n \leftrightarrow p$  interchange as we can see from eq (1.15). The coefficient  $S(\rho) = \frac{\partial^2 e(\rho, \beta)}{\partial \beta^2}$  is what we call the **symmetry energy**, a key parameter in explaining a wide range of nuclear properties and phenomena. It describes how much energy will be released when exchange all protons into neutrons for a symmetric

nuclear system.

Not only is  $S$  itself important, but also its dependence on  $\rho$ . By convention,  $S(\rho)$  is expanded around the nuclear saturation density  $\rho_0$  (following the free Fermi gas assumption):

$$S(\rho) = S(\rho_0) + \frac{dS}{d\rho} \bigg|_{\rho_0} (\rho - \rho_0) + \frac{1}{2} \frac{d^2S}{d\rho^2} \bigg|_{\rho_0} (\rho - \rho_0)^2 + \frac{1}{6} \frac{d^3S}{d\rho^3} \bigg|_{\rho_0} (\rho - \rho_0)^3 + \dots \quad (1.17)$$

From which, we have some auxiliary parameters defined:

$$\begin{aligned} S_0 &= S(\rho_0) \\ L &= 3\rho_0 \frac{dS}{d\rho} \bigg|_{\rho_0} \\ K_{sym} &= 9\rho_0^2 \frac{d^2S}{d\rho^2} \bigg|_{\rho_0} \\ Q_{sym} &= 27\rho_0^3 \frac{d^3S}{d\rho^3} \bigg|_{\rho_0} \end{aligned} \quad (1.18)$$

Among them,  $L$  represents  $S$ 's dependence on  $\rho$ .

Take neutron star [28] as an example, it has most neutrons and a few protons, so its  $\beta = 1$ .

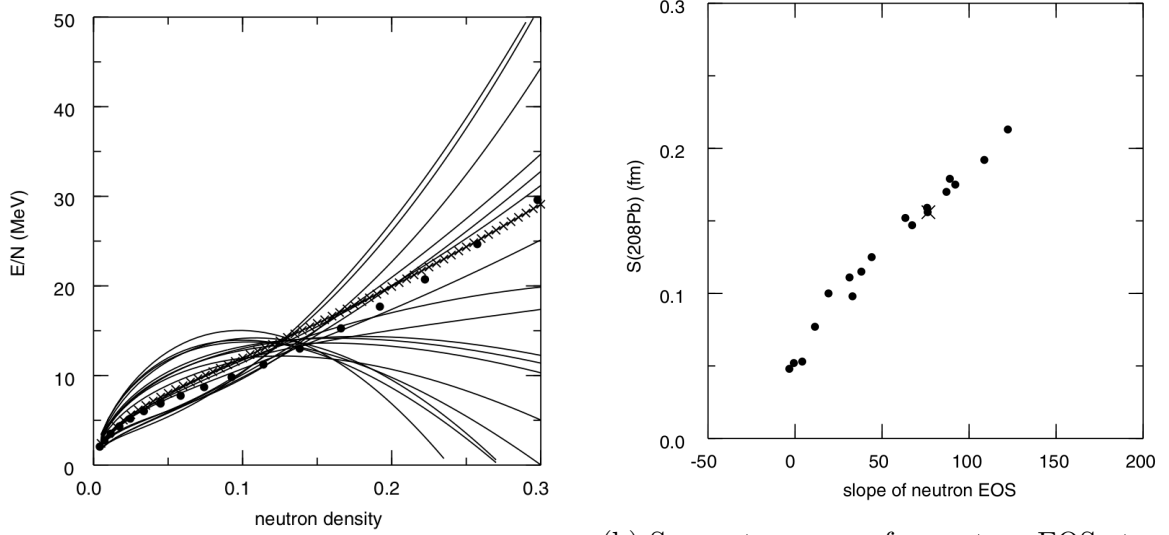
$$\begin{aligned} E &= E_0 + S \\ P &= \rho^2 \frac{dS}{d\rho} \approx \frac{L\rho^2}{3\rho_0} \\ RP^{-1/4} &\approx const \end{aligned} \quad (1.19)$$

The amazing thing is that neutron star's pressure dependents on  $L$  is proportional to  $R^4$ . Once we know the  $L$  value, we will know the pressure and therefore the radius of a neutron star.

Being such an important parameter, a great effort has been done to extract  $S$  and  $L$ . Comparing (1.15) and (1.16), we can directly get:

$$S(\rho) \approx -a_A \quad (1.20)$$

But this tells us only the symmetry energy at nuclear density ( $1.22 \times 10^{44} \text{ m}^{-3}$ ), what about the symmetry energy at other density values? Especially at the nuclear saturation density ( $\sim 1.7 \times 10^{44} \text{ m}^{-3}$ )? And what about its density dependence? Another strategy is the energy density functionals (EDF), which fits the binding energy throughout the nuclear mass table to find out the best EDF, then use it to calculate  $S(\rho)$ . Fitting parameterizations are constrained by nuclear density, proton RMS radii and nuclear binding energies. The problem is many EDFs can fit equally well with these constrains, but have quite different  $L$  values, as shown in Fig. ???. If there is a experiment that can identify  $S$  ( $L$ ) value without model dependence, then no doubt it will help a lot in understanding



(a) Neutron EOS for 18 Skyrme parameter sets. The filled circles are the Friedman-Panharipande (FG) variational calculations and the crosses are SkX. [20] We can see different models have very different symmetry energies. (b) Symmetry energy for neutron EOS at  $\rho_n = 0.1 \text{ neutron}/\text{fm}^3$  (in units of  $\text{MeV fm}^3/\text{neutron}$ ) vs the  $S$  value in  $^{208}\text{Pb}$  for 18 Skyrme parameter sets. The cross is SkX. Determination of  $S$  in  $^{208}\text{Pb}$  will greatly constrain the possible candidates.

the symmetry energy and the EoS.

The method to measure  $L$  in lab is to measure the neutron skin thickness of neutron rich nuclei. For symmetric nuclei ( $N = Z$ ), the protons and neutrons are expected to distribute uniformly. While for neutron-rich nuclei, the extra neutrons are pushed out against the surface tension[29], therefore forming a neutron skin.

Neutron skin and neutron star, though of their 18 orders of magnitude difference in size (fm vs km), both are neutron-rich nuclear matter and governed by the same physical laws: eq (1.19). So by measuring the neutron skin thickness, we can derive  $P$  and  $L$  values, for the study of neutron stars and nuclear EoS.

## 1.2 Physics Beyond the Standard Model (SM)

Parity-Violating Electron Scattering is always a promising avenue for physics beyond the SM in precision frontier. Flavor conserving interaction:

$$|A_\gamma + A_Z + A_{new}|^2 \rightarrow A_\gamma^2 \left[ 1 + 2\frac{A_Z}{A_\gamma} + 2\frac{A_{new}}{A_\gamma} \right]$$

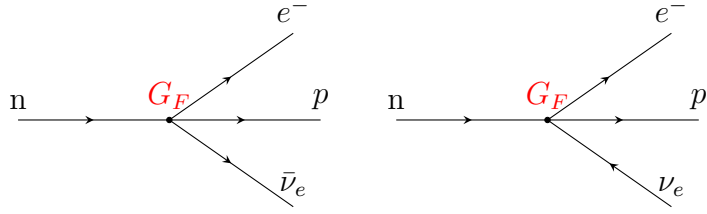


Figure 1.7: Fermi's interpretation of beta decay, current  $j_{n \rightarrow p}$  convert n into p and current  $j_{\nu_e \rightarrow e}$  creates  $(e, \bar{\nu}_e)$  pair.

## 1.3 Asymmetry

### Parity

The story traces back to the early age of particle physics. To explain the beta decay, Fermi proposed the 4-fermion interaction (Fermi's interaction) in 1933 [?], which is a low-energy limit of the weak interaction. In his theory, In analogy to the EM interaction (emission of a photon by an electron:  $\mathcal{M} = e j_\mu^{em} A^\mu$ ) Fermi interpreted the  $\beta$  decay as emission of a  $(e, \bar{\nu}_e)$  pair, during the process neutron converts itself into a proton, therefore coupling of two current:

$$\mathcal{M} = G_F (\bar{p} \mathbb{O}^\mu n) (\bar{e} \mathbb{O}_\mu \nu_e) = G_F j_{(n \rightarrow p)}^\mu j_\mu^{(\nu_e \rightarrow e)} \quad (1.21)$$

Where  $G_F = 1.166 \times 10^{-5} (GeV)^{-2}$  is the coupling constant that will be experimentally determined and  $\mathbb{O}$  represents the possible operators. Out of the 5 possible Lorentz invariant bilinear forms (Scalar (S:  $\mathbb{O} = \mathbb{1}$ ), pseudoscalar (P:  $\mathbb{O} = \gamma^5$ ), Vector (V:  $\mathbb{O} = \gamma^\mu$ ), Axial vector (A:  $\mathbb{O} = \gamma^\mu \gamma^5$ ) and Tensor (T:  $\mathbb{O} = \sigma^{\mu\nu} = \frac{i}{2}(\gamma^\mu \gamma^\nu - \gamma^\nu \gamma^\mu)$ ), Fermi selected the vector current to keep in line with the EM interaction:  $j^\mu = \bar{u} \gamma^\mu u$ .

In 1956, T. D. Lee and C. N. Yang, both being Fermi's student, postulated the revolutionary idea of parity violation for solving the  $\tau - \theta$  puzzle, and they succeeded. Only one year later, their hypothesis was experimentally tested by Wu etc in the decay of polarized  $Co^{60}$  nuclei, establishing the fact that parity is not conserved in weak interaction and therefore the weak current is not a pure vector-like quantity. Based on the experimental fact that parity is maximally violated [30], Sudarshan and Marshak [?], also Feynmann and Gell-Mann [?] updated Fermi's theory by replacing the vector current with a new current to accomodate parity violation, which led us to:

$$\mathcal{M} = \frac{G_F}{\sqrt{2}} (\bar{p} \gamma^\mu (\mathbb{1} - \gamma^5) n) (\bar{e} \gamma_\mu (\mathbb{1} - \gamma^5) \nu_e) \quad (1.22)$$

The factor of  $\frac{1}{\sqrt{2}}$  was introduced to keep  $G_F$  unchanged (Fermi's original theory was not aware the fact that neutrino was left-handed only, resulting in a decay phase space twice the real value in nature, to fix the problem, we can either modify the value of  $G_F$  or introduce a correction factor  $\frac{1}{\sqrt{2}}$ ). The V and A parts of V-A theory refer to the vector and axial vector current, responsible for Fermi transitions and Gamow-Teller transitions

respectively.

$$j_V^\mu = \bar{u}\gamma^\mu u \quad j_A^\mu = \bar{u}\gamma^\mu\gamma^5 u \quad (1.23)$$

The form of V-A as  $\mathbb{1} - \gamma^5$  happens to be the projection operator:

$$P_R = \frac{\mathbb{1} + \gamma^5}{2} \quad P_L = \frac{\mathbb{1} - \gamma^5}{2} \quad (1.24)$$

By definition of gamma matrix, one can easily verify that:

$$\begin{aligned} \left(\frac{\mathbb{1} - \gamma^5}{2}\right)^2 &= \frac{\mathbb{1} - \gamma^5}{2} & \gamma^\mu \frac{\mathbb{1} - \gamma^5}{2} &= \frac{\mathbb{1} + \gamma^5}{2} \gamma^\mu \\ \gamma^\mu \frac{\mathbb{1} - \gamma^5}{2} &= \frac{\mathbb{1} + \gamma^5}{2} \gamma^\mu \frac{\mathbb{1} - \gamma^5}{2} \end{aligned} \quad (1.25)$$

Then one can see the handness of the new current:

$$\mathcal{M} = \frac{4G_F}{\sqrt{2}} (\bar{p}\gamma^\mu \frac{\mathbb{1} - \gamma^5}{2} n) (\bar{e}\gamma_\mu \frac{\mathbb{1} - \gamma^5}{2} \nu_e) = \frac{4G_F}{\sqrt{2}} (\bar{p}_L \gamma^\mu n_L) (\bar{e}_L \gamma_\mu \nu_{e,L}) \quad (1.26)$$

Only left (right)-handed particle (antiparticle) can interact in weak interaction. In analogy to EM interaction, the coupling constant is proportional to a weak charge (weak isospin  $T_3$ ), then right-handed fermions (left-handed antifermions) will have  $T_3 = 0$  and left-handed fermions have the same weak charge.

Given the fact that the charge current (it changes particle's electric charge) connects 2 types of fermions and lepton number is conserved in weak interaction, it is natural to group them in a lepton doublet:  $f_L = \begin{pmatrix} \nu_l \\ l \end{pmatrix}_L$ . This implies us that for left-handed fermions:  $T = \frac{1}{2}$ ,  $T_3 = \pm \frac{1}{2}$

Applying the V-A theory to more decay and scattering process ( $\mu^+ \rightarrow e^+ + \nu_e + \bar{\nu}_\mu$ ,  $\pi^- \rightarrow l + \bar{\nu}_l$  etc.), we have 2 charge currents:

$$j_\mu^- = \bar{\nu}_{e,L} \gamma_\mu e_L \quad j_\mu^+ = \bar{e}_L \gamma_\mu \nu_{e,L} \quad (1.27)$$

which can be written in a more compact way w.r.t. the lepton doublet:

$$j_\mu^\pm = \bar{f}_L \gamma_\mu t^\pm f_L \quad (1.28)$$

where,

$$t^+ = \begin{pmatrix} 0 & 1 \\ 0 & 0 \end{pmatrix} = \frac{1}{2}(\sigma^1 + i\sigma^2) \quad t^- = \begin{pmatrix} 0 & 0 \\ 1 & 0 \end{pmatrix} = \frac{1}{2}(\sigma^1 - i\sigma^2) \quad (1.29)$$

We can see clearly the SU(2) symmetry by the  $t^\pm$  expression, the raising ( $t^+$ ) and lowing matrices ( $t^-$ ) are the combination of the first 2 Pauli matrices. Then one should consider the third component:

$$j_\mu^3 = \bar{f}_L \gamma_\mu \frac{1}{2} t^3 f_L = \frac{1}{2} (\bar{\nu}_{e,L} \gamma_\mu \nu_{e,L} - \bar{e}_L \gamma_\mu e_L) \quad (1.30)$$

This is a neutral current. But what does this neutral current represents for? The then only known neutral current is the EM current, but neutrino is neutral, how could it have a EM neutral current? The neutral current kept as a mystery until Glashow, Salam and Weinberg postulated the GSW model, which interpretes  $j^3$  as part of a more complete neutral current that includes  $j^{em}$  – the so called  $SU(2)_L \times U(1)$ .

One problem with Fermi's theory is that the cross section ( $\sigma \sim G_F^2 E^2$ ) will diverge at high energy, to which the solution was the introduction of mediating mesons:  $W^\pm$ . Unlike photon that mediates EM interaction, W boson is charged, and has a heavy mass implied from the short-range nature of the weak interaction. The introduction of W fields just make the weak interaction more similar to the EM interaction:

$$\mathcal{L} = g_W (J^+ W^+ + J^- W^-) \quad (1.31)$$

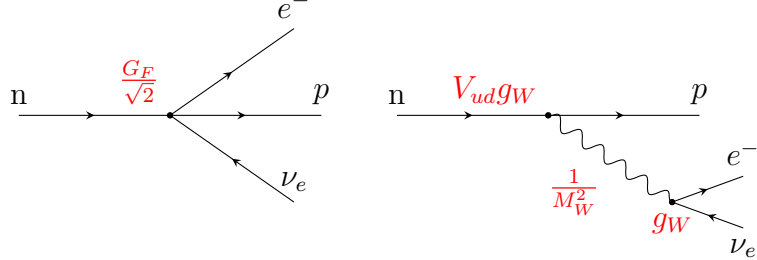


Figure 1.8: W-boson exchange picture of  $\beta$  decay

Given the similarity between weak interaction and EM interaction, it is natural to unify them into a multiplet of gauge fields. Based on Yang and Mills' non-abelian gauge theory, Salam and Weinberg successfully came up with a unified framework for both interactions – the  $SU(2)_L \times U(1)$  structure firstly suggested by Glashow. The  $SU(2)$  part is generated by ‘weak isospin’, the subscript L refers to the fact that only left-handed fermions couple to gauge boson of  $SU(2)$ , and the  $U(1)$  part comes from the ‘weak hypercharge’. There are 4 vector bosons:

$$W^1, W^2, W^3, B$$

These bosons will couple to both left-handed and right-handed fermions. For simplicity, let's consider only the first generation leptons here:

$$\psi_1 = \begin{pmatrix} \nu_e \\ e^- \end{pmatrix} \quad \psi_2 = \nu_{e,R} \quad \psi_3 = e_R^- \quad (1.32)$$

For the left-handed doublet  $\psi_1$ , it interacts to all bosons, so the covariant derivative is:

$$D_\mu = \partial_\mu - ig \frac{\sigma^a}{2} W_\mu^a - ig' y_1 B_\mu \quad (1.33)$$

where  $y_1$  is the hypercharge of  $\psi_1$ . The corresponding coupling Lagrangian is:

$$\mathcal{L}_{int,L} = -i\bar{\psi}_1\gamma^\mu(g\frac{\sigma^a}{2}W_\mu^a + g'y_1B_\mu)\psi_1 = -i(g\mathbf{j}^\mu\mathbf{W}_\mu + g'y_1\bar{\psi}_1\gamma^\mu\psi_1B_\mu) \quad (1.34)$$

For right-handed singlets, they don't couple to weak vector bosons, therefore the covariant derivative for right-handed fermions is:

$$D_\mu = \partial_\mu - ig'y_{2(3)}B_\mu \quad (1.35)$$

$y_{2(3)}$  are the hypercharge of  $\psi_{2(3)}$  and the Lagrangian:

$$\mathcal{L}_{int,R} = -ig'(y_2\bar{\psi}_2\gamma^\mu\psi_2 + y_3\bar{\psi}_3\gamma^\mu\psi_3)B_\mu \quad (1.36)$$

So the complete interacting Lagrangian is:

$$\mathcal{L}_{int} = \mathcal{L}_{int,L} + \mathcal{L}_{int,R} = -i(g\mathbf{j}^\mu\mathbf{W}_\mu + g'j_Y^\mu B_\mu) \quad (1.37)$$

where  $\mathbf{j}^\mu$  is the weak isospin current, it couples to a weak isos triplet of vector bosons:  $\mathbf{W} = (W^1, W^2, W^3)$  with coupling strength  $g$ ; and the weak hypercharge current  $j_Y^\mu = \sum_{i=1}^3 y_i\bar{\psi}_i\gamma^\mu\psi_i$  couples to an isosinglet vector boson:  $B^\mu$  with strength  $g'$ .

Because the GSW model preserve the SU(2) structure we talked about before, therefore it is obvious to reproduce the charged current:

$$W^\pm = \frac{1}{\sqrt{2}}(W^1 \mp iW^2) \quad j^\pm = j^1 \pm ij^2 \quad (1.38)$$

$$j^1W^1 + j^2W^2 = \frac{1}{\sqrt{2}}(j^+W^+ + j^-W^-) \quad (1.39)$$

As for the other 2 bosons, there is no way to satisfy  $y_1 = y_2 = y_3$  and  $g'y_i = eQ_i$  at the same time, so  $B$  is not pure  $A$ . Since both fields are neutral, one can try to mix them, and get some result matching experimental results:

$$\begin{pmatrix} A \\ Z \end{pmatrix} = \begin{pmatrix} \cos\theta_W & \sin\theta_W \\ -\sin\theta_W & \cos\theta_W \end{pmatrix} \begin{pmatrix} B \\ W^3 \end{pmatrix} \Leftrightarrow \begin{pmatrix} B \\ W^3 \end{pmatrix} = \begin{pmatrix} \cos\theta_W & -\sin\theta_W \\ \sin\theta_W & \cos\theta_W \end{pmatrix} \begin{pmatrix} A \\ Z \end{pmatrix} \quad (1.40)$$

The mixing angle is known as the Weinberg angle.

Rewrite eq. 1.37 in terms of  $W^\pm$ ,  $Z$  and  $A$ :

$$\begin{aligned} i\mathcal{L} = & \frac{g}{\sqrt{2}}(j^+W^+ + j^-W^-) \\ & + \sum_{i=1}^3 \bar{\psi}_i\gamma^\mu \left\{ \left[ g\frac{\sigma^3}{2}\sin\theta_W + g'y_i\cos\theta_W \right] A_\mu + \left[ g\frac{\sigma^3}{2}\cos\theta_W - g'y_i\sin\theta_W \right] Z_\mu \right\} \psi_i \end{aligned} \quad (1.41)$$

where  $g_W = g/\sqrt{2}$  is the coupling constant of weak charged current.

The neutral part can be expressed in corresponding charge:

$$\begin{aligned} i\mathcal{L}_{NC} &= \sum_{i=1}^3 \bar{\psi}_i \gamma^\mu \psi_i [(g \sin \theta_W I_3 + g' \cos \theta_W Y) A_\mu + (g \cos \theta_W I_3 - g' \sin \theta_W Y) Z_\mu] \\ &= ej_{EM}^\mu Q A_\mu + g_Z j_Z^\mu Q_Z Z_\mu \end{aligned} \quad (1.42)$$

Where  $I_3$  is the weak isospin and  $Y$  is the weak hypercharge; Similarly,  $Q$  is the EM charge in unit of electron charge and  $Q_Z$  is the weak neutral charge.  $e$  and  $g_Z$  are coupling constant for EM and neutral weak interaction respectively. With  $I_3$  and  $Y$  vary for different fermions, we have the following relationship:

$$e = g \sin \theta_W = g' \cos \theta_W = \frac{gg'}{g^2 + g'^2} \quad (1.43)$$

So the Weinberg angle is identified as:

$$\tan \theta_W = \frac{g'}{g} \quad (1.44)$$

and:

$$Y = Q - I_3 \quad (1.45)$$

The value of weak hypercharge depends on the definition, if one keep the  $\frac{1}{2}$  factor in the B current, then one will get:

$$\frac{Y}{2} = Q - I_3 \Rightarrow Y = 2(Q - I_3) \quad (1.46)$$

This is the traditional formula. In this thesis we will use the definition of eq. 1.45.

As for neutral weak current, the value of  $g_Z$ ,  $Q_Z$  and  $J_Z$  dependent on our choice, as long as:

$$g_Z Q_Z J_Z = (g \cos \theta_W I_3 - g' \sin \theta_W Y) \bar{\psi} \gamma^\mu \psi \quad (1.47)$$

The traditional choice is:

$$\begin{aligned} g_Z &= \frac{g}{\cos \theta_W} = \frac{e}{\sin \theta_W \cos \theta_W} \\ Q_Z &= I_e \cos^2 \theta_W - Y \sin^2 \theta_W = I_3 - Q \sin^2 \theta_W \end{aligned} \quad (1.48)$$

One can also absorb  $Q_Z$  into  $J_Z$  to get:

$$J_Z = \sum \bar{\psi}_i \gamma^\mu (I_3 - Q \sin^2 \theta_W) \psi_i = \sum_f \bar{f} \gamma^\mu \frac{c_v - c_a \gamma^5}{2} f \quad (1.49)$$

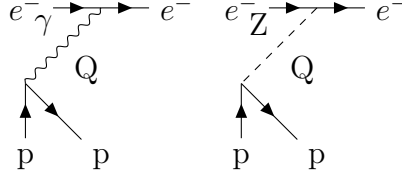
with

$$c_v = I_3 - 2Q \sin^2 \theta_W \quad c_a = I_3 \quad (1.50)$$

So we come to a striking prediction of the GSW model: the neutral weak interaction, which

was experimentally observed in 1973 in the Gargamelle neutrino experiment [31].

What we are going to observe in PREX-II and CREX exactly originates from this neutral weak current.



$$\mathcal{A}_{pv} = \frac{\frac{d\sigma^R}{d\Omega} - \frac{d\sigma^L}{d\Omega}}{\frac{d\sigma^R}{d\Omega} + \frac{d\sigma^L}{d\Omega}} = \frac{|\mathcal{M}^R|^2 - |\mathcal{M}^L|^2}{|\mathcal{M}^R|^2 + |\mathcal{M}^L|^2}$$

where:  $\mathcal{M}^{R,L} = \mathcal{M}_\gamma + \mathcal{M}_Z^{R,L}$ . Because EM amplitude is much larger than the weak amplitude:  $\mathcal{M}_\gamma \gg \mathcal{M}_Z^{R,L}$

$$\begin{aligned} \mathcal{A}_{pv} &\approx \frac{2\mathcal{M}_\gamma(\mathcal{M}_Z^R - \mathcal{M}_Z^L)}{2\mathcal{M}_\gamma^2} \\ &= \frac{\mathcal{M}_Z^R - \mathcal{M}_Z^L}{\mathcal{M}_\gamma} \propto \frac{\frac{d\sigma_{\text{weak}}}{d\Omega}}{\frac{d\sigma_{\text{EM}}}{d\Omega}} \\ &= \left( \frac{\mathcal{M}_Z^R - \mathcal{M}_Z^L}{\mathcal{M}_\gamma} \right)_{\text{point}} \times \frac{Q_{wk}}{Z} \frac{F_{wk}(Q^2)}{F_{ch}(Q^2)} \\ &\approx \frac{g_Z^2/M_Z^2}{e^2/Q^2} \frac{(j_Z^{e,R} - j_Z^{e,L})j_Z^n}{j_\gamma^e j_\gamma^p} \times \frac{Q_{wk}}{Z} \frac{F_{wk}(Q^2)}{F_{ch}(Q^2)} \quad (Q^2 \ll M_Z^2) \\ &= -\frac{8G_F/\sqrt{2}}{4\pi\alpha/Q^2} \frac{(\bar{e}_L\gamma^\mu I_3 e_L)\frac{1}{2}(\bar{n}_L\gamma_\mu I_3 n_L)}{(\bar{e}_L\gamma^\mu e_L)(\bar{p}\gamma_\mu p)} \times \frac{Q_{wk}}{Z} \frac{F_{wk}(Q^2)}{F_{ch}(Q^2)} \\ &= -\frac{G_F Q^2}{4\pi\alpha\sqrt{2}} \frac{Q_{wk}}{Z} \frac{F_{wk}(Q^2)}{F_{ch}(Q^2)} \end{aligned} \quad (1.51)$$

The weak isospin for electron and neutron is:  $I_3(e^-) = I_3(n) = -\frac{1}{2}$ . The factor of  $\frac{1}{2}$  in line 5 of eq. 1.51 arises from the fact that the target is unpolarized.

The FFs can be further decomposed into point nucleon FFs:

$$\begin{aligned} F_{ch}(q) &= G_{ch}^p(q)F_p(q) + G_{ch}^n(q)F_n(q) \\ &= G_E^p(q)F_p(q) + \frac{N}{Z}G_E^n(q)F_n(q) \\ F_{wk}(q) &= G_{wk}^p(q)F_p(q) + G_{wk}^n(q)F_n(q) \\ &= G_E^p(q) \left[ F_n(q) - \frac{Z}{N}(1 - 4\sin^2\theta_W)F_p(q) \right] - G_E^n(q) \left[ F_n(q)(1 - 4\sin^2\theta_W) - \frac{Z}{N}F_p(q) \right] \end{aligned}$$

Where  $G_E^p(q)$  and  $G_E^n(q)$  are the EW single nucleon FFs,  $F_p(q)$  and  $F_n(q)$  are the FFs of point proton and neutron density distribution. Compared with  $G_E^p(q)$ , the charge FF of

the neutron  $G_E^n(q)$  can be neglected for small momentum transfer:

$$\begin{aligned} F_p(q) &= \int d^3r j_0(qr) \rho_p(r) \\ F_n(q) &= \int d^3r j_0(qr) \rho_n(r) \\ G_{wk}^p &= q_p G_E^p + q_n G_E^n + q_0 G_E^s \\ G_{wk}^n &= q_p G_E^p + q_n G_E^n + q_0 G_E^s \end{aligned}$$

For weak charges including radiative correction

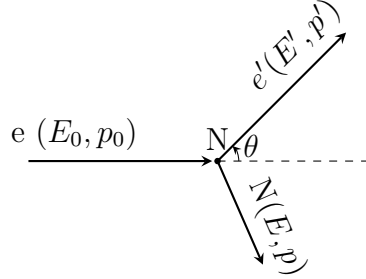
$$q_p \approx 0.0712 \quad q_n = q_0 \approx -0.9877$$

$$\begin{aligned} \frac{F_{wk}(q)}{F_{ch}(q)} &\approx \frac{F_n(q)}{F_p(q)} \\ \mathcal{A}_{pv} &= \frac{G_F Q^2}{4\pi\alpha\sqrt{2}} \frac{Q_{wk}}{Z} \left[ \frac{F_n(q)}{F_p(q)} - \frac{Z}{N} (1 - 4 \sin^2 \theta_W) \right] \end{aligned}$$

When ignoring structure (tree level):

$$\mathcal{A}_{pv} = \frac{G_F Q^2}{\pi\alpha\sqrt{2}} \left( \sin^2 \theta_W + \frac{1}{4} \left[ \frac{N}{Z} - 1 \right] \right)$$

## 1.4 Dynamics



4-Momentum conservation

$$E_0 + M = E' + E \quad \mathbf{p}_0 = \mathbf{p}' + \mathbf{p}$$

Assume ( $m_e \ll 0 \Rightarrow E_0 \approx p_0$ ,  $E' \approx p'$ )

$$\begin{aligned} E^2 &= M^2 + \mathbf{p}^2 = M^2 + (\mathbf{p}_0 - \mathbf{p}')^2 \\ &= M^2 + (E_0 - E' \cos \theta)^2 + (E' \sin \theta)^2 \\ &= M^2 + E_0^2 + E'^2 - 2E_0 E' \cos \theta \\ &= (E_0 + M - E')^2 \end{aligned}$$

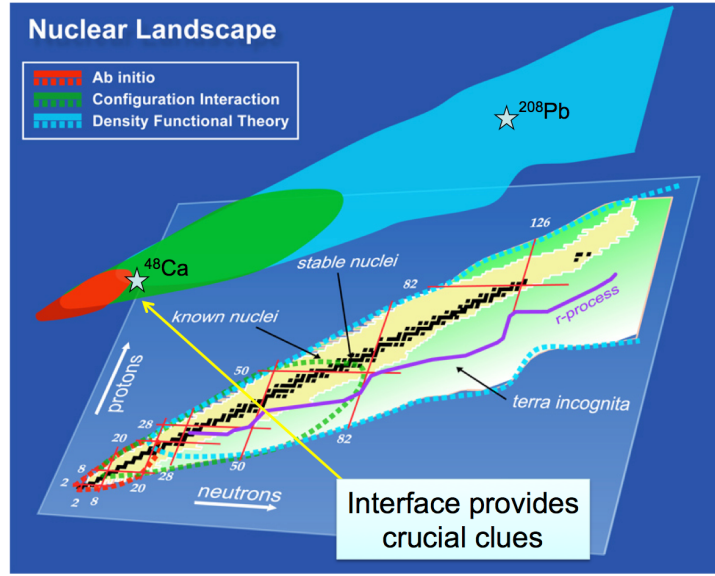


Figure 1.9: Nuclear Landscape

So we can get

$$\begin{aligned}
 M(E_0 - E') &= E_0 E' (1 - \cos \theta) \\
 E' &= \frac{M E_0}{M + E_0 (1 - \cos \theta)} \\
 Q^2 &= -q^2 = -[(E_0 - E')^2 - (\mathbf{p}_0 - \mathbf{p}')^2] \\
 &= 2E_0 E' (1 - \cos \theta)
 \end{aligned}$$

## 1.5 Why Pb and Ca

As tiny as the neutron skin thickness, to measure it relatively accurate, the larger it is, the better our measurement will be. So the target elements should have a large neutron excess. So  $^{208}\text{Pb}$  ( $^{48}\text{Ca}$ ) is chosen for PREX-II (CREX). Besides, both nuclei are spin-0, so that we don't need to worry about the target polarization. When the single nucleon separation energy in a nucleus is much larger than that of its neighbors, it is said that this nucleus has a magic number of protons or neutrons. The magic number arises from the nucleon shell structure – when a shell is fully filled and the next higher energy shell is empty, it is hard to separate out a nucleon from that closed shell. Both  $^{48}\text{Ca}$  and  $^{208}\text{Pb}$  are doubly magic nuclei, which means both the number of protons and neutrons are magic number, therefore a simple structure. It also means that the energy of their first excited state is much larger than the ground state, being 3.84 and 2.6 MeV respectively. Combined with the high momentum resolution of HRS, it provides sounding ground for flux integration detection.

As we see in previous section, the elastic scattering is quasi, not exact. The small energy change is caused by nuclei recoil. The heavier the target nuclei, the smaller the

recoil effect, the smaller the  $Q^2$ , the better our measurement of  $Q^2$  and scattering angle.

Finally,  $^{48}\text{Ca}$ , which lies in the medium region of the nuclear landscape, is accessible from both ab-initio and DFT theoretical approaches. By measuring the neutron skin thickness of  $^{48}\text{Ca}$ , we hope to provides a possibility to bridge these two methods.

# Chapter 2

## Experimental Setup

Over the past 30 years, PVES has been a well-established and powerful experimental technique in atomic, nuclear and particle physics. Its success traces back to Lee and Yang's prediction of parity violation in beta decay in 1956 [? ] and the following experimental provement by Wu in 1957 [32]. Shortly later, Zel'dovich first predicted the existance of parity-violating weak neutral current and proposed to measure it in electron-proton scattering [33] in 1959. But it was only about 20 years later that people was able to experimentally observe the PV asymmetry in electron scattering experiments. In 1978, C.Y. Prescott etc. (E122 experiment at SLAC) measured the PV asymmetry in the inelastic scattering of longitunally polarized electrons from an unpolarized deuterium target [3]. With this successful demonstration, more effort was made to improve this experimental technique, which matured and boomed at the turn of the last century. Many experiments were conducted to probe the contribution of strange sea quarks to nucleons' EM FFs (SAMPLE, G0, HAPPEX and A4) and test the Electroweak sector of the SM at low energy (E158, PVDIS, Qweak). It was PREX-I that first proposed the application of PVES to probe the structure of nuclei, then followed by PREX-II and CREX. Future programs (Moller, SoLID and MESA experiments) will continue the development of PVES and push it to a higher precision.

Generally, PVES experiments requires 2 experimental conditions: polarized electron beam and fast flipping of beam polarization. Both requirements actually come to the same dependence: an intense source of polarized electrons and with quick response. The nature of being PV means measurement between different polarization states, while the **tiny** characteristic of PV asymmetry demands fast flipping of the polarization states. To measure such a tiny quantity, it is essential to control the experimental configurations as the same as possible between different beam helicities. One obvious and effective method to do the job is to fast flipping of beam helicity, the faster the helicity reversal, the smaller the possible change in beam conditions, target density and other apparatus, the smaller the introduced false asymmetry. This requirement makes PVES out of the capacity of storage ring accelerators. Though of the fast reversal of electron's helicity, much effort is needed to control the beam fluctuation, making it as small as possible. Possible systematic uncertainties in the source and accelerator will be controlled through the slow reversal

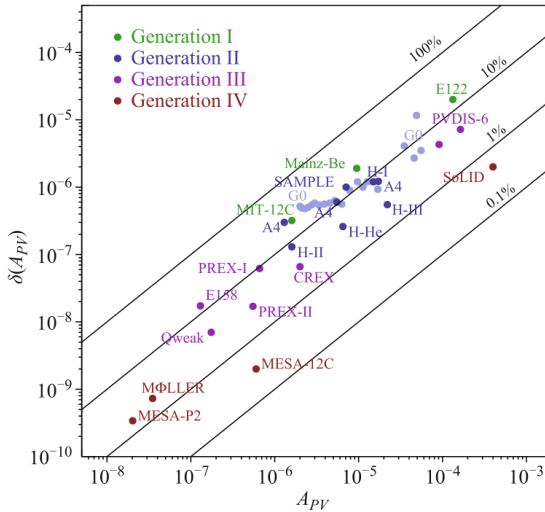


Figure 2.1: Evolution of PVES experiments, solid lines represent the relative precision. Generation I experiments (E122 (1978) [3], MIT-12C (1989) [4] and Mainz-Be (1990) [5]) did pioneering work to pave the way for PVES. Generation II experiments (the SAMPLE collaboration [6] at the MIT-Bates accelerator, the G0 [7] and HAPPEX [8] collaboration at Jefferson Lab and the A4 collaboration [9] at the Maizer Mikrotron (MAMI) accelerator) were devoted to the exploration of strange FFs in nucleons. Generation III experiments (E158 at SLAC [10], Qweak [11] and PVDIS [12]) tested the SM at low energy and measured the neutron skin thickness of nuclei (PREX-I/II and CREX). The planned Generation IV experiments (SoLID program [13] and MOLLER experiment [14] at JLab, P2 experiment on the future Mainz Energy-recovery Superconducting Accelerator (MESA) [15]) will continue to test the SM and explore the structure of nucleons with higher precisions. (MESA-12C is the same experiment as MESA-P2 with a different  $^{12}\text{C}$  target)

of beam helicity. In terms of the target deformity under electron bombardment, a raster with very high scanning rate will minimize this uncertainty. As for detection of scattered electrons, electron flux rather than single electron will be counted due to high scattering rate in such experiments.

The 2 sister experiments were conducted in Hall A at JLab, the CEBAF accelerator at JLab is one of the few facilities in the world that can do PVES experiments ( other facilities include MIMA and its successor MESA, the Facility for Antiproton and Ion Research (FAIR) and the Facility for Rare Isotope Beams (FRIB)). CEBAF provided excellent polarized electron beams (helicity correlated difference at sub-nanometer level) to hall A, with dedicated apparatus (Compton polarimeter, taget chamber, HRS and others) in Hall A, we were able to measure this tiny asymmetry precisely.

	PREX-II	CREX
Target	$^{208}\text{Pb}$	$^{48}\text{Ca}$
Target density ( $g/cm^3$ )	11.38	1.855
Target thickness ( $mm$ )	$0.2554 + 0.5520 + 0.2566$	6
Number of Target	10	1 + 1
Used	6	2
Beam Energy ( $GeV$ )	0.953	2.18
Largest Beam Current ( $\mu A$ )	70	150
Average Beam Polarization (%)	89.7	87.1
Beam Rate ( $MHz$ )	249.5	249.5
Electrons/Bunch ( $\times 10^6$ )	1.75	3.76
Helicity Flip Rate ( $Hz$ )	240	120
Power on Target ( $Watt$ )		
Scattering angle (deg)	4.7	4.51
$Q^2$ ( $GeV^2$ )	0.00616	0.0297
Scattering rate ( $MHz/arm$ )	$\sim 2200^{\textcolor{red}{1}}$	$\sim 28$
xsection ( $mbarn$ )	3930.6	5.3
Acceptance ( $msr$ )	0.0037	0.0037
Collected Charge ( $C$ )	114	412
Predicted $\mathcal{A}_{pv}$ ( $ppm$ )	0.6	2
Proposed precision	3.6%	2.4%
Error on $R_n$ ( $fm$ )	0.06	0.02

Table 2.1: Summary of PREX-II and CREX

## 2.1 Kinematics

PREX-II and CREX are follow-up experiments to PREX-I, which also ran at JLab in 2010. With excellent control of systematic uncertainty, but unfortunately, many technical challenges during the experiment, PREX-I’s result was statistics limited, achieving a precision of 10% [? ]:

$$\mathcal{A}_{Pb} = 656 \pm 60(stat) \pm 14(syst) \text{ ppb}$$

Based on the experience and lessons we learned from PREX-I, PREX-II and CREX had more well-established designs, which helped to meet the goal of high-precision.

One important feature of these 2 experiments is the redundancy design for critical components: we have 2 slow helicity reversal for systematic uncertainty control, we have 2 polarimeters for polarization measurement, we have multiple BPMs and BCMs for beam parameter monitoring, we have multiple Pb foil targets and finally 2 HRS arms for electron reception.

Experiment	PREX-II (%)	CREX (%)
Charge Normalization	0.1	0.1
Beam Asymmetry	1.1	0.3
Detector Non-Linearity	1.0	0.3
Transverse Asymmetry	0.2	0.1
Polarization	1.1	0.8
Target Contamination	0.4	0.2
Inelastic Scattering	< 0.1	0.2
Effective $Q^2$	0.4	0.8
Total Systematic	2	1.2
Statistical	3	2.4
Total	3.6	2.7

Table 2.2: Budget of systematic and statiscal error in both experiments [35, 36]

### Uncertainty Budget

The goal of PREX-II is to achieve the 1% precision in  $^{208}\text{Pb}$  neutron radius proposed by PREX-I, which requires the presicion of PV asymmetry measurement better than 3% [34]. CREX proposed similar goal, that a precision of 0.02  $fm$  (0.6%) in the  $^{48}\text{Ca}$  neutron radius will be an essential benchmark to test various microscopic models, which correspond to a 2.4% total error in PV asymmetry.

As said above, PREX-I already had impressive control over systematic uncertainties (2.1%), so will the PREX-II and CREX. The main concern is to collect as much scattered electrons as possible to reduce statistical error, which is inversely proportional to  $\sqrt{N}$ .

$$\frac{\delta \mathcal{A}}{\mathcal{A}} = \sqrt{\sigma_{stat}^2 + \sigma_{sys}^2} \quad \sigma_{stat} = \frac{\sigma_{det}}{P\sqrt{N}} \quad (2.1)$$

where:

- $\sigma_{det}$  is the detector uncertainty
- $P$  is the beam polarizaiton
- $N$  is the total number of scattered electrons

#### 2.1.1 Figure Of Merits (FOM)

The choice of beam energy and scattering angle is a compromise of competing factors. PV asymmetry prefers larger beam energy and larger scattering angle, while scattering rate falls dramatically with beam energy and scattering angle,  $Q^2$  also likes smaller beam energy and scattering angle, and calculation showes that the sensitivity of PV asymmetry w.r.t. neutron radius is oscillating along beam energy. All these considerations are

incorporated into the FOM, which is defined as:

$$\text{FOM} = R \times \mathcal{A}^2 \times \epsilon^2$$

where  $R$  is the scattering rate,  $\mathcal{A}$  the PV asymmetry and  $\epsilon$  the sensitivity of  $\mathcal{A}$  w.r.t.  $R_n$ . One difference here is that FOMs for most PVES experiments have only  $R$  and  $\mathcal{A}^2$ , the inclusion of  $\epsilon$  in our FOM help to achieve a higher precision in  $R_n$  measurement.

## Rate

For a data set of  $N$  independent events sampled from one normal distribution  $X \sim N(x_0, \sigma_0)$ , the statistical uncertainty on the measured mean value will be:

$$\text{var}(\bar{x} = \frac{1}{n} \sum x_i) = \frac{1}{n^2} \text{var}(x_i) = \frac{\sigma_0^2}{n} \implies \sigma(\bar{x}) = \frac{\sigma_0}{\sqrt{n}}$$

Assume one want to measure a 1 *ppm* asymmetry to 1% statistical uncertainty,

$$\frac{\sigma_A}{A} = \frac{1}{A} \frac{\sigma_{\text{det}}}{\sqrt{2N}} \approx \frac{1}{A\sqrt{2N}} = 1\% \implies N = 5 \times 10^{15} \quad (2.2)$$

a factor of 2 is included because we have 2 HRS arms. One need to count  $\sim 10^{15}$  scattered electrons. Given a counting rate of 1 *MHz*, it will take  $\frac{5 \times 10^{15}}{1 \text{ MHz}} = 5 \times 10^9 \text{ s} \approx 160 \text{ years}$ , a completely unacceptable time scale. So we have to turn to integrated flux technique for a higher scattering rate, which is:

$$\frac{dR(\theta)}{d\Omega} = \frac{d\sigma}{d\Omega} I t \frac{\rho}{A} \times N_A \quad (2.3)$$

- $\frac{d\sigma}{d\Omega}$  is the fractional cross section in  $\text{cm}^2/\text{str}$ ,
- $I$  is the beam current in *electrons/s*
- $t$  is the target thickness in *cm*
- $\rho$  is the target density in  $\text{g/cm}^3$
- $A$  is the atomic number
- $N_A = 6.022 \times 10^{23}$  is the Avogadro's constant and conversion factors.

The differential cross section was numerically calculated by our theoretical friends with values of 3930.6 *mbarn* and 5.3 *mbarn* for  $^{208}\text{Pb}$  and  $^{48}\text{Ca}$  at their corresponding kinematics. Other parameters can be checked in table 2.1.

The total rate will be the integration over the acceptance:

$$R = \int \frac{dR(\theta)}{d\Omega} d\Omega = \frac{dR}{d\Omega} d\Omega \quad (2.4)$$

PREX-II and CREX have an acceptance defined by the septum and Q1 collimator, which is  $d\Omega = 0.0037 \text{ str}$

Finally, we should also consider radiative correction due to emission of virtual and real soft photons (Bremsstrahlung), and hard photons by vacuum polarization, this correction is formulated as:

$$\eta = \left( \frac{\Delta}{E} \right)^{bt} \quad (2.5)$$

which is evaluated to be:  $\eta \sim 0.5$ .

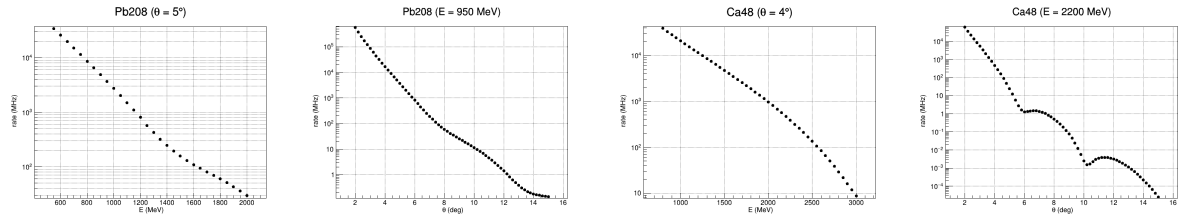


Figure 2.2: Scattering rate versus beam energy and scattering angle for  $^{208}\text{Pb}$  and  $^{48}\text{Ca}$ , the energy and scattering angle are design values. We see that rate falls quickly along both beam energy and scattering angle for both nuclei, so one would like small beam energy and small scattering angle (equivalently small  $\mathbf{q}$ ) for large scattering rate.

## Asymmetry and Sensitivity

As we shown in eq. 2.2, the asymmetry itself matters, a 2 times larger asymmetry means we can reduce the run time to one quarter, a huge save of beam time. So we should choose the kinematics region where asymmetry is large. Besides, asymmetry's sensitivity ( $\epsilon$ ) to neutron radius is also important, keep in mind that our final goal is to extract neutron radius from PV asymmetry, the more sensitive the asymmetry to neutron radius, the more precise the extracted neutron radius. The sensitivity is calculated as the relative change of  $\mathcal{A}$  with 1% change in neutron radius.

$$\epsilon = \frac{\delta \mathcal{A}/\mathcal{A}}{\delta R/R} = \frac{|\mathcal{A}_{stretched} - \mathcal{A}|/\mathcal{A}}{1\%} \quad (2.6)$$

Though asymmetry is what we want to measure, we can estimate its value based on some theoretical models, as was numerically calculated by our theoretical friends in [2].

Based on the theoretical result, we can optimize the kinematics for both nuclei:

$$\frac{\delta R}{R} = \frac{\delta \mathcal{A}}{\mathcal{A}} \frac{1}{\epsilon} = \frac{\sigma_{det}}{P} \frac{1}{\sqrt{N} \mathcal{A} \epsilon} \quad (2.7)$$

To minimize  $\delta R/R$ , it is equivalent to maximize

$$FOM = N \times \mathcal{A}^2 \times \epsilon^2 \quad (2.8)$$

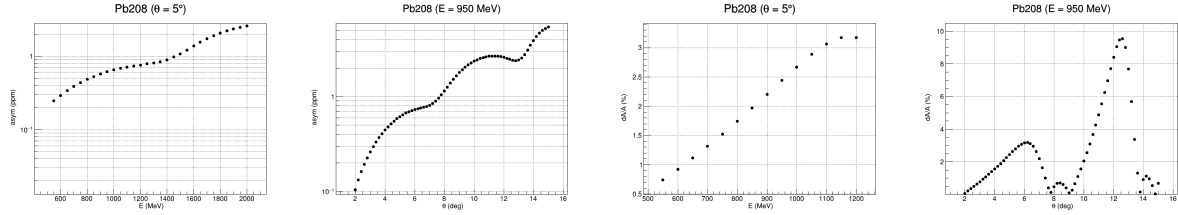


Figure 2.3: Asymmetry and sensitivity plot for  $^{208}\text{Pb}$ , which increases along beam energy and oscillating up along scattering angle. The sensitivity plot is calculated with 1% change in neutron radius and it shows the absolute value. So in small scattering angle region, there is a local maximum around  $6^\circ$

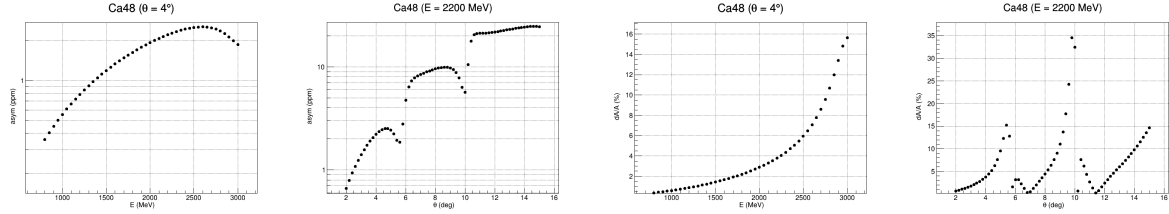


Figure 2.4: Asymmetry and sensitivity plot for  $^{48}\text{Ca}$ , the asymmetry maximize around 2500 MeV and there is a local maximum about  $4.5^\circ$ . As for sensitivity, there is regional maximum around  $5^\circ$

The design values of beam energy and scattering angle were chose to be 950 (2200) MeV and 5 (4) degree for  $^{208}\text{Pb}$  ( $^{48}\text{Ca}$ ). The beam energy of CREX is exactly 1-pass beam energy in CEBAF.

## 2.2 Continuous Electron Beam Accelerator Facility (CEBAF)

CEBAF is able to deliver multi-GeV continuous wave (cw) eletron beams of different energies and different intensities to 4 halls simultaneously. With the 12 GeV upgrade, the north and south 1497  $MHz$  LINAC each has 25 Superconducting Radial Frequency (SRF)

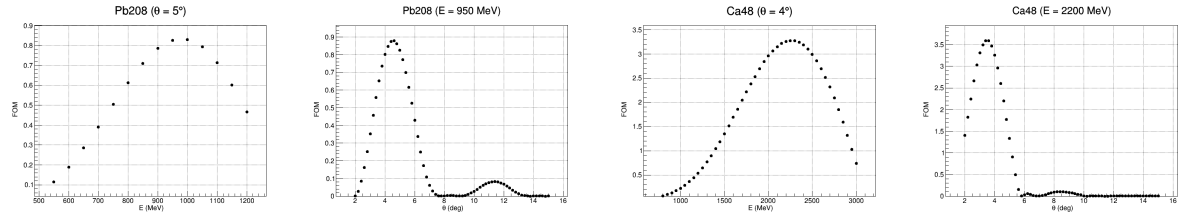


Figure 2.5: For both nuclei, FOM supports a small scattering angle. As for beam energy, FOM maximize around 950 (2200)  $GeV$  for  $^{208}\text{Pb}$  ( $^{48}\text{Ca}$ ).



Figure 2.6: Aerial view of JLab accelerator site, yellow line tells the position of the CEBAF accelerator and the 3 experimental halls are marked out as A/B/C (Hall D locates on the top left corner, after the exit of north LINAC). The accelerator tunnel is 30 *feet* ( $\sim 9$  m) underground and 10 *feet* ( $\sim 3$  m) high, with a circumference of about 7/8 *miles* (1.4 km). There are 2 superconducting LINAC (red lines), each of 1/4 *miles* (400 m). The pink part on the mid left is the location of injector. The right 2 plots show the tunnel and experimental halls under construction.

cryomodules, capable of accelerating electrons at the peak rate of 2.2 *GeV/turn*. Hall A, B and C can receive up to  $2.2 \times 5 = 11$  *GeV* cw beams and Hall D, with an extra half circle, can receive up to 12 *GeV* cw beams. With this design, different nuclear experiments can be carried out in different halls without interfering each other, theoretically.

As one can see in 2.7, laser pulse ( $\lambda = 780$  nm) from 4 lasers (Hall D laser is not shown in the plot) shoot in the electron gun (2 electron guns in total) that operates at  $-130$  kV to excite electrons, which interweaving with each other, forming a chain of electron bunches, with a phase difference of  $120^\circ$  from neaby bunches (Hall D doesn't have its own slit in the chopper, therefore it follows either Hall A or Hall C). This electron chain is sent into north LINAC by the injector, accelerated by both LINACs. After reaching desired energy, they will be kicked out at the exit of south LINAC and delivered to experimental halls (A, B and C) for various experiments.

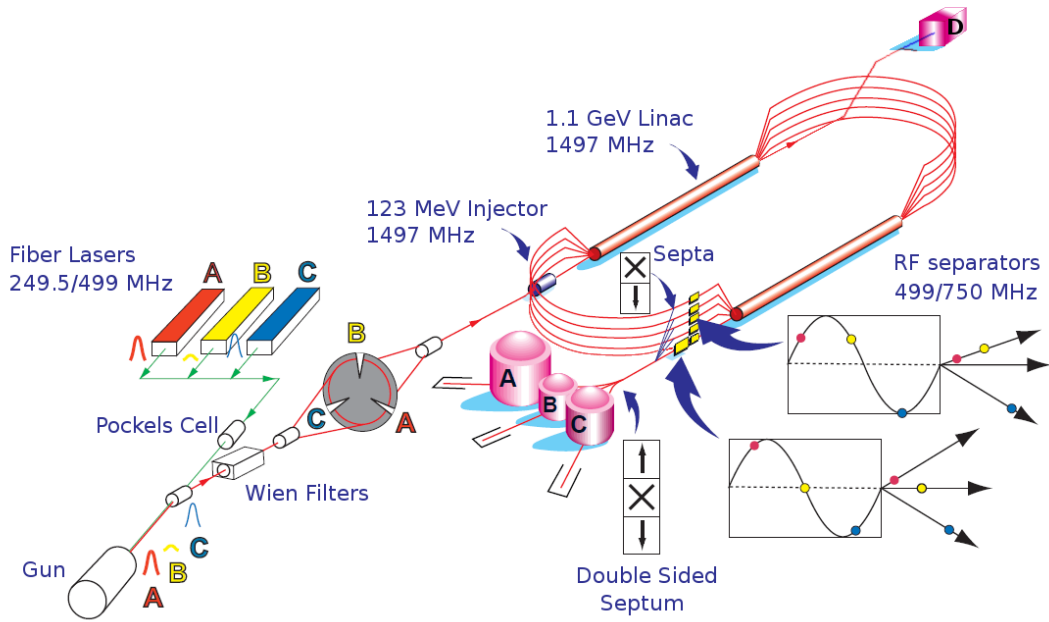


Figure 2.7: Schematic plot of CEBAF. Low energy beams will be kicked into higher arc, and high energy beams will go through lower arc. The magnetic field increases from higher arc to lower arc to keep electron trajectory have the same radius.

The maximum beam current of  $200 \mu A$  at (old) highest energy of  $5 GeV$  available at CEBAF is limited by the rf power ( $1 MW = 5 GeV \times 200 \mu A$ ) and by the beam power on the beam dump. While Hall B and D requires only tiny amount of cw beams (at  $nA$  level), it is actually Hall A and C that consume the produced electron beams, both can receive a few tenths to over one hundred  $\mu A$ .

While all 4 halls at JLab are dedicated to the study of nuclear structure, they focus on different aspects. Hall A concentrates on form factors of various nuclei, Hall B digs into generalized parton distributions, Hall C devotes itself to precise determination of valance quark properties in nuclei, and finally, the newly established Hall D explores origin of confinement through exotic mesons.

Because all 4 halls shared the same electron source and the same accelerator, cooperation is needed to make them work at the same time. In terms of electron source, PVES experiment usually has priority over other experiments to maintain the quality of polarized electron beam. As for the LINAC, if one hall wants a smaller energy, say  $1 GeV$ , then the LINAC power will be reduced to  $1 GeV/turn$ , which will be applied to other halls' electron beams, therefore limiting the highest energy available in other halls. Careful schedule is needed to make sure every hall get what they want.

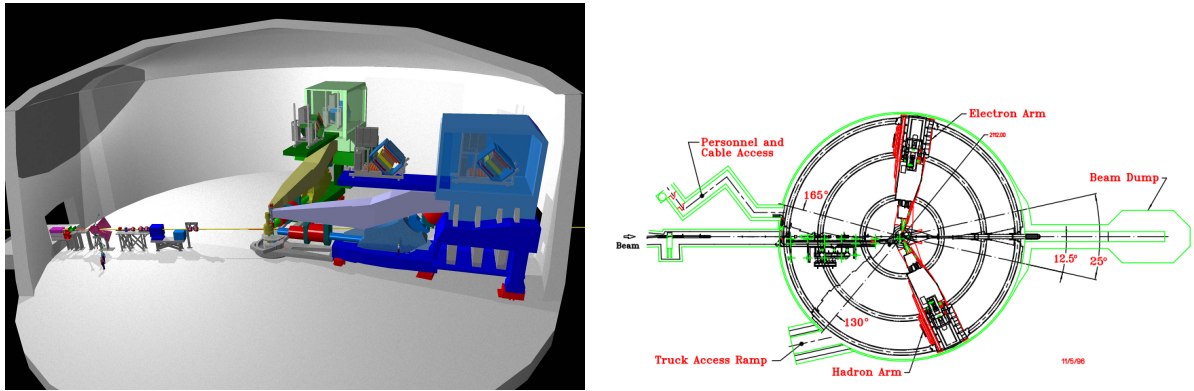


Figure 2.8: 3D and bird view of Hall A [16]. Originally, they were called High Resolution Hadron Spectrometer (HRHS) and High Resolution Electron Spectrometer (HRES), but they are essentially identical to each other and can be used interchangeably. so now they are called left arm (HRS-L) and right arm HRS (HRS-R).

## 2.3 Polarized Electron

### 2.3.1 Polarized Electron Source

PVES experiments motivate the development of polarized electron source, which require a highly stable polarized electron source that can produce high polarization electron beam at a wide range of intensity, from nA to A depending on the experiment. The source should be capable of rapid helicity reversal ( $\sim 100Hz$ ) with negligible impact on other properties of the beam.

Currently, GaAs-based semiconductor photoemission source is the only available polarized electron source for accelerators on the market. Historically, this kind of electron source was the only one that could satisfy high peak currents required by the low duty factors of the old accelerators and rapid helicity reversal required by PVES. That's why it is the only player on the market now. Over the past few decades, pulsed beam has been replaced by continuous beam while this electron source is inherited and further developed. The polarized electron source used by CEBAF can produce electron beam with polarization greater than 85%, much larger than the 37% polarization from its inauguration at SLAC. [3]

The design was first proposed independently by Garwin, Pierce and Siegmann [37] and by Lampel and Weisbuch [38]. The idea is straightforward: When circularly polarized laser light with carefully selected energy  $E_{gap} < h\nu < E_{gap} + \Delta$  shoot on the semiconductor, only electrons on the valance band  $P_{3/2}$  will be pumped into the conduction band  $S_{1/2}$ . The selection rule makes sure only those transitions that satisfy  $\Delta m_j = +1$  ( $-1$ ) can occur for circularly right (left) incoming photons, As shown in fig. ???. The ratio of the transition rate is also marked out in circle in the plot, which can be calculated from the Clebsch-Gordan coefficient easily. The excited electrons are polarized and different states have different pumping rate, so we have polarized electron beam now with

polarization as:  $P = (3-1)/(3+1) = 50\%$ , for both cases.

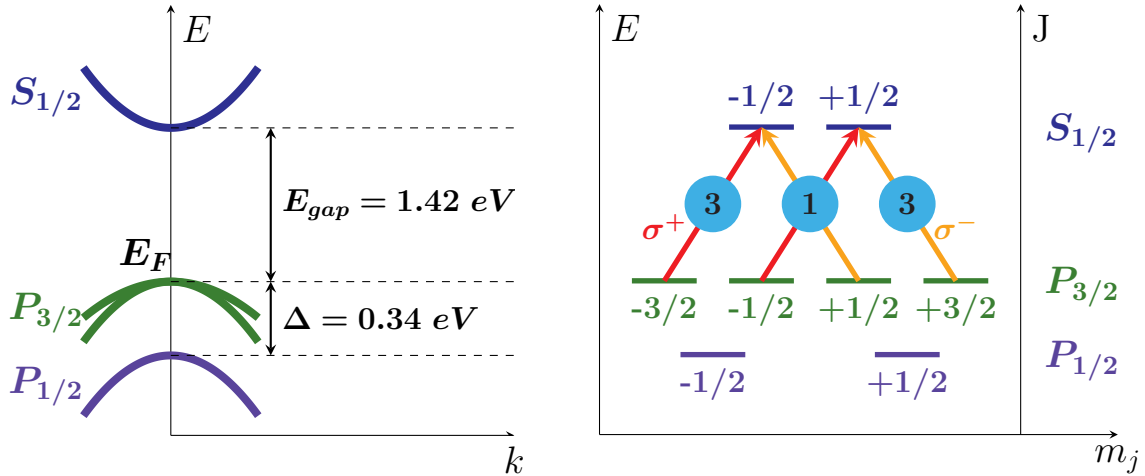


Figure 2.9: Excitation of polarized electrons

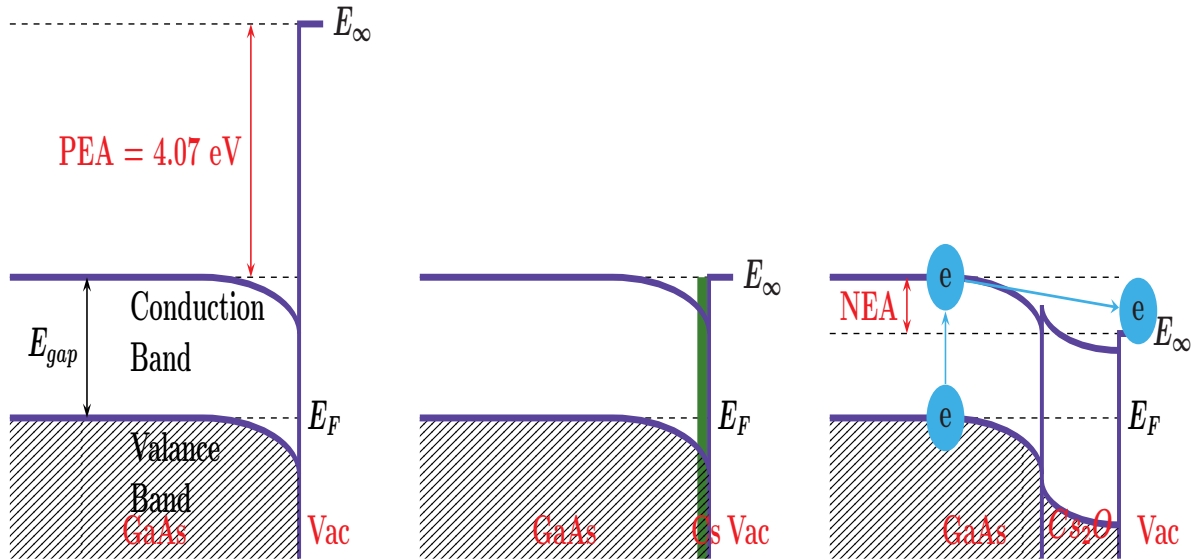


Figure 2.10: The energy band diagram of GaAs near its surface. Left: bare p-type GaAs, the large positive electron affinity (PEA) prevents electrons from escaping the surface; Middle: p-type GaAs with a cesiated surface, the electron affinity (EA) is 0, but electrons still can't escape the surface easily; Right: GaAs with layer of cesium oxide; the electron vacuum energy  $E_\infty$  is lowered to make a negative EA so that electrons can break free the surface easily. [17]

Then how can we liberate the polarized electrons from the material, without degenerating the polarization significantly. As shown in fig. ??, for bare GaAs, a 4.07eV electron affinity (EA) prevents any electrons from leaving the surface. To solve this problem, a

condition known as negative electron affinity (NEA) is used, that is to make the energy of electron in the vacuum just outside the surface lower than the conduction band energy by adding a layer a cesium oxide on the surface of pure GaAs semiconductor.

By the NEA technique, we were able to get polarized electron beam, but never reached the ideal 50% polarization, achieved polarization range between 25 to 43%. The polarization loss is due to spin dilution as electrons diffuse to the semiconductor surface. From this aspect, we can increase the polarization by reducing the thickness of the GaAs crystal. But obviously, even the thinnest GaAs crystal can't give us a polarization greater than 50%. New strategies are needed. It turned out the answer was strained GaAs. [17]

With a strained layer, the degeneracy of  $P_{3/2}$  state is splitted, only states with  $m_j = \pm 3/2$  will be pumped, therefore we will get 100% polarization, in ideal case. The real polarization achieved by CEBAF electron source is about 88%.

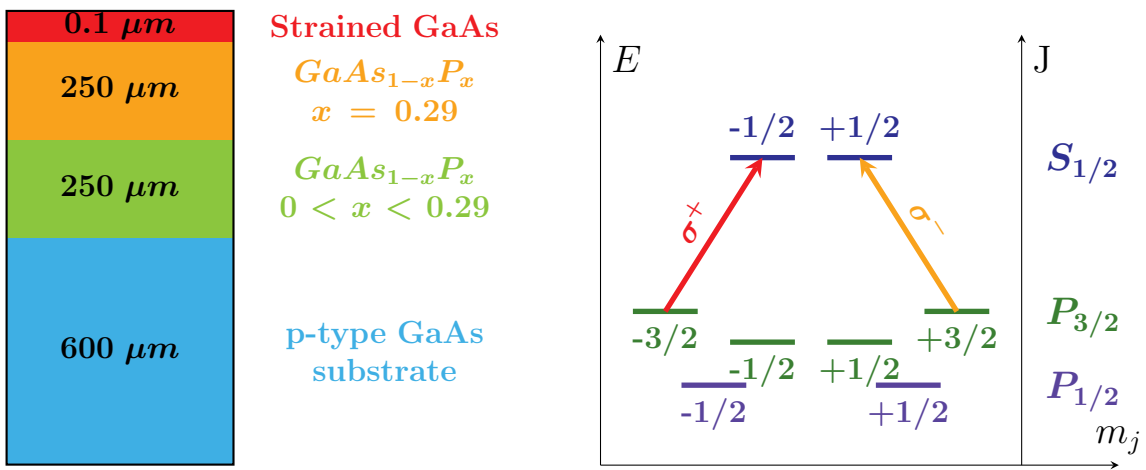


Figure 2.11: Strained GaAs

### 2.3.2 Polarization Control

#### Pockels Cell

Now that we can produce polarized electron beams, we need more control over the polarization of the electron beams. We should be able to flip the beam polarization quickly while keeping polarization as stable as possible. It is not easy and time consuming to manipulate the electron directly, while manipulating photons is much easier. One just need to reverse the circular polarization of the laser pulse, it will flip the electron beam polarization. The easiest way to do the job is a half-wave plane, by inserting it into or retracting it from the laser path, the phase of the laser pulse will be changed by  $\pi$ , flipping the laser circular polarization. But mechanical movement is not fast enough, the fast flipping of beam polarization is done by a component called Pockels Cell (PC), which is Rubidium Titanyle Phosphate (RTP) crystal. PC operates based on the Pockels effect, which is the production of birefringence in the crystal under an electric field, the

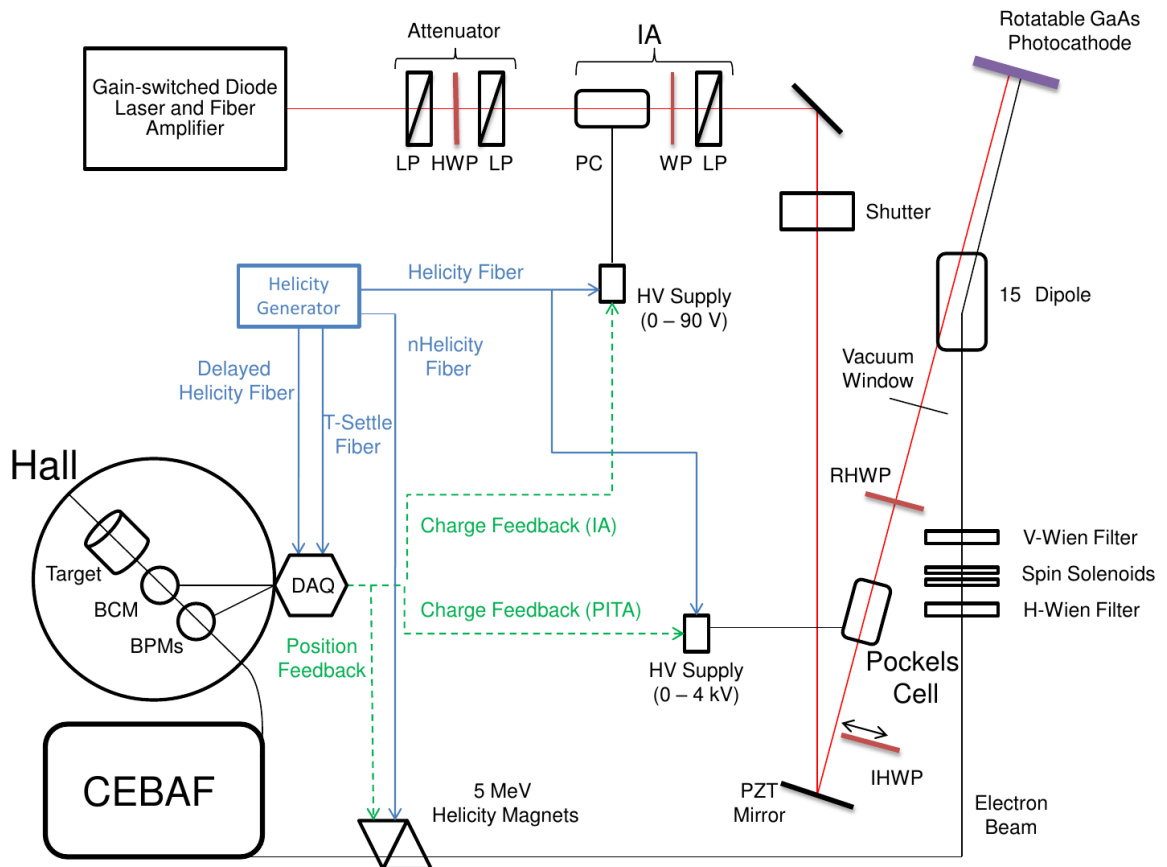


Figure 2.12: The laser system at the CEBAF injector

birefringence is proportional to the strength of the applied electric field. By applying appropriate high voltage ( $\sim 1.5$  kV), PC will act as a quarter wave plate (photon amplitude along fast and low axes  $E_x, E_y$  will have a phase difference of  $\pm\frac{\pi}{2}$  depending on the polarity of the applied electric field), converting linearly polarized laser beam into circularly polarized laser beam. And reverse the electric field polarity will reverse the polarization of the laser beam. This transition can be very fast, up to 1 kHz, with a dead time of about 60  $\mu$ s.

### Polarization Induced Transport Asymmetry (PITA, or Phase Induced Transmission Asymmetry) [?]

What we talked about above is the ideal case that PC will be an exact quarter wave plate and other optical components also work well, in reality, there is always deviation from the perfect circular polarization, resulting in systematic effect on beam position, spot size and intensity. If the deviation is polarization correlated, it will introduce a false asymmetry to our PV asymmetry measurement, which is called the PITA effect. The PITA effect is the dominant piece of HCBA, which, as we said before, is the largest false

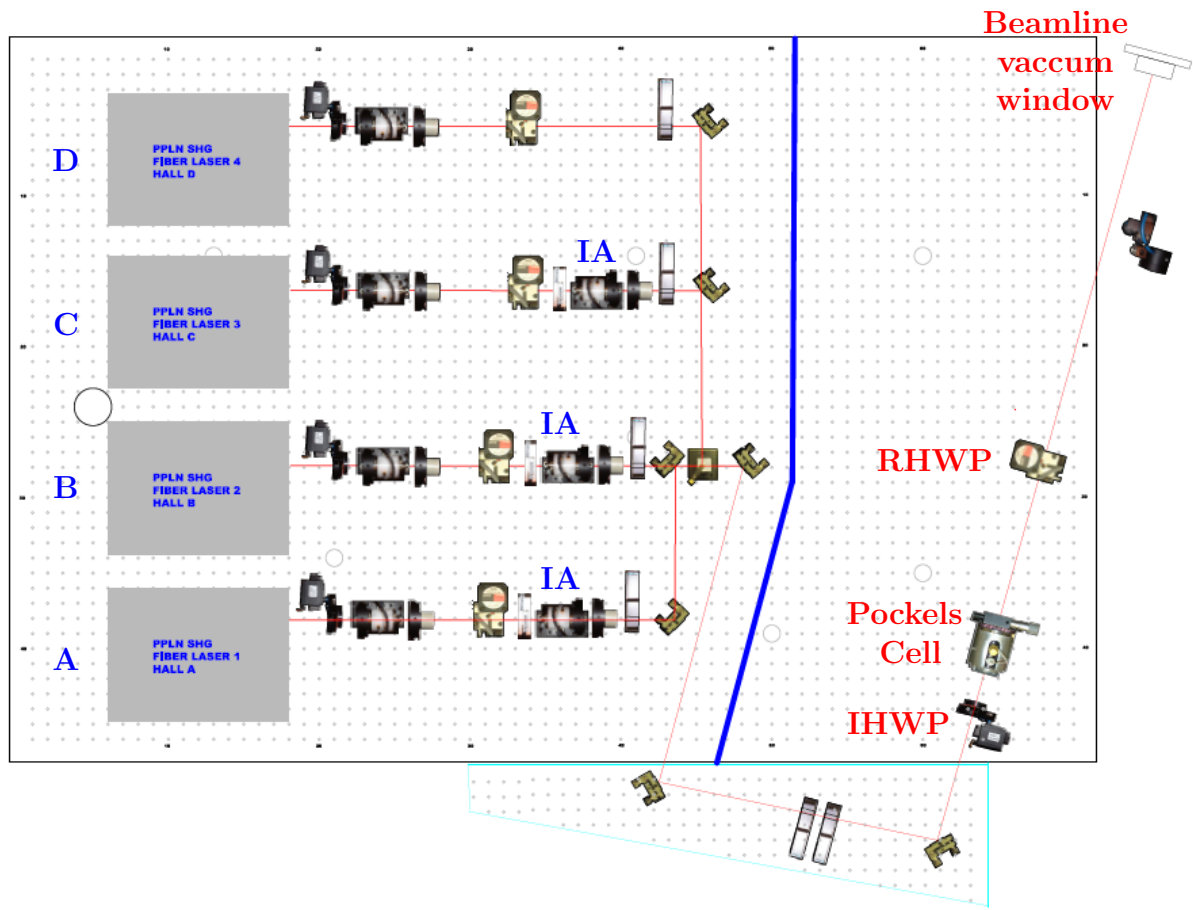


Figure 2.13: How the laser table actually looks like

asymmetry in our measurement.

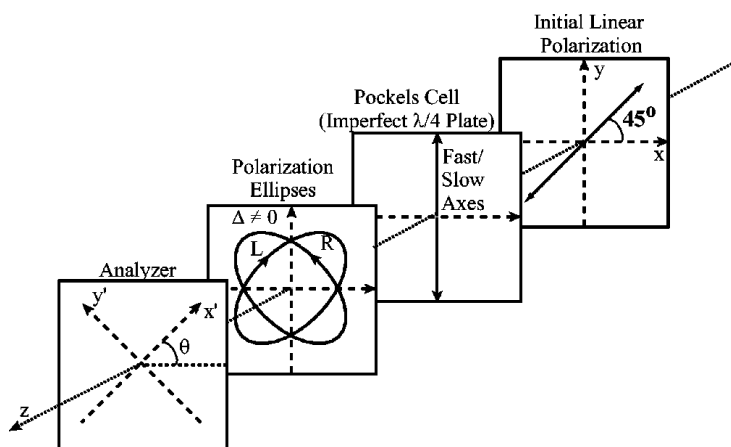


Figure 2.14: Phase shift by going through the PC

The PITA effect is characterized by the PC induced phase shift  $\delta$

$$\delta^{R(L)} = \mp \left( \frac{\pi}{2} + \alpha \right) - \Delta$$

where  $\alpha$  and  $\Delta$  represent the symmetric and asymmetric offset phase shift respectively. The resultant slightly elliptical beam has a residual linear component, leading to an intensity asymmetry (to first order):

$$\mathcal{A}_I = \frac{I^R - I^L}{I^R + I^L} = -\frac{\epsilon}{T} [\Delta \cos(2\theta)] \quad (2.9)$$

$\epsilon/T$  ( $<< 1$ ) defines the “analyzing power”,  $\epsilon = T_{x'} - T_{y'}$  and  $T = (T_{x'} + T_{y'})/2$ ,  $T_{x'(y')}$  is the transmission coefficient along the axis  $x'$  ( $y'$ ) of the downstream analyzer.  $\theta$  is the angle between the PC’s fast axis and the  $x'$  axis of the analyzer

Consider other optical elements along the laser path, like the RHP and the vacuum window, the unknown tiny birefringence in these components will also contribute to  $\Delta$ , resulting to a modified intensity asymmetry:

$$\mathcal{A}_I = \frac{I^R - I^L}{I^R + I^L} = -\frac{\epsilon}{T} [\cos(2\theta) \cdot (\Delta - \Delta^0)] \quad (2.10)$$

To minimize the intensity asymmetry, one would like to keep  $\Delta - \Delta^0$  as small as possible. Fortunately, *Delta* is tunable, by change the applied electric field. As shown in fig. 2.12, our charge feedback system will monitor the charge intensity asymmetry and automatically adjust the HV supplied to the PC to maintain a small  $\mathcal{A}_I$ . Over CREX, the average charge intensity asymmetry is ??? ppm.

As you may see in fig. 2.12, the charge feedback system also controls the HV supply of the Intensity Attenuator (IA), which, together with the slit in beam chopper, controls the intensity of electron beams. So, IA also plays a key role in achieving a small charge intensity asymmetry by equalizing beam intensity across helicity states.

A optical element called Rotatable Half-Wave Plate (RHWP) lies downstream the PC, it help to equalize any residual linear polarization left in the PC to establish a Quantum Efficiency (QE) independence of helicity.

## Slow Helicity Reversal

Fast reversal of the PC can minimize a lot of random noise from beam and target density fluctuations, nevertheless, some helicity correlated (HC) false asymmetries remain, such as electronic pickup between accelerator electronic systems and the experimental DAQ system or the residual birefringence effect. It is the job of slow helicity reversal to cancel these systematic false asymmetries.

There are 2 methods to make slow helicity reversal – the Insertable Half-Wave Plate (IHWP) and the double Wien Filters. Prior to 2009, IHWP was the only available approach at CEBAF to do slow helicity reversal. A new mechanism was introduced

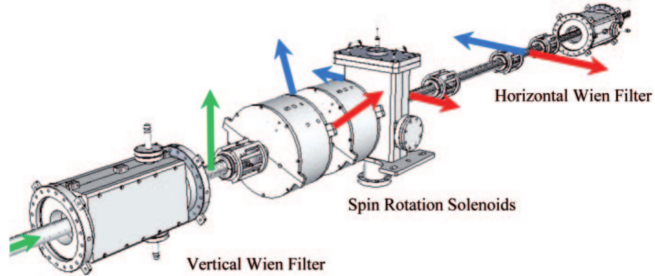


Figure 2.15: Schematic plot of double wien filter, electron beam travels from left to right. [18]

during PREX-I and Qweak experiments for better systematic precision – the wien filter.

The IHWP lies upstream of the PC, it is the easiest way to reverse the beam helicity by inserting or retracting the IHWP. With slow helicity reversal, we can identify the possible systematic uncertainties. The idea is simple, assume the true and a systematic false asymmetry to be  $A_0$  and  $\Delta A$ , then what we measure by inserting (retracting) the IHWP will be:

$$A^{+(-)} = \pm A_0 + \Delta A \quad (2.11)$$

Because IHWP doesn't affect the systematic uncertainty, so the true asymmetry will be:

$$A_0 = \frac{A^+ - A^-}{2} \quad (2.12)$$

As easy and good as IHWP, it resolves only some of the HC beam variations, namely the residual birefringence from the laser optical system and is powerless in dealing with other HC effects, like HC beam size variations that are introduced via PC focusing [18], which is addressed by the wien filter. The wien filter manipulate the electron spin directly by electromagnetic field without affecting the electron movement and is able to achieve any spin orientation. It consists of 2 wien filters and 2 intervening solenoids between them. A wien filter is such a cavity with proper electric and magnetic field ( $qE = qvB$ ), perpendicular to each other and to the electron moving direction, so that it rotates electron spin only. Electrons coming from the photocathode are longitudinally polarized, the vertical wien filter will make the electron spin vertical oriented, so that it can be rotated to left/right by the following spin solenoid, depending on the polarity of the solenoid, a wien flip means to change the polarity of the spin solenoid. Finally, the horizontal wien filter will fine tune the spin direction to optimize the longitudinal polarization in the experimental hall. Note that electrons exit the double wien filters are not longitudinally polarized, because electron spin will precess when travel through the accelerator, causing a rotation in the horizontal plane. Therefore, a carefully selected initial spin direction is needed to make sure the spin is (anti) parallel to electron momentum at target.

This tells us another function of the wien filter, to set a non-longitudinal initial spin to cancel out the shift caused by spin precession during acceleration, so that we have

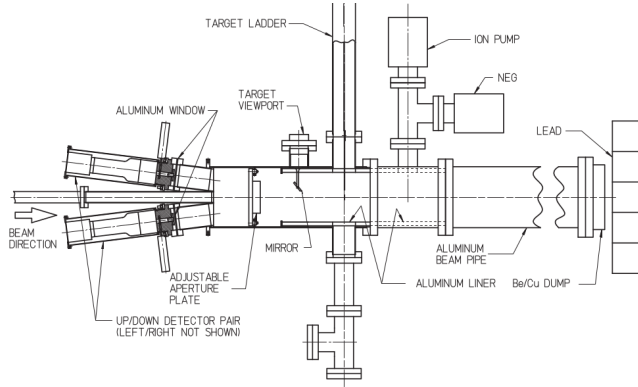


Figure 2.16: Schematic plot of the Mott polarimeter, it has 4 symmetric detector ports (up and down, left and right – which is not shown in the plot). The back scattering angle is  $172.6^\circ$ , where we have the highest analyzing power from theoretical calculation of the Sherman function. [19]

exactly longitudinally polarized electron beam at target.

With both IHWP and Wien filter, we are able to cancel most systematic false asymmetries, achieving very small systematic errors.

### 2.3.3 Polarimeters

Now that we have polarized electron beams, we still need to measure its polarization. We have 3 polarimeters to measure the beam polarization: the Mott polarimeter at injector and the Compton and Moller polarimeter in Hall A. As their names imply, they use the cross section asymmetry of the Mott, Compton and Moller scattering to measure the polarization of the electron beam. Since these are all pure QED processes, their cross sections are well understood and analyzing powers are easily calculable to high order.

While both Mott and Moller measurement are invasive, they can't be done frequently (Moller measurement happens about every 10 days). the non-invasive Compton polarimeter is the only choice for beam polarization monitoring. Mott polarimeter measures the beam polarization before it enters the accelerator, so it is not used for the determination of beam polarization during PREX-II/CREX.

#### Mott Polarimeter

The 5-MeV Mott polarimeter lies at the CEBAF injector, between the Wien Filter and the Injection Chicane, it measures the single spin cross section asymmetry of 5 MeV electron beams scattered off a high-Z target. Comparing the measurement to the Sherman Function [39], the analyzing power, will tell us the transverse polarization of the electron beam:

$$\mathcal{A}_{LR} = \frac{N_L - N_R}{N_L + N_R} = S(\theta) \mathbf{P} \cdot \hat{\mathbf{n}} \quad (2.13)$$

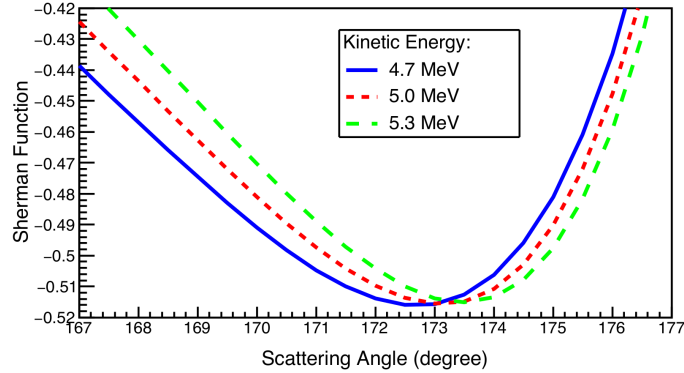


Figure 2.17: The Sherman Function for different high-Z targets at 5 MeV, dots represent experimental measurement.

$\hat{\mathbf{n}}$  is the unit normal vector of the scattering plane. The same formula applies to the Up-Down asymmetry. Because the asymmetry comes from the coupling of electron's spin and the induced magnetic field by the nucleus in the electron's rest frame (spin-orbit coupling), the scattering potential is:

$$V(r, \mathbf{L}, \mathbf{S}) = V_{Coulomb} + V_{so}(r, \mathbf{L}, \mathbf{S}) = \frac{Ze}{r} + \frac{Ze^2}{2m^2r^3} \mathbf{L} \cdot \mathbf{S} \quad (2.14)$$

So only transverse polarization can be measured using Mott polarimeter, rather than the longitudinal one we desire at the target. Nevertheless, it provides an independent check of the initial beam polarization from the injector and its high precision (its total uncertainty can be as small as 0.61% [19]) helps to normalize the polarization measurement in the experimental halls.

### Compton Polarimeter

The Compton polarimeter locates at the entrance to hall A (about 20 m upstream the target chamber), using the elastic scatter between polarized photon and electron to measured the polarization of the electron beam. As shown in fig 2.18, when the compton polarimeter is on, the electron beam will be bent into the Compton Chicane to interact with the polarized photons nearly head-on (a tiny crossing angle of 23.5 mrad). The Fabry-Perot Cavity is locked to and filled with circularly polarized (> 99%) green laser beam ( $\lambda = 532 \text{ nm}$ ,  $E = 2.334 \text{ eV}$ ). The back-scattered photons will be detected by a GSO (low energy) or PbWO<sub>4</sub> crystal calorimeter right of the interaction region, while the electron beam will be bent back to the beam pipe to bombar the target. Due to interaction with photons, the scattered electrons will be less energetic than the incoming ones. So under the same dipole field, the scattered electrons will be bent more than the non-interacting electrons, as shown by the red dash line in Fig. 2.18. This seperation allow us to measure the scattered electrons, together with measurement of scattered photons, we can identify and scattering asymmetry and then the polarization of the electron beam.

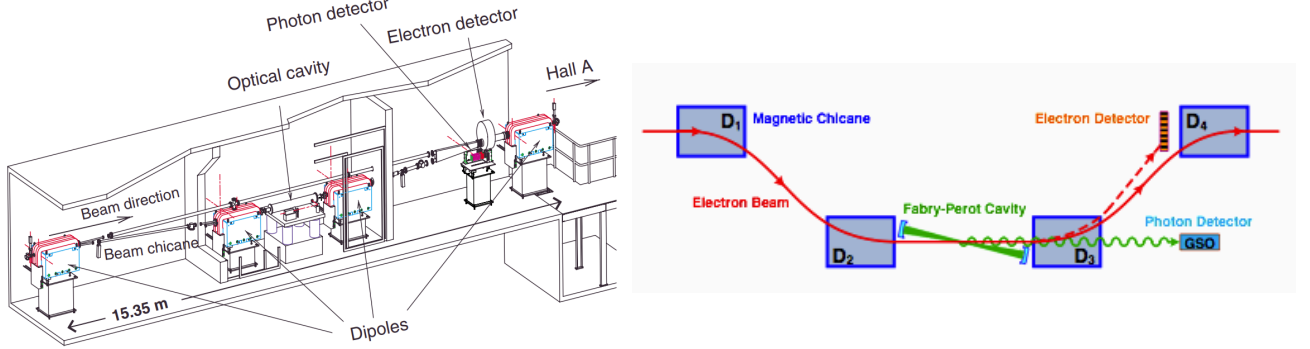


Figure 2.18: Left: Compton Chicane [20]; Right: Schematic plot of electron/photon scattering

The energy of the scattered photon will be:

$$E_\gamma \approx E_{laser} \frac{4a\gamma^2}{1 + a\theta_\gamma^2\gamma^2} \quad (2.15)$$

where  $\gamma = E_{beam}/m_e$  is the Lorentz factor of the incoming electron,  $a = \frac{1}{1+4\gamma E_{laser}/m_e}$  and  $\theta_\gamma$  is the scattering angle w.r.t. the electron moving direction. The maximum energy of the scattered photon appears at  $\theta_\gamma = 0$ , which is back scattering. For PREX-II (CREX) beam energy of 0.95 (2.2)  $GeV$ ,  $E_\gamma^{max} \sim 32.55$  (167.02)  $MeV$ .

Define  $\rho = \frac{E_\gamma}{E_\gamma^{max}}$ , the cross section for unpolarized Compton scattering will be:

$$\frac{d\sigma}{d\rho} = 2\pi r_0^2 a \left[ \frac{\rho^2(1-a)^2}{1-\rho(1-a)} + 1 + \left( \frac{1-\rho(1+a)}{1-\rho(1-a)} \right)^2 \right] \quad (2.16)$$

$r_0 = \frac{\alpha\hbar c}{mc^2}$  is the classical electron radius; then the analyzing power will be:

$$\mathcal{A}_l = \frac{\sigma_{\Rightarrow}^{\rightarrow} - \sigma_{\Rightarrow}^{\leftarrow}}{\sigma_{\Rightarrow}^{\rightarrow} + \sigma_{\Rightarrow}^{\leftarrow}} = \frac{2\pi r_0^2 a}{d\sigma/d\rho} (1 - \rho(1+a)) \left[ 1 - \frac{1}{(1 - \rho(1-a))^2} \right] \quad (2.17)$$

The measured asymmetry will be:

$$\mathcal{A}_{exp} = \mathcal{P}_e \mathcal{P}_\gamma \mathcal{A}_l = \frac{N_\gamma^R - N_\gamma^L}{N_\gamma^R + N_\gamma^L} \Rightarrow \mathcal{P}_e = \frac{\mathcal{A}_{exp}}{\mathcal{P}_\gamma \mathcal{A}_l}$$

The advantage of the Compton polarimeter is that it can tolerate quite high current (up to  $\sim 200 \mu A$  at JLab), plus its non-invasive operation make it a beam polarization monitor. The disadvantage is, comparing to Mott or Moller polarimeter, its analyzing power is quite low at  $GeV$  energy level, while increase the beam energy will lead to high

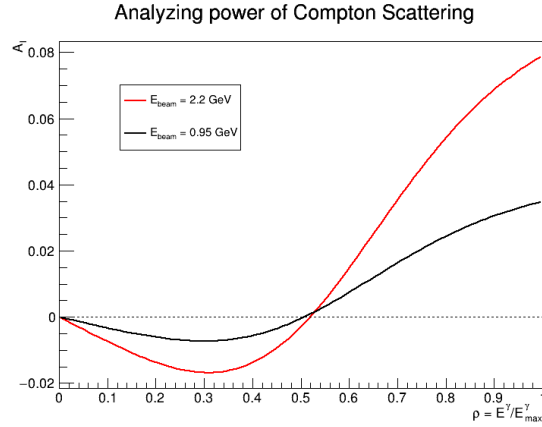


Figure 2.19: The Compton analyzing power increases with electron energy. Note that the analyzing power will change sign at  $\rho \sim 0.5$  for both PREX-II and CREX beam energies.

background in the photon detection due to synchrotron radiation. Overall, the Compton polarimeter is able to achieve a 1% absolute systematic uncertainty.

## Moller Polarimeter

The Moller polarimeter lies downstream of the Compton polarimeter and upstream of the target chamber. It uses elastic electron-electron scattering to measure the asymmetry due to different beam polarizations.

$$\begin{aligned} \frac{d\sigma}{d\Omega} &= \frac{d\sigma_0}{d\Omega} \left( 1 + \sum_{i,j=x,y,z} \mathcal{P}_b^i \cdot \mathcal{P}_t^j \cdot A_{ij}(\theta_{CM}) \right) \\ \frac{d\sigma_0}{d\Omega} &= \frac{\alpha^2}{s} \left( \frac{4 - \sin^2 \theta_{CM}}{\sin^2 \theta_{CM}} \right)^2 \end{aligned} \quad (2.18)$$

With  $\frac{d\sigma}{d\Omega} d\Omega$  being the unpolarized moller scattering cross section,  $s$  is the Mandelstam variable:  $s = 2m_e(E + m_e) \approx 2m_e^2\gamma$ ,  $\mathcal{P}_b$  ( $\mathcal{P}_t$ ) the polarization of beam (target).  $\theta_{CM}$  and  $A_{ij}$  the scattering angle and analyzing power in CoM frame.

Assuming incoming electrons move in the  $z$  direction and the scattering happens in the  $xz$  plane, then in the ultra-relativistic limit:

$$\begin{aligned} A_{zz} &= \frac{\sin^2 \theta_{CM} (7 + \cos^2 \theta_{CM})}{(3 + \cos^2 \theta_{CM})^2}, & A_{xx} = -A_{yy} &= \frac{\sin^4 \theta_{CM}}{(3 + \cos^2 \theta_{CM})^2} \\ A_{xz} = A_{zx} &= \frac{2 \sin^4 \theta_{CM} \cos \theta_{CM}}{\gamma (3 + \cos^2 \theta_{CM})^2}, & A_{xy} = A_{yz} = A_{yz} = A_{zy} &= 0 \end{aligned} \quad (2.19)$$

When  $\theta_{CM} = 90^\circ$ ,  $A_{zz}$  is maximized to be  $\frac{7}{9}$ . This is what we choose in the moller polarimeter.

The polarized target electrons come from magnetized Fe-alloy foil, which is saturated

by a very strong ( $4\text{ T}$ ) longitudinal magnetic field created by superconducting Helmholtz coils, as shown in Fig. 2.20. So Eq. 2.18 is simplified to:

$$\frac{d\sigma}{d\Omega} = \frac{d\sigma_0}{d\Omega} (1 + \mathcal{P}_b^z \cdot \mathcal{P}_t^z \cdot A_{zz}(\theta_{CM})) \quad (2.20)$$

The moller pair (the scattered incident electrons and recoil target electron) centered around  $\theta_{CM} = 90^\circ$  ( $\theta_{lab} < 3^\circ$ ), are seperated from the undeflected beam by set of magnets, then goes through collimators (at the exit of dipole, not shown in Fig. 2.20) that define the acceptance, and finnally is detected by electron detectors in coincidence. The measreud asymmetry between spin-parallel and anti-parallel cross section is:

$$A_{exp} = \frac{N^+ - N^-}{N^+ + N^-} = \mathcal{P}_b \mathcal{P}_t \langle A_{zz} \rangle \Rightarrow \mathcal{P}_b = \frac{A_{exp}}{\mathcal{P}_t \langle A_{zz} \rangle} \quad (2.21)$$

with  $\langle A_{zz} \rangle$  being the average analyzing power over the acceptance, which was about 0.75 for PREX-II and CREX.

The target foil was cooled by conduction through the target, whose temperature will climb quickly with increase beam current, causing damage to target polarization. Therefore moller polarimeter can only operate at very low current ( $\lesssim 1\mu\text{A}$ ). The extrapolation from polarization measurement at low current to high current where PREX-II and CREX run at, is a large source of systematic uncertainty. During PREX-II and CREX, the target polarization was measured to be  $\mathcal{P}_t \sim 8\%$  leading to an effective analyzing power of  $A_{eff} = \mathcal{P}_t \langle A_{zz} \rangle = 6\%$ . This relative large analyzing power makes moller measurement quite precise. Overall, Moller polarimeter in Hall A can achieve a systematic uncertainty less than 1%.

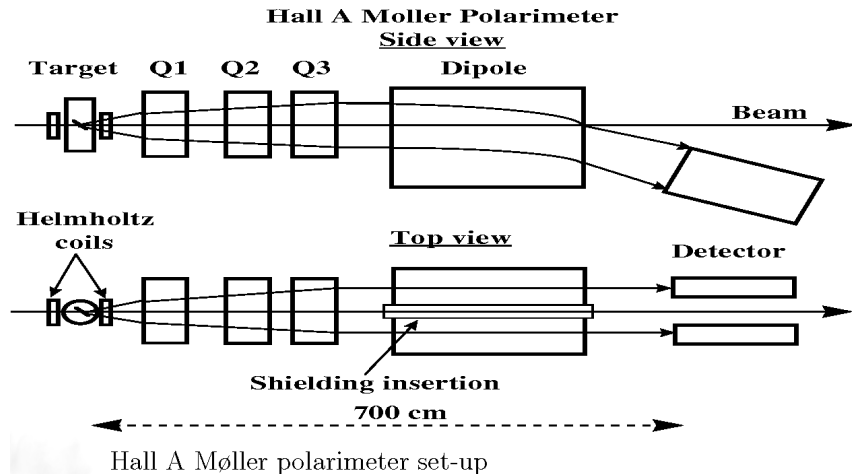


Figure 2.20: Møller Polarimeter

## 2.4 Monitors

Besides beam polarization, another significant source of systematic uncertainty is the beam false asymmetry – the difference in beam position, angle, energy and current between different helicity states. Because there is no way to ensure exactly the same beam parameters between different helicity states, even with fast helicity flipping. We monitored these variables with redundant specialised devices – Beam Position Monitors (BPMs) and Beam Current Monitors (BCMs). For PREX-II and CREX, we had another independent monitor system – Small Angle Monitors (SAMs). These monitors were able to measure the beam difference as precise as:

$$\Delta x \sim 1 \mu\text{m} \quad \Delta x' \sim 1 \text{ mrad} \quad \Delta p/p \sim 0.0004 \quad \Delta I/I \sim 100 \text{ ppm}$$

(FIXME)

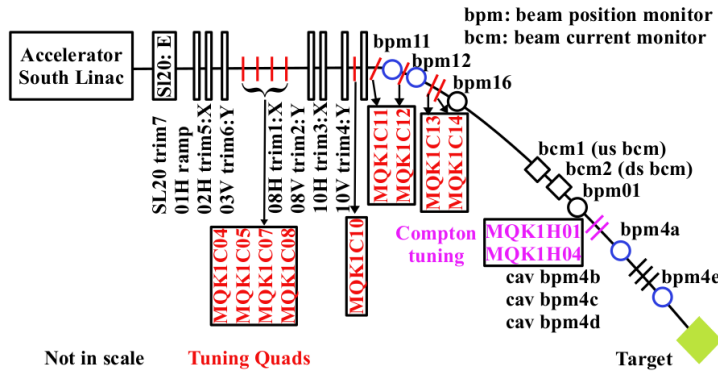


Figure 2.21: Schematic plot of Hall A beam monitor system and beam modulation system

### 2.4.1 BPMs

Hall A has a series of BPMs along the beam pipe leading to the target chamber to monitor the beam conditions, among them, 6 switched electrode electronics (SEE) stripline BPMs are important to PREX-II and CREX, their records are used to extract beam parameters. These 6 key BPMs are shown in Fig. 2.21. BPM4A and BPM4E locate 7.524 m and 1.286 m upstream of the target chamber, they are used to determine the beam position and angle on the target. BPM11 and BPM12 are positioned on the arc area to measure the beam energy using the bending radius of the electron trajectory. BPM1 and BPM16 are backup monitors.

A stripline BPM consists of a 4-wire antenna array of open ended thin wire striplines, the voltage induced by the electron bunches in each electrode is sensitive to beam position. Therefore we can extract  $(x', y')$  positions from opposite 2 pickup signals.

$$x' = \frac{1}{S_x} \frac{X_p - X_m}{X_p + X_m} y' = \frac{1}{S_y} \frac{Y_p - Y_m}{Y_p + Y_m} \quad (2.22)$$

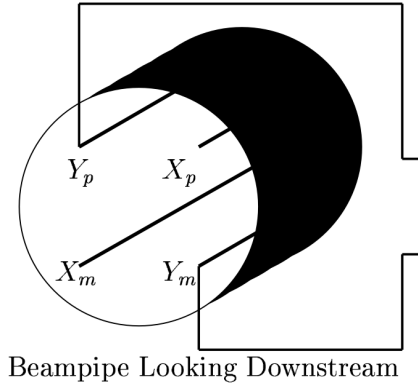


Figure 2.22: Schematic plot of stripline BPM

where the proportional constant  $S_x$  ( $S_y$ ) is the position sensitivity. The pickup voltage responds linearly to beam displacement when the displacement is small. In the case of Hall A BPMs, the 4 striplines are rotated 45° w.r.t. to hall coordinate system, so a 45° rotation is needed to recover hall (x, y) from extracted BPM (x', y').

Besides these stripline BPMs, PREX-II and CREX also utilized 3 cavity BPMs (see discussion below), shown as bpm4b/c/d between bpm4a and bpm4e in Fig. 2.21, to measure beam conditions for low current calibration runs, because stripline BPMs don't work when beam current is lower than 0.5  $\mu A$ . These cavity BPMs were not used in normal production runs.

## 2.4.2 BCMs

One technique to measure beam current is current transformation. Various BCMs based on this idea may have different designs, features and performances, the key component is the same – current transformer (CT). When beam bunch travel through the beam pipe, it will induce a magnetic field in the beam pipe (the core), which in turn will induce a current in the secondary winding (toroid), whose output is proportional to the beam current. To make a precise measurement, it is important to shield any outside magnetic field and separate the segment of beam pipe where the BCM lies in from the rest.

The BCM system in Hall A consists of two radio frequency (rf) cavities and an unseer monitor in between, the unseer monitor is a parametric current transformer (PCT), which will output a DC voltage equivalent to 4 mV per  $\mu A$  of beam [21]. In PREX-II and CREX, the Unser monitor was not used for beam current measurement, because its voltage output drifted quickly after only a few minutes of running, instead, it was used to calibrate the rf-cavity monitors on either side of it, whose readout was what we used for runtime beam current measurement.

A rf cavity is a metallic chamber that sustains an electromagnetic (EM) field (infinite number of resonant EM modes), by special design of its shape, a particular EM mode can efficiently transfer energy to or from a charged particle. The frequently heard accelerating cavity need to provide a electric field along beam velocity direction. While a decelerating

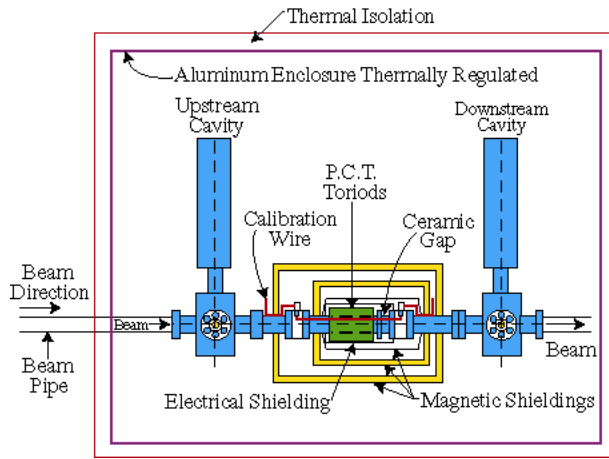


Figure 2.23: Hall A BCM system [21]

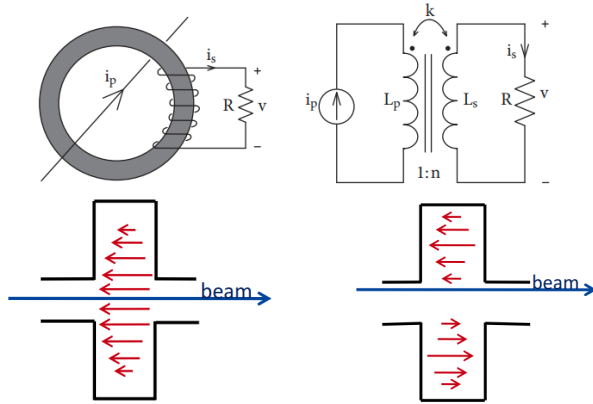


Figure 2.24: Up: Schemtaic plot of current convertor; Down:  $\text{TM}_{010}$  and  $\text{TM}_{110}$  modes, the red arrows are electric field

cavity, which will absorb energy from the coming charged particles, can be used as beam diagnostic monitors. The induced voltage is proportional to the traversing charge  $q$ :

$$V = 2k_{loss}q \quad (2.23)$$

where  $k_{loss}$  is the loss factor, which depends only on the electric field distribution, therefore is sensitive to beam position and particle velocity. To measure beam intensity, one would prefer the EM mode whose electric field doesn't depend on  $r$  position, these are  $\text{TM}_{010}$  like modes; while for measurement of beam position, exactly the opposite is wanted, the electric field should have an azimuth angle and  $r$  dependence, which are  $\text{TM}_{110}$  like modes.

The 2 rf-cavity current monitors are of Pill box type (the electric field is concentrated near axis, while the magnetic field is concentrated at outer cylindrical wall), which operates at  $\text{TM}_{010}$  mode. The voltage readout will be downconverted to lower frequencies signals, then filtered, amplified and further precessed before writing into the data

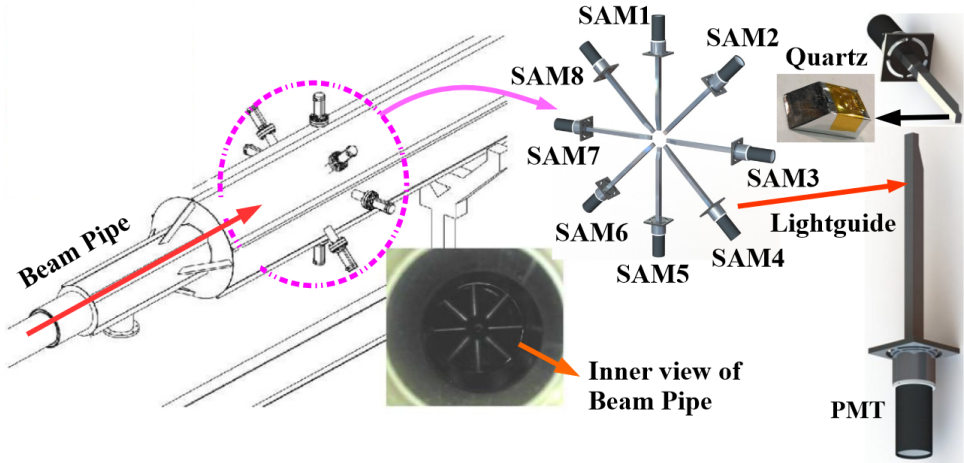


Figure 2.25: Layout of SAMs[?] ??

stream. Due to non-linearity at low current region, actually 3 signals (the same signal with different gains: x1, x3 and x10) will be recorded [? ].

### 2.4.3 SAMs

For further understanding of beam dynamics, electronic noise and possible target boiling effect, a luminosity monitoring system, called the small angle monitors, was installed in the dump pipe, about 7 m downstream of the target pivot. As shown in Fig. ??, the SAMs system consist of 8 detector modules, symmetrically positioned around the dump pipe. Each detector module has a quartz tile (active detector), attached to a lightguide, the Cherenkov light will be read out by a PMT at the end of the lightguide. As its name implies, SAMs are designed to monitor small angle ( $\sim 1^\circ$ ) scattered and secondary flux from the target, thus it can also be used to inspect the target conditions, e.x. a bubble in the target that forms and disappears within one helicity window is unknown to both BPMs and BCMs, but SAMs will see it. SAMs' readout is sensitive to beam parameters, e.x., the sum of a symmetric pair monitors is sensitive to change in beam current and energy while their difference tells the fluctuation in beam position and angle. The symmetric design helps to disentangle these beam parameters. So it provide an independent check of the measurement of BPMs and BCMs and can be used to eliminate possible beam or electronic noise.

### 2.4.4 Beam Modulation

Another system we see in Fig. 2.21 is the beam modulation system, which lies in beamline arc right after Beam Switch Yard where electron chains are separate into Hall A/B/C beams. It consists of 6 air-core coils and an energy vernier in the last cavity of south LINAC, the total number of 7 coils provides a redundancy w.r.t. the free number

of degrees of beam phase space, making sure to cover all beam phase space at target. Coil (trim) 1, 3, 5 are responsible for modulating beam x position and coil 2, 4, 5 will modulate beam y position. These coils (vernier) are driven by a VME-DAC, which in turns is controlled by the parity DAQ. It takes 4.267 s for each coil (vernier) to modulate the beam, a whole modulation cycle takes 85.68 s ( $\sim 1$  beam modulation every 10 mins during run time).

The beam modulation system was used for false asymmetry correction, together with regression. When beam was modulated, BPMs and detectors will record corresponding change in their readout, to calculate detector sensitivity w.r.t. jitter in beam parameters. Therefore, the modulation should be much larger than the natural jitter in the beam, a typical position modulation will be about  $100 \mu\text{m}$  (FIXME) and the energy vernier will result in a beam displacement of  $0.75 \text{ mm}$  in BPM 11/12.

## 2.5 Target

For the sake of statistics, the designed current was quite large, as shown in Table. ???. With such high current, the electron beam will deposit quite a lot of heat on the target, it will be a disaster if we can't take away these heat as soon as possible to keep a stable target temperature. For PREX-II, because Pb itself is not a good thermal conductor ( $35 \text{ W/m} \cdot \text{K}$ ), auxiliary diamond foils ( $> 1000 \text{ W/m} \cdot \text{K}$ ) were used to form a D-Pb-D sandwich target to help heat dissipation. The thickness of the diamond foil matters, one lesson we learned from PREX-I was that with thin ( $0.15 \text{ mm}$ ) diamond foil, the thermal conductivity of the diamond foil dropped greatly (from  $1000 \text{ W/m} \cdot \text{K}$  to  $100 \text{ W/m} \cdot \text{K}$ ) after about 1 week of running with  $70 \mu\text{A}$  cw beam, resulting in some Pb targets melted. While a thicker diamond foil ( $0.25 \text{ mm}$ ) will protect Pb foils from melting under the same conditions. In PREX-II, a factor of 2 safety margin was adopted, conservatively assume 1 week running for each Pb target, 35 PAC days of beam time requires 5 targets, and we deployed 10 isotopically pure Pb sandwich targets with thick diamond layers to ensure the success of PREX-II, each new target was able to sustain up to  $85 \mu\text{A}$  cw beams.

While Ca itself is an excellent thermal conductor, no need for auxiliary materials and higher current can be applied. Isotopically pure  $^{48}\text{Ca}$  (the original target we used had a purity of 95.99%) is much more expensive than pure  $^{208}\text{Pb}$  target, so only one  $^{48}\text{Ca}$  target was prepared for CREX. After the target accident, the new  $^{48}\text{Ca}$  target was a stack of 3 separated foils with similar total thickness.

Targets were firmly mounted in bays of target ladders, whose axes were perpendicular to the beam line. The ladder was movable along its axis by an AC servo-motor, which can receive remote instructions through internet. The motion along ladder axis can be precise to  $\sim 12 \text{ nm}$ . There are 2 target ladders in total, one for production targets and the other one for calibration targets. The production-ladder had 10  $^{208}\text{Pb}$  targets, two Calcium isotope targets:  $^{40}\text{Ca}$  and  $^{48}\text{Ca}$ , and 4 other calibration and diagnostic targets, 16 target slots in total. The calibration-ladder had 5 targets, a carbon hole, a watercell, a thin C foil, a thin natural Pb and a thin  $^{40}\text{Ca}$  target. The calibration-ladder was rotated

45° w.r.t. the production ladder, which was along the lab x axis, as shown in Fig. 2.26 and 2.27.

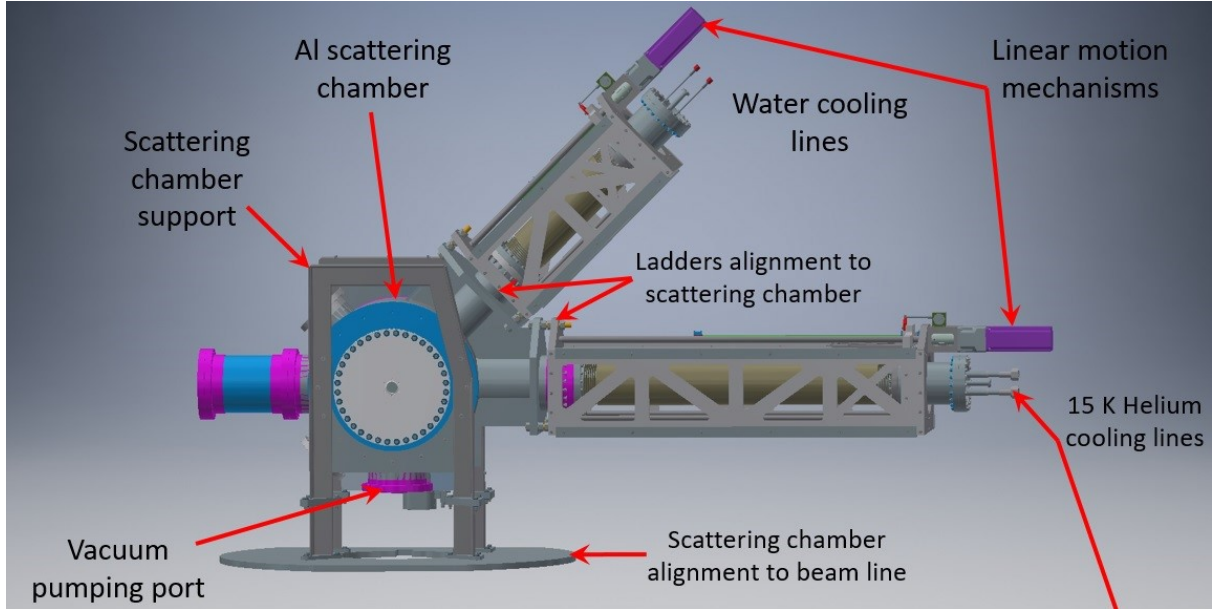


Figure 2.26: Scattering chamber of PREX-II/CREX

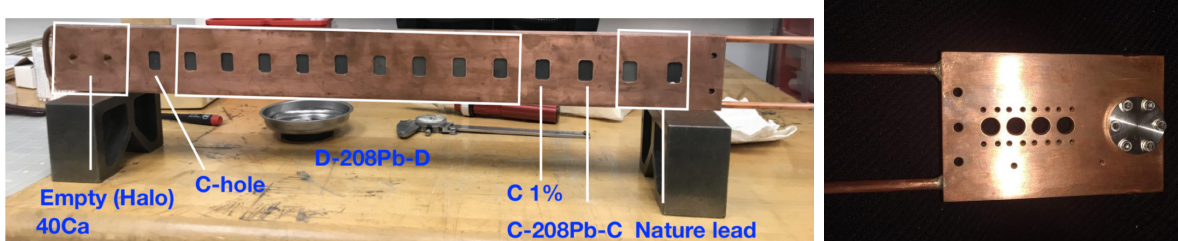


Figure 2.27: Production target ladder and calibration ladder

The  $^{40}\text{Ca}$  and  $^{48}\text{Ca}$  targets were installed on the cold heat sink in dedicated cylindrical sockets at the end of the production ladder. The fact that the  $^{48}\text{Ca}$  and the  $^{208}\text{Pb}$  targets share the same ladder means they actually had the same z location, therefore the same scattering angle (CREX scattering angle was proposed at 4°), to simplify the design, construction and installation of the target chamber.

Special care was needed for  $^{48}\text{Ca}$  target, the pressure should be less than  $10^{-6}$  torr to avoid Ca oxidation. The vacuum of the target chamber was maintained by a turbo-molecular pumping system, which created a  $10^{-7}$  ( $10^{-8}$ ) torr vacuum for the calibration (production) ladder in the target chamber. What's more, gate valves were closed to isolate the target chamber from upstream and downstream beam pipes when beam was not on. By way of precaution, a nitrogen purge system was installed to purge air in case of possible leak. Every time we warmed up the  $^{48}\text{Ca}$  target, boiling was needed before restarting data taking.

### 2.5.1 Target Cooling

The production ladder was cryogenically cooled due to high power from electron beam, while the calibration ladder was water cooled, the calibration runs need only  $\lesssim 1 \mu A$  level beam current. Both ladders were made of cooper, the cooper frame of the production ladder was cooled by  $15 K$ ,  $12 \text{ atm}$  gaseous helium, which runs through the cooling tube surrounding the frame. Contact between the target and the frame and within each layer of the  $^{208}\text{Pb}$  sandwich target is also important. Belleville washers were used to clamp the lead and diamond foils to ensure contact as temperature changes in the beam, besides, a thin layer of Apiezon L vacuum grease was applied to their interface to improve heat conductivity. In the diamond/copper interface, a silver-based paste compound was used for the same purpose. For D-Pb-D sandwich target with thick C foil, the heat loading will be  $100 \text{ W}@70 \mu A$  with a  $4 \times 6 \text{ mm}$  raster, the cooling system would keep the Pb target stay at  $\sim 60 K$  (melting point at  $600 K$ ) assuming good contact and smooth heat conduction. For  $^{48}\text{Ca}$  target, With  $150 \mu A$  beam current, it will produce about  $370 \text{ Watts}$  heat on the target, which raised the target temperature up to  $\sim 300 K$  (melting point at  $1115 K$ ).

### 2.5.2 Raster

Although the target foil was cooled to about  $20 K$  (PREX-II), it still deformed (even melted) under electron's bombardment. Small nonuniformities in the target thickness vary the scattering rate, and over the course of the experiment they eventually generated enough noise to swamp the tiny weak-scattering signal. Actually, this is how we inspect the status of a target and evidence to replace a target if the measured asymmetry width increase significantly.

The solution to this problem is the raster, which is a set of dipole magnets that deflect the beam at about  $25 \text{ kHz}$  to spread the beam on the target. What we learned from PREX-I was that we could significantly reduce the sensitivity to target-thickness variations by synchronizing the helicity flipping frequency with the raster frequency so that it sampled different areas on the target. As shown in Fig. 2.28, the Lissajous pattern we got depends on the frequency difference between X and Y, the larger the frequency difference, the larger the scanning area. The ratio of  $f_y/f_x$  should be an irrational number to prevent a closed Lissajous pattern. The actual frequencies we used were  $25.44$  and  $24.48 \text{ kHz}$ , for PREX-II, the raster size was  $4 \times 6 \text{ mm}$ , and CREX had a raster size of  $2 \times 2 \text{ mm}$ .

Another reason for having raster is heat dissipation, the larger the raster size, the quicker the heat dissipation will be, the lower the target temperature, as shown in Fig. 2.30.

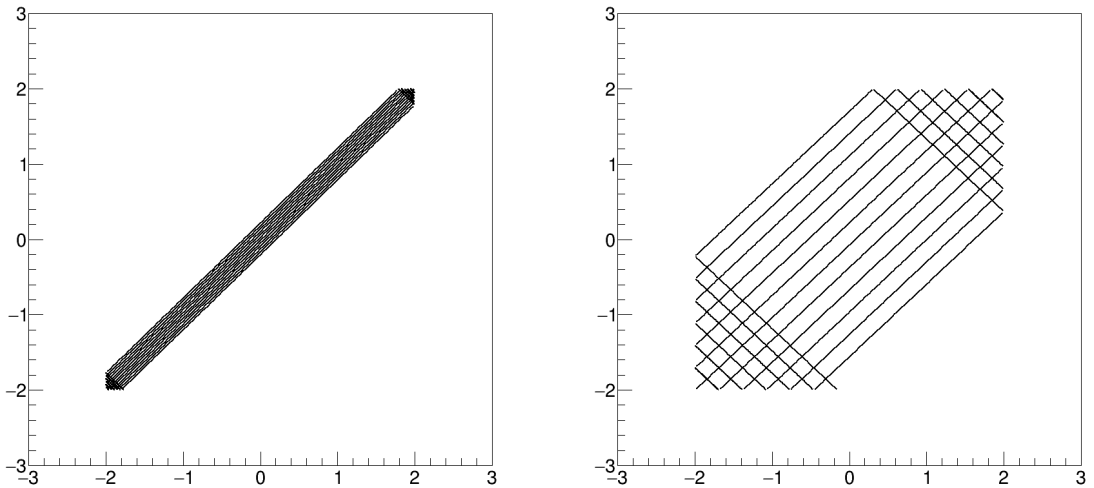


Figure 2.28: Raster pattern with different frequency difference between X and Y. Left:  $|f_y - f_x| = 120 \text{ Hz}$ ; Right:  $|f_y - f_x| = 8 * 120 \text{ Hz}$ . The raster shape is a  $4 \times 4 \text{ mm}$  square.

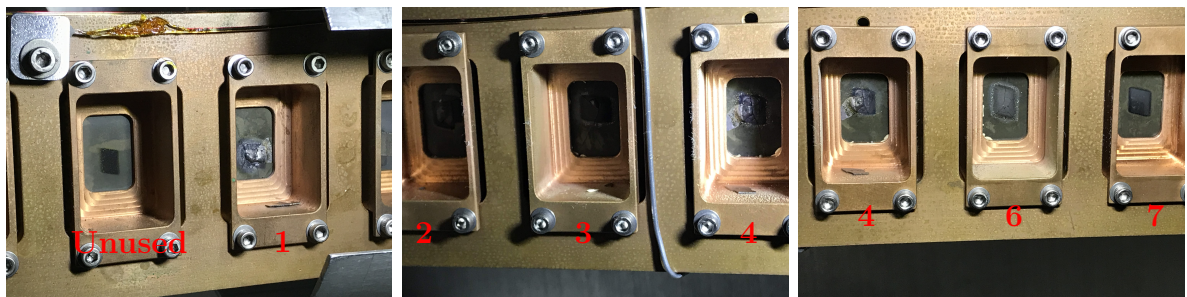


Figure 2.29: Picture of Pb targets after running, one can see clearly the shape of raster.

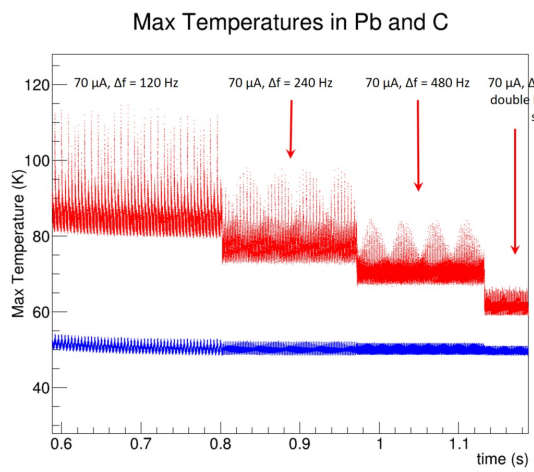


Figure 2.30: How the target temperature change with size of raster area.

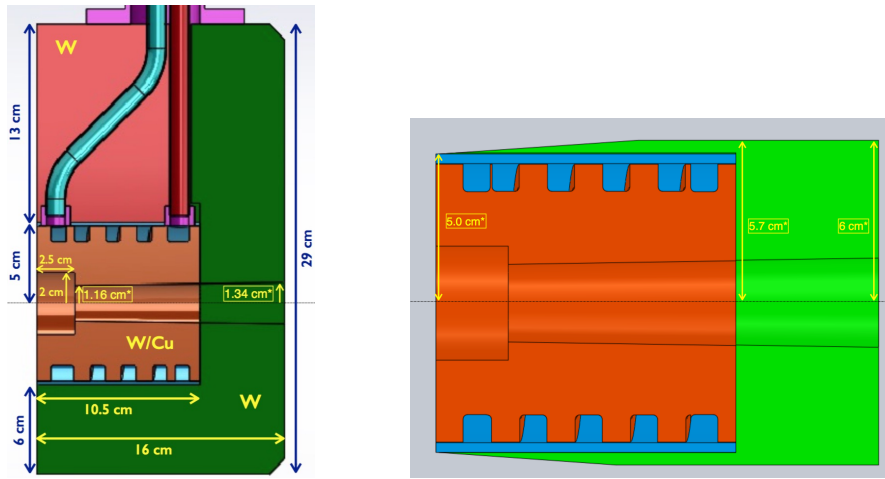


Figure 2.31: Side and top view of beamlime collimator. Beam from left to right.

### 2.5.3 Beamlime Collimator and Sieve Slit Collimators

Another problem that failed PREX-I was the excessive radiation, which damaged electronics in the Hall and the o-ring on the target exit flange leading to leaks and ultimately halted the experiment. With this experience, the new design of the pivot area (the center of the 2 HRS where the target chamber lies in) for PREX-II and CREX payed more attention to radiation near the target region. The idea was to lead as much radiation to beam dump as possible, and absorb the rest radiation in one key component – the beamlime collimator, which was placed 83 cm downstream of the production target. The beamlime collimator consists of an inner collimator and a housing jacket made of sintered tungsten; the inner collimator, in turn, has the same structure of a 70% W/30% Cu alloy collimator and a copper jacket. As shown in Fig. 2.31, there is cylinder notch in the front of the inner collimator, to make sure the electrons/radiation are completely absorbed inside the collimator. The beamlime collimator was water cooled, with maximum heat loading of about 3.65 kW from Pb target. The power on the beamlime collimator was another signal for the degradation of target. When the temperature of the outgoing water increased dramatically, it was time to replace the target. as shown in Fig. 2.32

Besides the beamlime collimator, a few other devices were installed to further eliminate the radiation level in the hall. These devices include the high-density polyethylene (HDPE) neutron shield around the beamlime collimator region and a skyshine shield consisting of a 6 cm thick tungsten block and massive concrete blocks. These extra shields were used to block high energy neutrons from the collimator.

On both sides of the beamlime collimator were the 5 mm thick stainless steel sieve slit collimators (about 1.1 m from the target), which were used for optics study, helping electron trajectory reconstruction. When we took production data, the sieve slit collimators were moved out of the spectrometer acceptance; when we took optics data to measure the scattering angle and  $Q^2$ , the sieve slit collimators were put in to cover the whole spectrometer acceptance, without interfering the inner bore of the the beamlime collimator.

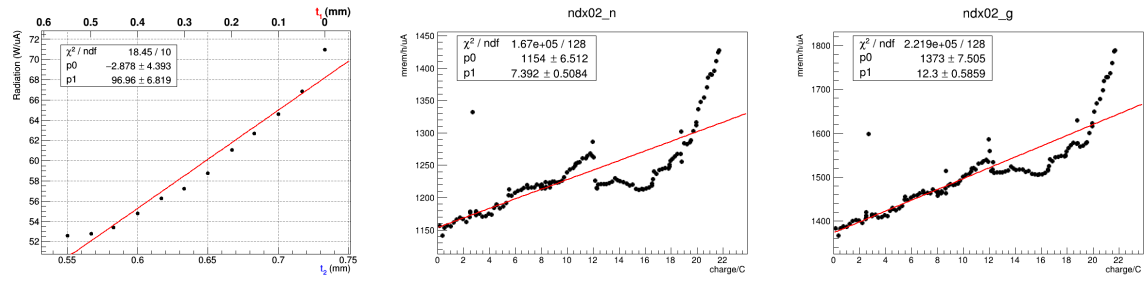


Figure 2.32: Left: a simple model of target degradation – assuming the inner foil ( $t_1$ ) is becoming thinner and the outer foil is becoming thicker ( $t_2$ ) while the total mass keeps intact. The plot shows how the power deposition on the beamline collimator change in this model. Middle and Right: actual neutron and photon radiation level monitored along charge accumulation. They show similar trends.

With known (x, y) information of each hole in the sieve plane, together with the vertical drift chamber (VDC) tracker, we can reconstruct the beam transport matrices.

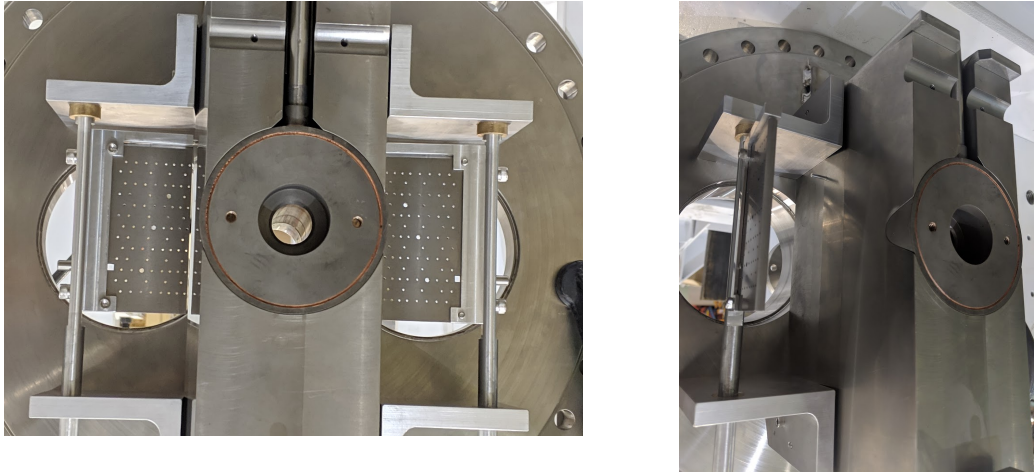


Figure 2.33: Front picture of beamline collimator and sieve slit collimators, looking downstream. One can clearly see a cylinder removed from the central collimator. The sieve planes lie after the beamline collimator and are movable like a door, it can be opened or closed remotely.

## 2.5.4 Septum

The septum magnet is required to bridge the scattered electrons at small angle into the HRS. As said before, the designed scattering angle is about  $5^\circ$  while the smallest angle that HRS can reach is  $12.5^\circ$ , so we need the septum magnet to guide the scattered electrons into HRS.

The septum magnets are normal conducting magnets that consist of 3 coils, by applying large current, it will produce a strong magnetic field (up to  $\sim 1$  T in the central

region). A non-magnetic stainless vacuum box will connect the upstream collimator box and the downstream HRS vacuum pipe on both sides of the septum. The septum beampipe (the one that leads to the beam dump) is made of magnetic stainless steel to shield the magnetic field from the septum, on both ends of the septum beampipe, there are magnetic steel box to shield the fringe magnetic field from septum.

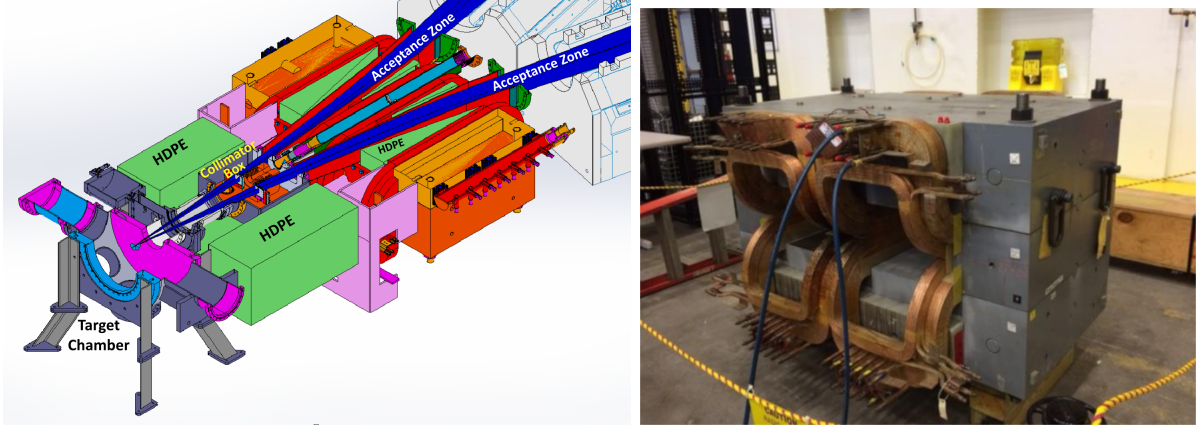


Figure 2.34: Left: septum (the red coils) in the pivot region; Right: picture of septum.

### 2.5.5 High Resolution Spectrometer (HRS)

The key component of every Hall A experiment – spectrometer. The most frequently used ones are the high resolution spectrometer pair. Each HRS consists 3 superconducting quadrupoles and 1 dipole. The maximum magnetic field of the 3 quadrupoles are 1.2, 1.0 and 1.0  $T$  respectively while the dipole can provide up to 1.7  $T$  field. The incoming electrons will be bent 45° up in the vertical plane and then received by the following detectors. HRS has a small angular acceptance ( $\pm 28$   $mr$  horizontally,  $\pm 60$   $mr$  vertically, the solid angle being 7.8  $msr$ ), but can move over a wide range of angle around the hall (12.5° – 165°). As its name implies, it achieves a very high momentum resolution at the  $10^{-4}$  level over a wide range of momentum (0.8 – 4  $GeV$ ). This capacity helped us to reject most of inelastic electrons, because a small difference in electron momentum (2 – 3  $MeV$ ) will lead to large separation in the detector plane, thus leaving us a relative clean data with very small background from inelastic scattering.

Before the entrance of Q1 quadrupoles was the Q1 collimator, which defined the spectrometer acceptance. It was strictly required that the symmetry between left/right, and up/down of Q1 collimators should be preserved to reduce any possible systematic uncertainties.

### 2.5.6 Detector Package

The standard HRS detector package on each arm consists of trigger scintillators for triggering, a pair of VDCs for particle tracking, Cherenkov type detectors and shower

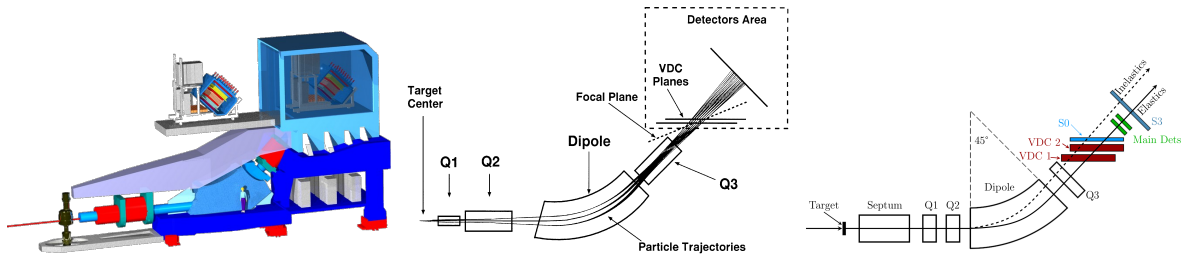


Figure 2.35: Schematic plot of HRS and particle rays inside it. [22] The 'focal plane' in the middle plot, by design, should be at an angle of  $45^\circ$  w.r.t the central ray, but is actually rotated to  $70^\circ$  due to lackness of sextupole winding in Q3. When we talk about the HRS focal plane, we usually refer to the VDC lower plane.



Figure 2.36: Picture of Q1 collimator pairs

counters (calorimeters) for particle identification (PID). In PREX-II and CREX, we needed only part of these detectors, namely VDCs and S0/S3 triggers, others were removed for safety. We built our own Cherenkov counters that can work in the so called 'intergrating mode'.

### Vertical Drift Chamber (VDC)

Each VDC detector package consists of 2 drift chambers, one lower and one upper chamber with a vertical separation of  $0.23\text{ m}$  ( $0.335\text{ m}$  between the same U or V planes of the lower and upper chamber), to enable precise position and angle measurement. The drift chamber is actually a multiwire proportional chamber (MWPC) with 2 layers of sense wires – U and V planes in the lab horizontal plane, which are orthogonal to each other and has a vertical separation of  $26\text{ mm}$ . Each wire plane consists of 368 tungsten wires with the width of adjacent wires being  $4.24\text{ mm}$ , corresponding to  $6\text{ mm}$  in the spectrometer cross section due to the  $45^\circ$  cross angle between the central ray and the VDC plane. The ion's drift time in the chamber are used to reconstruct particle trajectory. The single plane can achieve a position resolution of  $\sim 235\text{ mm}$  FWHM, the angular

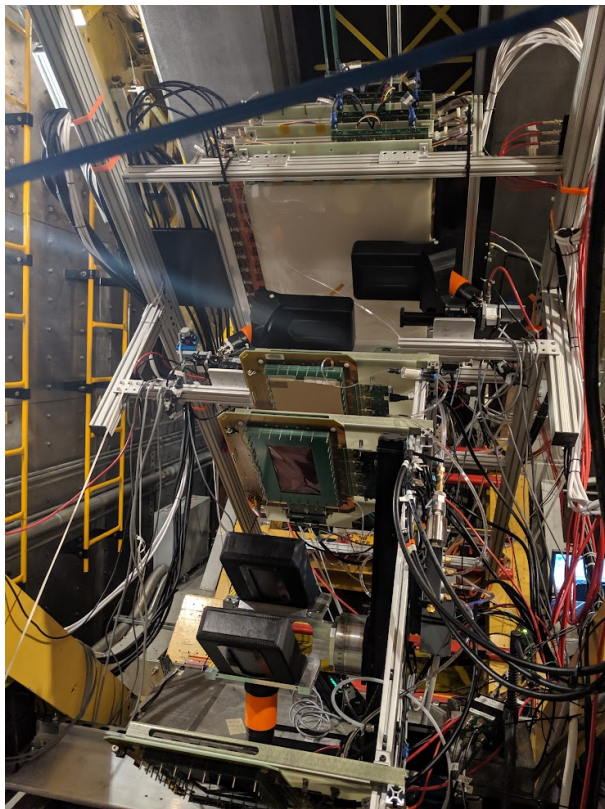


Figure 2.37: The detector package

resolution is  $6 \text{ mrad}$  FWHM for  $\theta$  (out-of-plane angle)  $2.3 \text{ mrad}$  for  $\phi$  (in-plane angle) [23].

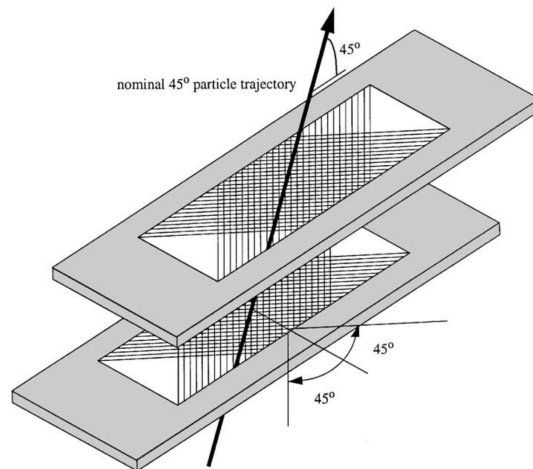


Figure 2.38: Schematic plot of VDCs showing UV wires [23]

VDCs were only used for optics runs in PREX-II and CREX, when we collect electrons one by one to measure their scattering angle and energy, otherwise they were turned off during normal production runs.

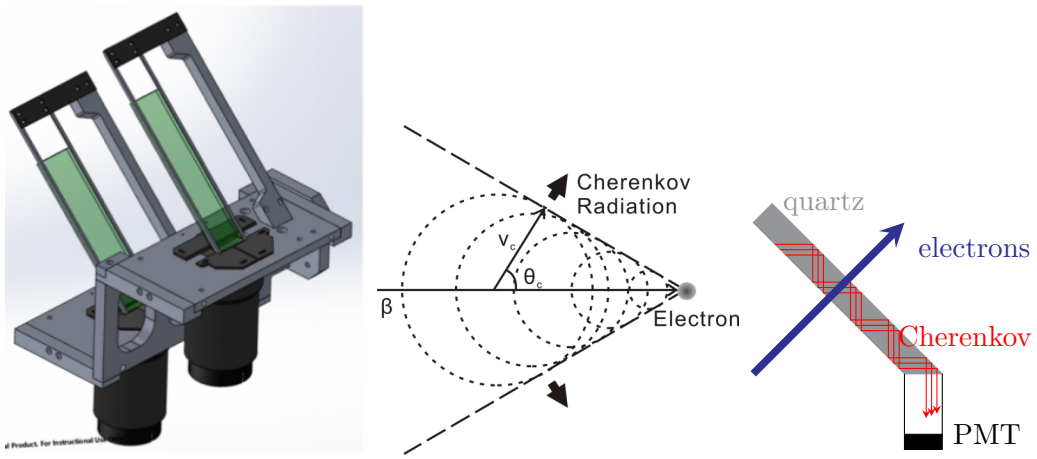


Figure 2.39: Left: CAD drawing of the quartz detector; Middle: schematic plot of Cherenkov radiation, the angle between electron and the Cherenkov radiation is  $\cos \theta = \frac{v_c}{v_e} = \frac{c}{nv_e} = \frac{1}{n\beta} \approx \frac{1}{n}$ ; Right: electron flux goes through a quartz detector.

## Trigger

Same as VDCs, triggers were only used in counting mode for optics study. The standard detector package consists of multiple trigger planes, and we used only 2 of them: S0 and S3 plastic scintillators. The S0 scintillator locates between VDCs and the main detectors while S3 lies behind the main detectors, they have a sensitive area of 170 cm long by 25 cm wide. Their signals were logically combined to provide different trigger rate. The trigger rate was controlled to be less than 50 kHz most of the time (the up limit of VDC is about 250 kHz).

## Main Detector

The main detector of PREX-II and CREX was the 5 mm thick fused silica (quartz) tiles, with a size of 16 cm long by 3.5 cm wide (3 cm  $\times$  3 cm active area). 2 identical quartz detectors were installed with the upstream one used as the main detector and the downstream one as the backup (also used for a cross check in PREX-II). They are tilted to be perpendicular to the electron rays. The high refractive index of quartz ( $n \approx 1.45$ ) means the opening angle  $\theta$  in Fig. 2.39 is about 46°, larger than the critical angle to make total internal reflection ( $\theta_c = \arcsin \frac{1}{n} = 43.6^\circ$ ), therefore, the Cherenkov light produced by high energy electrons will be totally reflected inside the quartz and finally collected by the PMT. The high photon yield make it easier to resolve the electron peak, which was beneficial given the fact that non-linearity of the PMTs is one of the major contributors to systematic uncertainties.

The width of the photon-electron distribution will increase the statistical uncertainty:

$$\sigma_A = \sigma_{stat} \times \sqrt{1 + \left( \frac{\sigma_{PE}}{\langle PE \rangle} \right)^2} \quad (2.24)$$

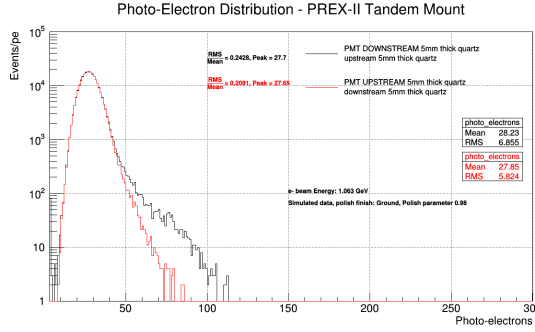


Figure 2.40: Simulation result of photo-electron (PE) spectrum for single electron passing through the main detectors. The wider tail in the downstream detector is due to particle showering in the upstream quartz. Plot from Devi Adhikari.

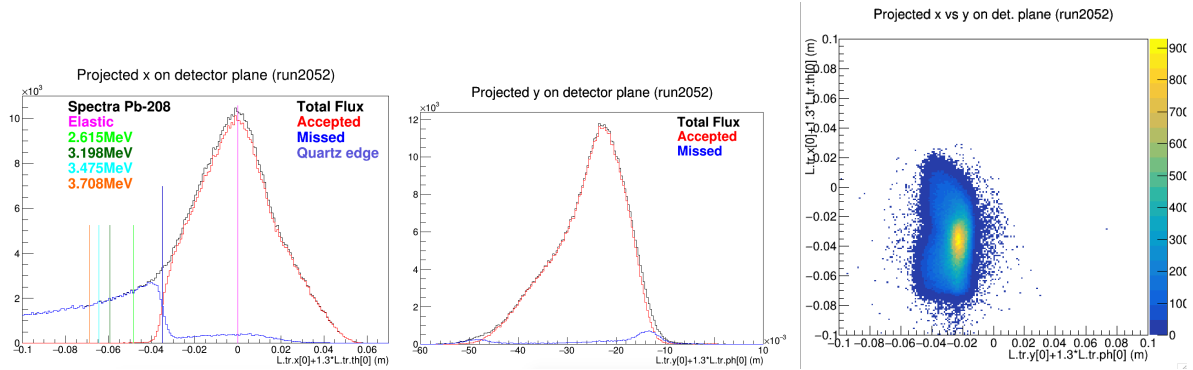


Figure 2.41: Data of x,y distribution on quartz. Plots from Devi Adhikari.

where  $\sigma_{PE}$  is the RMS of the distribution. The RMS can be parameterized into 2 parts: the Gaussian principle part which is inversely proportional to the quartz thickness and a Landou tail which comes from the showering process and is proportional the thickness. The final decision of 5  $mm$  of thickness was a compromise between these 2 parts to minimize detector resolution  $\frac{\sigma_{PE}}{\langle PE \rangle}$ : thicker to increase photon-electron yield and thinner to reduce showering.

There was a homemade motion control system in each arm to move the main detectors remotely, which allowed us to tune the position of the main detectors when we changed gain of the main detectors under a different beam current.

## AT Monitors

About 1  $m$  downstream the main detector were a pair of AT monitors, as shown in Fig. 2.37, which used exactly the same quartz piece as the main detectors. They were used to monitor transverse polarization in the beam.

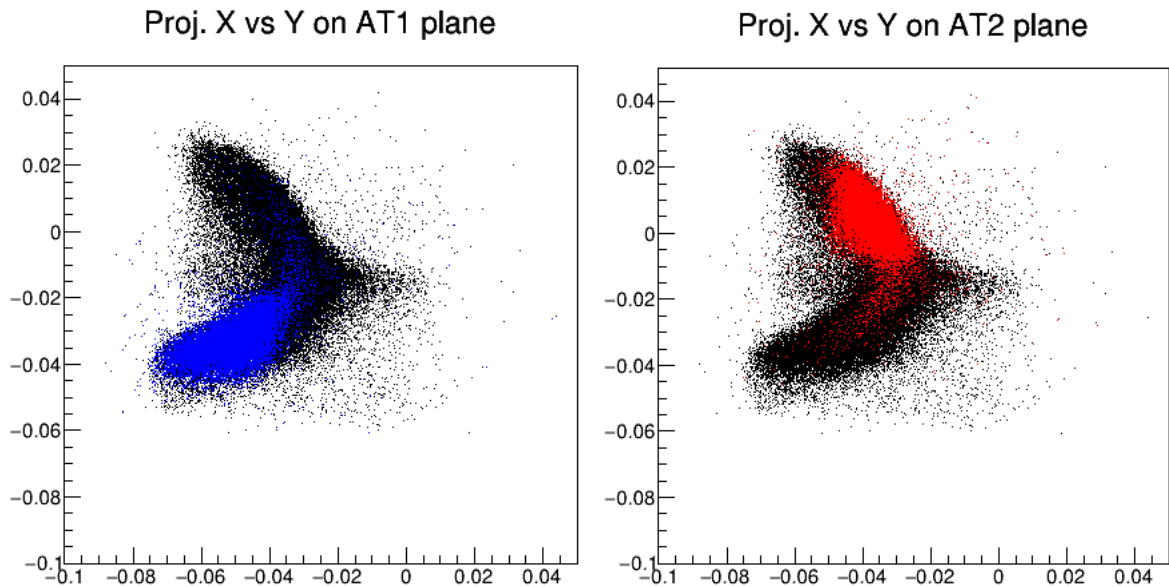


Figure 2.42: Scatter plot of electrons on the AT monitor plane. Red and blue represent events with opposite transverse polarization.

### 2.5.7 Data AcQuisition (DAQ)

CEBAF Online Data Qcquisition (CODA) system We use to pseudo random number generator to decide the helicity pattern, which will trigger the data taking of both detectors and monitors. DAQ will read data from PCs, BPMs, BCMs and detectors, which will then be digitalized by a 18 digits ADC. In one helicity window, they will sample ??? times, which will be grouped into 4 blocks. The sum of the 4 blocks was what we got.

The integrated response of each detector and beam monitor was collected and sampled by a custom 18-bit ADC for each helicity window.

Integrating mode and counting mode

# Chapter 3

## Data Analysis

As mentioned before, though of fast flipping and tremendous effort to keep electron beam in exactly the same conditions (intensity, energy, position and angle on target) through opposite helicity states, life is not easy and there is no way to achieve such a goal, after all, no one can understand completely and control every aspect of something as complicated as an accelerator. There is always various noise caused in various parts of the machine, though very small in general sense, they are large compare to what we want to measure, and actually the largest correction to PV asymmetry. So we need to remove such noise in the raw asymmetry we measured.

We use the same methods to process both PREX-II and CREX data, therefore we will talk about only CREX data here.

CREX started commissioning around December 2019, we took the first good run on Dec 12. 6 slugs (slug 100 - 105) were collected before the Christmas. After the Christmas break, data taking was resumed until Jan 18 2020 when the  $^{48}\text{Ca}$  target was damaged accidentally. It tooks 5 days to prepare a new  $^{48}\text{Ca}$  target. Things moving on quite smoothly, we had 2 days of transverse asymmetry measurement from Feb 10 to Feb 12. We were a little over halfway on data taking when Covid-19 hitted and the lab was shut down at the end of March 2020. Fortunately, things came back 4 months later, we had

variable	quadtets	minirun	run	slug
count	86840789	8527	1386	121
raw asymmetry ( $ppk$ )				
corrected asymmetry ( $ppk$ )				
bpm4aX				
bpm4aY				
bpm4eX				
bpm4eY				
bpm12X				

Table 3.1: CREX Data Set

variable	regression	dithering	Lagrangian
slope correction (ppm)			

the chance to continue data taking for about 1 month. The experiment stopped data taking on Sep 18 2020. A total charge of 480 C was collected, among which 390 C was good charge. The dataset was clearly separated into 3 parts: before AT, after AT (before Covid) and after Covid, which we will talk about later.

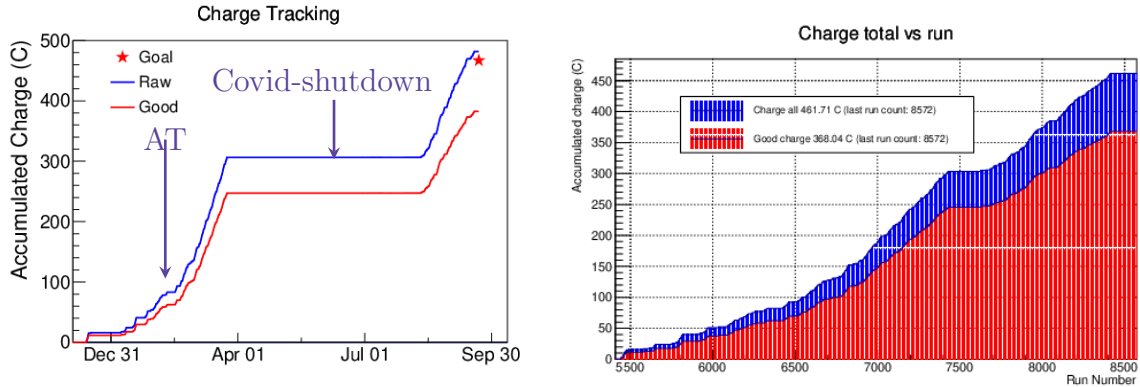


Figure 3.1: Charge accumulation versus time (left) and run number (right). The long plateau on the left plot is due to Covid shutdown, which is shown around run 7500 on the right plot. We see that data taking is most efficient after AT (before Covid), the last month (after Covid) is not bad while the first 2 months is not so efficient due to various problems.

CREX collected 1451 production runs, among them, 1386 were identified as ‘Good’ and used for final analysis. The good runs consists of 1362 both arms runs, 6 left arm runs and 18 right arm runs. Each good production run took about 1 *hour* and collected about 0.3 C charge with a charge efficiency of 80%.

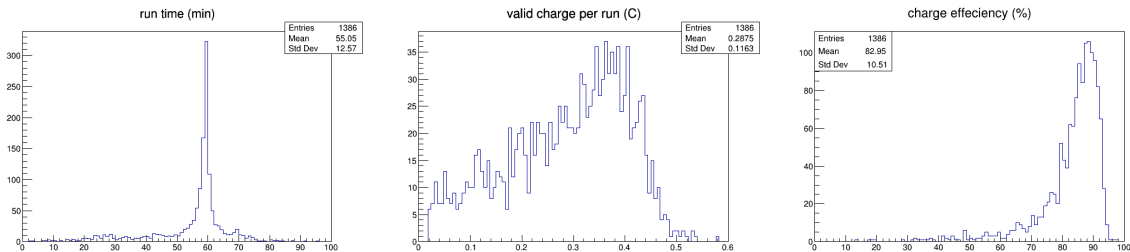


Figure 3.2: Statistics of CREX runs

Though electrons come bunch by bunch, the bunch frequency of 249.5 *MHz* is much larger than our helicity frequency of 120 *Hz*, so electron beam can be regarded as continuous. All electrons within one helicity window will be integrated as 1 record. Every 4

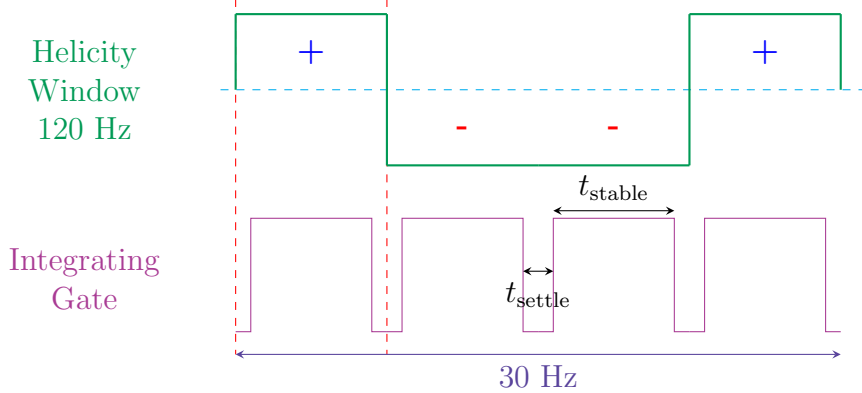


Figure 3.3: For CREX,  $t_{\text{settle}} = 90 \mu\text{s}$ , to allow the PC stabilizes after flipping, avoiding any cross effect from last helicity state. The deputy factor is 98.92%.

continuous helicity window data is grouped as quadruplet in order to cancel the 60 Hz noise in line power, and asymmetry will be calculated based on quadruplet – this is what we called one asymmetry event. So the asymmetry event frequency is 30 Hz. CREX collects ??? such good asymmetry events.

Every run is separated into multiple miniruns to account for the fact beam conditions are changing quickly, it is inappropriate to calculate slope values over a 60 mins run. Minirun will be more proper, the beam conditions, and therefore the slope value should be more stable during such a shorter time period. Every minirun contains 9000 good (pass cut) events (5 mins), the last minirun contains whatever number of good events that can't be divided into 2 miniruns. CREX has 8543 miniruns from 1386 runs, among them, 16 miniruns are discarded due to noisy beam conditions that were not caught in the previous 2 respins. To avoid any respin, these miniruns are simply removed, which counts ??? C.

Runs will be grouped into slugs. One slug is defined as all runs before the next IHWP flipping. With good beam conditions, we could collect 3 slugs per day, so each slug took about 8 hours or longer in case of any accidents. CREX collects 124 slugs, after data clean and combination to remove slugs with only 1 runs, 121 slugs are kept.

Finally, slugs will be grouped into part, with different wien flip status. We have 3 parts as said before.

## Cut

We have only very loose cut on data to keep as much data as possible. The online cuts include a current cut and some stability cuts. The current cut requires the beam current no smaller than  $15 \mu\text{A}$  below the nominal current, due to non-linearity in monitor/detector response. The stability cut says ???

a few miniruns are discarded

## Beam Current

We have 5 bcms and the upstream analog bcm is used as the target current monitor. where are the 5 bcms why choose bcm\_an\_us as bcm\_target?

- non-linearity from electronics read out: false asymmetry. PMT → preamplifier → ADC

Data quality:

- Beam excursion: data quality cuts are applied to remove unstable beam periods  
FIXME: a plot for beam excursion

## 3.1 Raw Data

What we call one event is all electrons counted in one helicity window. The asymmetry value is calculated using every 4 (8 in PREX-II) helicity windows (++ or -++) to cancel the 60 Hz line power noise. The helicity pattern was chosen pseudo-randomly. The CREX data consists of ??? event.

ErrorFlag

beam jitter ??? in position, ??? in energy and ??? in time scale

Every event is accompanied by a set of beam parameter values, recording the beam conditions in that helicity window. A series of cut will be applied, basing on the beam stability, to select good charge.

### Pair value

For any 2 continuous events, define their pair value as: For BPM/BCM, the pair difference is:

$$diff = \frac{v^+ - v^-}{2}$$

For usl/usr, the asymmetry is:

$$asym = \frac{v^+ - v^-}{v^+ + v^-}$$

### Redundant Position Measurement

stripline BPM vs Cavity BPM

#### 3.1.1 Measured Asymmetry

#### 3.1.2 Beam False Asymmetry

Can we count number of electrons from detector read out?

## 3.2 Regression

Regression is the most common statistical method to identify the relationship between dependent variables (Y) and independent variables (X). Bear in mind that regression itself doesn't tell us any relationships or rules, it only works under the assumption that the relationship of variables is predictable (given by the user) and the dependent variables follow a known distribution function  $P(\epsilon)$ , again, needed to be told by the user:

$$Y = f(X) + \epsilon$$

With these prior knowledge, regression is able to calculate the most likely coefficients in the predicted model.

For example, the famous least square fit is actually a linear regression

$$Y = c_0 + \sum c_i x_i + \epsilon$$

assuming Gaussian distribution of the dependent variable:  $\epsilon \sim N(0, \sigma)$  Another frequently used scene is logistic regression for classification, which is very similar to linear regression except  $f(X)$  will be converted into a probability function, e.x. using the logistic function:

$$h(z) = \frac{e^z}{1 + e^z} \quad z = f(X)$$

### 3.2.1 The Model

Considering one monitor and one detector. Assuming the reading noise of detector follows the Gaussian distribution and the monitor is precise:

$$\begin{aligned} M &= m \\ D &= d + \epsilon(0, \sigma_0^D) \end{aligned}$$

Here, M (D) is the measured value while m (d) is the true value and  $\sigma_0^D$  is the variance of the noise for Detector.

Then the difference between beams of opposite polarization will follow also the Gaussian distribution with a larger variance:

$$\begin{aligned} \Delta M &= M^+ - M^- = d^+ - d^- = \Delta d_0 \\ \Delta D &= D^+ - D^- = (d^+ + \epsilon(0, \sigma_0^D)) - (d^- + \epsilon(0, \sigma_0^D)) = \Delta d_0 + \epsilon(0, \sqrt{2}\sigma_0^D) = \Delta d_0 + \epsilon(0, \sigma_1^D) \end{aligned}$$

Again,  $\Delta m_0$  ( $\Delta d_0$ ) is the real difference between the different polarized beams while  $\Delta M$  ( $\Delta D$ ) is the measured value.

The probability for measuring  $\Delta D$  will be:

$$P(\Delta D) = \frac{1}{\sigma_1^D \sqrt{2\pi}} e^{-\frac{1}{2} \left( \frac{\Delta D - \Delta d_0}{\sigma_1^D} \right)^2}$$

We will have a bunch of independent data points:  $(\Delta M, \Delta D)_i$  and we want to extract the relationship between  $\Delta d_0$  and  $\Delta m_0$ :  $c \equiv \frac{\partial d}{\partial m}$  – given the tinyness of  $\delta m$ , first order is precise enough. This is exactly a linear regression problem.

$$\Delta d = 0 + c\Delta m$$

For any real data point  $(\Delta m_0, \Delta d_0)_i$ , the possibility to measure  $(\Delta M, \Delta D)_i$  is:

$$P_i(\Delta D | \Delta M) = \frac{1}{\sigma_1^D \sqrt{2\pi}} e^{-\frac{1}{2} \left( \frac{\Delta D - c\Delta M}{\sigma_1^D} \right)^2} \quad (3.1)$$

For the accumulated data of one minirun, the total probability will be:

$$P = \prod_i^n P_i(\Delta D | \Delta M) = \prod_i^n \frac{1}{\sigma_1^D \sqrt{2\pi}} e^{-\frac{1}{2} \left( \frac{\Delta D_i - c\Delta M_i}{\sigma_1^D} \right)^2} \quad (3.2)$$

To maximize  $P$ , we have:

$$\frac{\partial P}{\partial c} = P \times \sum_i \frac{\Delta M_i}{\sigma_1^D} \left( \frac{\Delta D_i - c\Delta M_i}{\sigma_1^D} \right) = 0 \quad (3.3)$$

Which gives  $c$  as:

$$\sum_i \Delta M_i (\Delta D_i - c\Delta M_i) = 0 \quad \Rightarrow \quad c = \frac{\sum \Delta D_i \Delta M_i}{\sum \Delta M_i^2} \quad (3.4)$$

Extend independent variable to multi-dimensional, we have:

$$\Delta D = (c_1 \ c_2 \ \cdots \ c_n) \begin{pmatrix} \Delta M^1 \\ \Delta M^2 \\ \vdots \\ \Delta M^n \end{pmatrix} + \epsilon(0, \sigma^D) \quad (3.5)$$

$$\frac{\partial P}{\partial c_\nu} \propto \sum_i \Delta M_i^\nu (\Delta D_i - \sum_\mu c_\mu M_i^\mu) = 0 \quad (3.6)$$

Arrange them in a matrix:

$$\begin{pmatrix} \sum_i \Delta D_i \Delta M_i^1 \\ \sum_i \Delta D_i \Delta M_i^2 \\ \vdots \\ \sum_i \Delta D_i \Delta M_i^n \end{pmatrix} = \begin{pmatrix} \sum_i \Delta M_i^1 \Delta M_i^1 & \sum_i \Delta M_i^2 \Delta M_i^1 & \cdots & \sum_i \Delta M_i^n \Delta M_i^1 \\ \sum_i \Delta M_i^1 \Delta M_i^2 & \sum_i \Delta M_i^2 \Delta M_i^2 & \cdots & \sum_i \Delta M_i^n \Delta M_i^2 \\ \vdots & \vdots & \ddots & \vdots \\ \sum_i \Delta M_i^1 \Delta M_i^n & \sum_i \Delta M_i^2 \Delta M_i^n & \cdots & \sum_i \Delta M_i^n \Delta M_i^n \end{pmatrix} \begin{pmatrix} c_1 \\ c_2 \\ \vdots \\ c_n \end{pmatrix} \quad (3.7)$$

Define covariance of any 2 variables as:

$$\text{cov}(x, y) = \sum_i x_i y_i \quad (3.8)$$

To get:

$$\begin{pmatrix} c_1 \\ c_2 \\ \vdots \\ c_n \end{pmatrix} = \begin{pmatrix} \text{cov}(\Delta M^1, \Delta M^1) & \text{cov}(\Delta M^2, \Delta M^1) & \cdots & \text{cov}(\Delta M^n, \Delta M^1) \\ \text{cov}(\Delta M^1, \Delta M^2) & \text{cov}(\Delta M^2, \Delta M^2) & \cdots & \text{cov}(\Delta M^n, \Delta M^2) \\ \vdots & \vdots & \ddots & \vdots \\ \text{cov}(\Delta M^1, \Delta M^n) & \text{cov}(\Delta M^2, \Delta M^n) & \cdots & \text{cov}(\Delta M^n, \Delta M^n) \end{pmatrix}^{-1} \begin{pmatrix} \text{cov}(\Delta D, \Delta M^1) \\ \text{cov}(\Delta D, \Delta M^2) \\ \vdots \\ \text{cov}(\Delta D, \Delta M^n) \end{pmatrix} \quad (3.9)$$

For multiple detectors, it is easy to get:

$$\begin{pmatrix} c_{11} & c_{21} & \cdots & c_{m1} \\ c_{12} & c_{22} & \cdots & c_{m2} \\ \vdots & \vdots & \ddots & \vdots \\ c_{1n} & c_{2n} & \cdots & c_{mn} \end{pmatrix} = \begin{pmatrix} \text{cov}(\Delta M^1, \Delta M^1) & \text{cov}(\Delta M^2, \Delta M^1) & \cdots & \text{cov}(\Delta M^n, \Delta M^1) \\ \text{cov}(\Delta M^1, \Delta M^2) & \text{cov}(\Delta M^2, \Delta M^2) & \cdots & \text{cov}(\Delta M^n, \Delta M^2) \\ \vdots & \vdots & \ddots & \vdots \\ \text{cov}(\Delta M^1, \Delta M^n) & \text{cov}(\Delta M^2, \Delta M^n) & \cdots & \text{cov}(\Delta M^n, \Delta M^n) \end{pmatrix}^{-1} \begin{pmatrix} \text{cov}(\Delta D^1, \Delta D^1) \\ \text{cov}(\Delta D^1, \Delta D^2) \\ \vdots \\ \text{cov}(\Delta D^1, \Delta D^n) \end{pmatrix} \quad (3.10)$$

Theoretically, we need only 5 BPMs to cover all the beam parameter phase space. What's the typical noise of bcm/bpm?

### 3.3 Beam Modulation

### 3.4 Lagragian

### 3.5 Correction

- background dilution

### 3.6 Result

# Chapter 4

## Transverse Asymmetry

The Beam Normal Single Spin Asymmetry (BNSSA, also known as Transverse Single Spin Asymmetry or Transverse Asymmetry) is different from the PV asymmetry, it is purely electromagnetic and therefore parity-conserving. It arises from the interference between one-photon and two-photon exchange (OPE and TPE), therefore it is sensitive to the TPE amplitude. By measuring it, we can probe the strength of TPE, an important knowledge of electron elastic scattering that may explain the myth of proton radius measured with different methods.

The transverse asymmetry is also an important systematic uncertainty to our PV asymmetry measurement, because there is always some residual transverse polarization in the electron beam. With  $\mathcal{A}_n \sim \alpha_{EM} m_e / E_e$ , its magnitude of  $10^{-5}$  for a GeV level electron beam is much larger than  $\mathcal{A}_{pv}$ , so a complete understanding and precise measurement of the transverse asymmetry is needed to ensure accurate correction of  $\mathcal{A}_{pv}$ .

Being a routine and bonus of a PV experiment, PREX-I also measured the transverse asymmetry of some nuclei, namely  $^1H$ ,  $^4He$ ,  $^{12}C$  and  $^{208}Pb$ . Surprisingly, PREX-I saw a zero transverse asymmetry in  $^{208}Pb$ , while the transverse asymmetries of other light nuclei seemed to agree with theoretical predictions, as shown in Fig. ???. One of the reason for PREX-II was that we wanted to verify the zero measurement in  $^{208}Pb$ , which remains as a challenge to theorists.

As its name implies, BNSSA depends on only one spin, either the target or the electron, polarized target is better than polarized target in that it is hard to polarize nuclei, especially heavy nuclei.

### 4.1 Motivation for Transverse Asymmetry

#### The Scattering Theory

Consider the scattering of a free ( $t_0 \rightarrow -\infty$ ) particle from a time independent potential  $V(\mathbf{r})$ , which decays quickly as  $r \rightarrow \infty$ . The evolution from the free initial state  $|i\rangle$  is

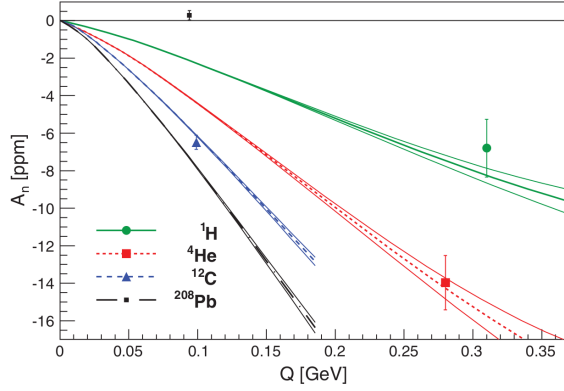


Figure 4.1: Transverse asymmetry measured in PREX-I.

denoted as  $|\psi(t)\rangle_S$  (under the Schrödinger picture,  $\hbar = 1$ ):

$$|\psi(t)\rangle_S = U(t) |\psi(t_0)\rangle = \lim_{t_0 \rightarrow -\infty} U(t, t_0) |i\rangle \quad (4.1)$$

where  $U(t, t_0)$  is the evolution operator:

$$U(t, t_0) = \exp\left(\frac{1}{i}(H_0 + V)(t - t_0)\right) = \exp(-i(H_0 + V)(t - t_0)) \quad (4.2)$$

$H_0$  is the free Hamiltonian and  $H = H_0 + V$  is the complete Hamiltonian with interaction term.

The projection of  $\psi(t)$  to a free final state  $|f\rangle$  defines the so called S-matrix (the order of the subscripts matters):

$$S_{if} \equiv \lim_{t \rightarrow +\infty} \langle f | \psi(t) \rangle = \lim_{t \rightarrow \infty} \lim_{t_0 \rightarrow -\infty} \langle f | U(t, t_0) | i \rangle \quad (4.3)$$

Which defines the S operator:

$$S_{if} = \langle f | S | i \rangle \implies S = U(+\infty, -\infty) \quad (4.4)$$

The S-matrix describe the scattering amplitude from the free initial state  $|i\rangle$  to the free final state  $|f\rangle$ . Conservation of probability indicates unitary of S matrix:

$$S^\dagger S = \sum_f |\langle f | U(+\infty, -\infty) | i \rangle|^2 = 1 \quad (4.5)$$

It is easier to evaluate  $U(t)$  in the interaction picture. Define

$$|\psi(t)\rangle_I \equiv \exp\left(-\frac{1}{i}H_0 t\right) |\psi(t)\rangle_S = \exp(iH_0 t) \exp(-i(H_0 + V)t) |i\rangle \quad (4.6)$$

The subscript I and S denote the interaction and Schrödinger picture respectively. The evolution of  $|\psi(t)\rangle_I$  is:

$$\begin{aligned}
\frac{d}{dt} |\psi(t)\rangle_I &= [\exp(iH_0t)(iH_0) \exp(-i(H_0 + V)t) + \exp(iH_0t)(-i)(H_0 + V) \exp(-i(H_0 + V)t)] |\psi(t)\rangle_I \\
&= -i \exp(iH_0t) V \exp(-i(H_0 + V)t) |\psi(t)\rangle_I \\
&= -i \exp(iH_0t) V \exp(-iH_0t) \cdot \exp(iH_0t) \exp(-i(H_0 + V)t) |\psi(t)\rangle_I \\
&= -i V_I(t) |\psi(t)\rangle_I
\end{aligned} \tag{4.7}$$

where  $V_I(t) = \exp(iH_0t)V \exp(-iH_0t)$  is the time dependent interaction term. Eq. 1.7 leads to the Dyson series:

$$U(t, t_0) = 1 - i \int_{t_0}^t dt_1 V_I(t_1) U(t_1, t_0) = \sum_{n=0}^{\infty} \frac{(-i)^n}{n!} \int_{t_0}^t dt_1 \cdots \int_{t_0}^t dt_n T[V_I(t_1) \cdots V_I(t_n)] \tag{4.8}$$

T means time-ordering:

$$T(V_I(t_1)V_I(t_2)) \equiv \begin{cases} V_I(t_1)V_I(t_2) & t_1 \leq t_2 \\ V_I(t_2)V_I(t_1) & t_2 \leq t_1 \end{cases} \tag{4.9}$$

$$\begin{aligned}
\langle f | U(t, t_0) | i \rangle &= \langle f | i \rangle - i \langle f | \int_{t_0}^t dt_1 V_I(t_1) U(t_1, t_0) | i \rangle \\
&= \delta_{if} - i \sum_m \int_{t_0}^t dt_1 \langle f | \exp(iH_0t_1) V \exp(-iH_0t_1) | m \rangle \langle m | U(t_1, t_0) | i \rangle \\
&= \delta_{if} - i \sum_m \langle f | V | m \rangle \int_{t_0}^t dt_1 \exp(i(E_f - E_m)t_1) \langle m | U(t_1, t_0) | i \rangle
\end{aligned} \tag{4.10}$$

Truncate Eq. 1.10 into first order ( $\langle m | U(t_1, t_0) | i \rangle = \delta_{im}$ ) and define  $T_{if} = \langle f | V | i \rangle$ , we will get:

$$\langle f | U(t, t_0) | i \rangle = \delta_{if} - iT_{if} \int_{t_0}^t dt_1 \exp(i(E_f - E_i)t_1) \tag{4.11}$$

and

$$\begin{aligned}
S_{if} &= \lim_{t \rightarrow +\infty} \lim_{t_0 \rightarrow -\infty} \langle f | U(t, t_0) | i \rangle \\
&= \delta_{if} - iT_{if} \int_{-\infty}^{\infty} dt_1 \exp(i(E_f - E_i)t_1) \\
&= \delta_{if} + i2\pi\delta(E_f - E_i)T_{if}
\end{aligned} \tag{4.12}$$

In matrix form:

$$S = 1 + i2\pi T \tag{4.13}$$

$S$  begin unitary implies

$$S^\dagger S = (1 - i2\pi T^\dagger)(1 + i2\pi T) = 1 + i2\pi(T - T^\dagger) + (2\pi)^2 T^\dagger T = 1 \quad (4.14)$$

which reads

$$T - T^\dagger = i(2\pi)T^\dagger T = i(2\pi)TT^\dagger \quad (4.15)$$

In terms of matrix element:

$$\begin{aligned} \delta(E_f - E_i)(T_{if} - T_{if}^\dagger) &= \sum_m i2\pi\delta(E_f - E_m)\delta(E_m - E_i)T_{fm}T_{mi}^\dagger \\ T_{if} - T_{if}^\dagger &= \sum_m i2\pi\delta(E_m - E_i)T_{fm}T_{mi}^\dagger = ia_{if} \end{aligned} \quad (4.16)$$

where

$$a_{if} = \sum_m (2\pi)\delta(E_m - E_i)T_{fm}T_{mi}^\dagger \quad (4.17)$$

is the absorptive part of the transition amplitude  $T_{if}$ .  $|m\rangle$  extends to all on-shell intermediate states.

The two parts of  $S$  are easy to understand. The constant piece denotes the evolution of one free particle into another free particle without any interactions; obviously, it can evolve only into itself. The  $T$  matirx describe the interaction (transition amplitude) between the free initial particle  $|i\rangle$  and the free final particle  $|j\rangle$ , which tells us the interaction cross section.

The free particle state can be completely described by its momentum (ignoring spin for now)  $\mathbf{p}$ . For an incoming electron  $|\mathbf{p}_i\rangle$ , the probability to transform into the final state of  $|\mathbf{p}_f\rangle$  is:

$$dP = (\text{phase space}) \times (\text{transition probability}) = \frac{d\mathbf{p}_f}{(2\pi)^3} \times |S_{\mathbf{p}_i\mathbf{p}_f}|^2 \quad (4.18)$$

For a non trivial case of  $|f\rangle \neq |i\rangle$ , we have:

$$S_{if} = i2\pi\delta(E_f - E_i)T_{if} \quad (4.19)$$

The differential cross section will be:

$$d\sigma = \frac{dP}{\mathcal{L}\Delta t} \quad (4.20)$$

where  $\mathcal{L}$  is the luminosity, indicating number of particles hitting the target per unit area per unit time, in our case of incoming plane wave,  $\mathcal{L} = \rho v = v$ , and  $\Delta t$  is the interaction time.

$$d\sigma = \frac{1}{v\Delta t} \frac{d\mathbf{p}_f}{(2\pi)^3} 2\pi\delta(E_f - E_i) 2\pi\delta(E_f - E_i)|_{E_f=E_i} |T_{if}|^2 \quad (4.21)$$

Transform one  $\delta$  back to integrating form:

$$2\pi\delta(E_f - E_i)|_{E_f=E_i} = \int_{-\infty}^{+\infty} dt \exp(-i(E_f - E_i)t)|_{E_f=E_i} = \int_{-\infty}^{+\infty} dt \quad (4.22)$$

Physically, we don't go back or into infinity in time, because the real particle is a finite wave packet rather than a plane wave. The integration above should be finite and close to the interaction time

$$\int_{-\infty}^{+\infty} dt \rightarrow \Delta t \quad (4.23)$$

Thus we have a defined cross section

$$d\sigma = \frac{1}{v} \frac{d\mathbf{p}_f}{(2\pi)^3} 2\pi\delta(E_f - E_i)|T_{if}|^2 \quad (4.24)$$

The cross section is proportional to  $|T_{if}|^2$ , as known to us.

## T-Symmetry

Symmetry is the most profound concept and foundation of modern physics, which can be separated into continuous symmetries and discrete ones. Time symmetry is one important discrete symmetry, which states that physical laws should keep unchanged under time reversal operation. Time reversal is the operation that flips time arrow, so that time runs backward after time reversal. Obviously, vectors that are first order of time derivative will also reverse sign, such as momentum, angular momentum and magnetic field.

Express the time reversal operation in QM:

$$|\tilde{\psi}\rangle = \hat{\mathcal{T}}|\psi\rangle \quad (4.25)$$

where  $\hat{\mathcal{T}} : t \rightarrow -t$  is the time reversal operator.

In terms of our scattering, as said above, a particle will flip its momentum and spin (angular momentum) under time reversal, and pick up a phase.

$$|\tilde{\psi}\rangle = \hat{\mathcal{T}}|\psi_{\uparrow}(\mathbf{k})\rangle = \eta|\psi_{\downarrow}(-\mathbf{k})\rangle \quad (4.26)$$

$\eta$  is the phase difference,  $|\eta|^2 = 1$ . So the T matrix can also be applied to time reversed state

$$T_{\tilde{i}\tilde{f}} = \langle \tilde{f} | V | \tilde{i} \rangle \quad (4.27)$$

It is well known that electromagnetic interaction is invariant under time reversal.

$$|T_{if}|^2 = |T_{\tilde{f}\tilde{i}}|^2 \quad (4.28)$$

With these concepts, one can also define the **T-odd** quantities which are proportional to the difference of the magnitude of a normal T element and its half time reversed

version:

$$\begin{aligned}
T\text{-odd} &\propto |T_{if}|^2 - |\tilde{T}_{\tilde{i}\tilde{f}}|^2 \\
&= |T_{if}|^2 - |T_{fi}|^2 \\
&= |T_{if}|^2 - |T_{if}^\dagger|^2 \\
&= |T_{if}|^2 - |T_{if} - ia_{if}|^2 \\
&= -i(T_{if}a_{if}^* - T_{if}^*a_{if}) - |a_{if}|^2 \\
&= 2\text{Im}(T_{if}a_{if}^*) - |a_{if}|^2
\end{aligned} \tag{4.29}$$

### Transverse Asymmetry

Denote the incoming and outgoing transversely polarized electrons as  $|\mathbf{k}\rangle$  and  $|\mathbf{k}'\rangle$ , the scattering is shown in Fig. 1.1.

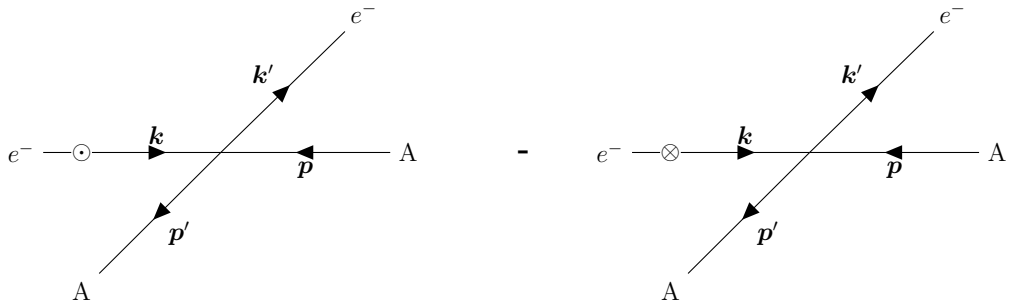


Figure 4.2: Feynman plots of transversely polarized electron scatters off unpolarized nuclear target in the CoM.

The transverse asymmetry will be:

$$\mathcal{A}_n \equiv \frac{N_\uparrow - N_\downarrow}{N_\uparrow + N_\downarrow} = \frac{|T_\uparrow(\mathbf{k}, \mathbf{k}')|^2 - |T_\downarrow(\mathbf{k}, \mathbf{k}')|^2}{|T_\uparrow(\mathbf{k}, \mathbf{k}')|^2 + |T_\downarrow(\mathbf{k}, \mathbf{k}')|^2} \tag{4.30}$$

where  $T(\mathbf{k}, \mathbf{k}') = \langle \mathbf{k}' | V | \mathbf{k} \rangle$  is the scattering amplitude and the arrow subscript indicates electron's spin direction.  $T_\downarrow(\mathbf{k}, \mathbf{k}')$  is related to  $T_\downarrow(-\mathbf{k}, -\mathbf{k}')$  by a rotation around the normal direction of the scattering plane, as shown in Fig. 1.2

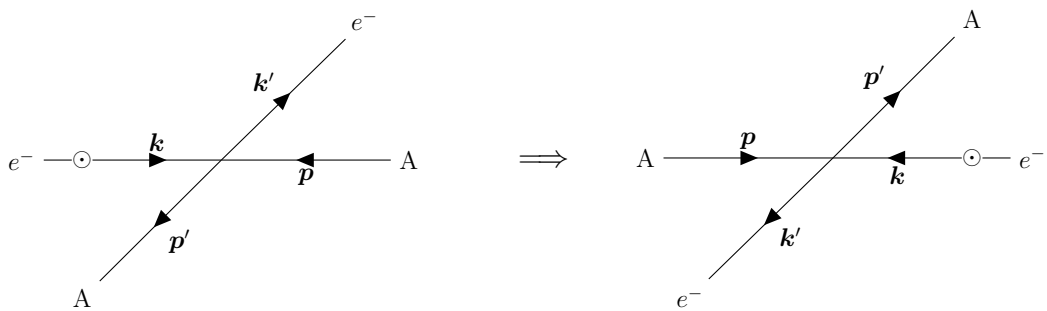


Figure 4.3: Rotation by  $\pi$  around the normal direction.

$$T_{\downarrow}(\mathbf{k}, \mathbf{k}') = e^{i\pi} T_{\downarrow}(-\mathbf{k}, -\mathbf{k}') \quad (4.31)$$

Let  $T_{if} = T_{\uparrow}(\mathbf{k}, \mathbf{k}')$ , then  $T_{\tilde{i}\tilde{f}} = T_{\downarrow}(-\mathbf{k}, -\mathbf{k}')$  and

$$\begin{aligned} \mathcal{A}_n &\approx \frac{|T_{\uparrow}(\mathbf{k}, \mathbf{k}')|^2 - |T_{\downarrow}(-\mathbf{k}, -\mathbf{k}')|^2}{2|T_{\uparrow}(\mathbf{k}, \mathbf{k}')|^2} \\ &= \frac{|T_{if}|^2 - |T_{\tilde{i}\tilde{f}}|^2}{2|T_{if}|^2} \\ &= \frac{2\text{Im}(T_{if}a_{if}^*) - |a_{if}|^2}{2|T_{if}|^2} \end{aligned} \quad (4.32)$$

We see that the transverse asymmetry is a T-odd quantity. For EM interaction

$$T_{if} \propto \alpha \quad a_{if} \propto \alpha^2 \quad (4.33)$$

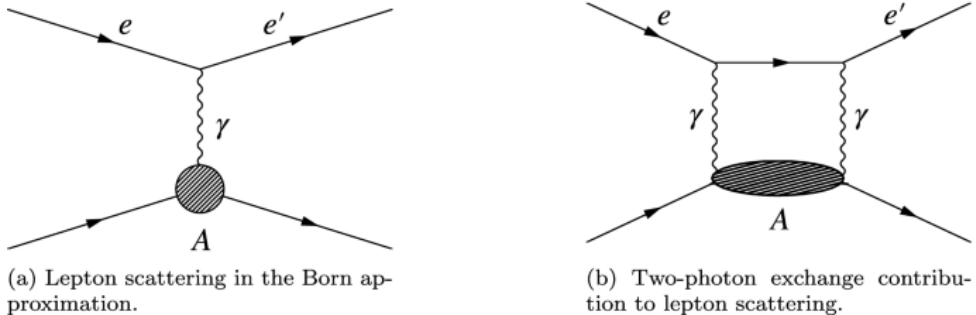
Because  $\alpha \simeq \frac{1}{137}$  is small, we can expand Eq. 1.32 in order of  $\alpha$ . To the lowest order

$$\mathcal{A}_n = 0 \quad (4.34)$$

and to the first order

$$\mathcal{A}_n = \frac{\text{Im}(T_{if}a_{if}^*)}{|T_{if}|^2} \quad (4.35)$$

$T_{ij}$  represents the OPE interaction while  $a_{ij}$  represents the TPE interaction. So the physical interpretation of Eq. 1.34 and 1.35 is that time reversal symmetry requires the transverse asymmetry to be zero under the Born approximation (OPE only) and the (lowest order) non-zero transverse asymmetry comes from the interference between OPE and TPE.



## 4.2 How to Measure the Transverse Asymmetry: the Method

The experimentally measured transverse asymmetry will be

$$\mathcal{A}_{mea} = \mathcal{A}_n \mathbf{p}_e \cdot \hat{n} = \mathcal{A}_n |p_e| \sin(\phi_s - \phi_e) \quad (4.36)$$

where  $\mathbf{p}_e$  is the electron spin direction and  $\phi_s$  being its angle w.r.t. the xz plane;  $\hat{n} = \frac{\mathbf{k}' \times \mathbf{k}}{|\mathbf{k}' \times \mathbf{k}|}$  is the unit normal vector of the scattering plane and  $\phi_e$  the angle between the scattering plane and the xz plane. As shown in Fig. 1.3.. We see an angle dependence of the

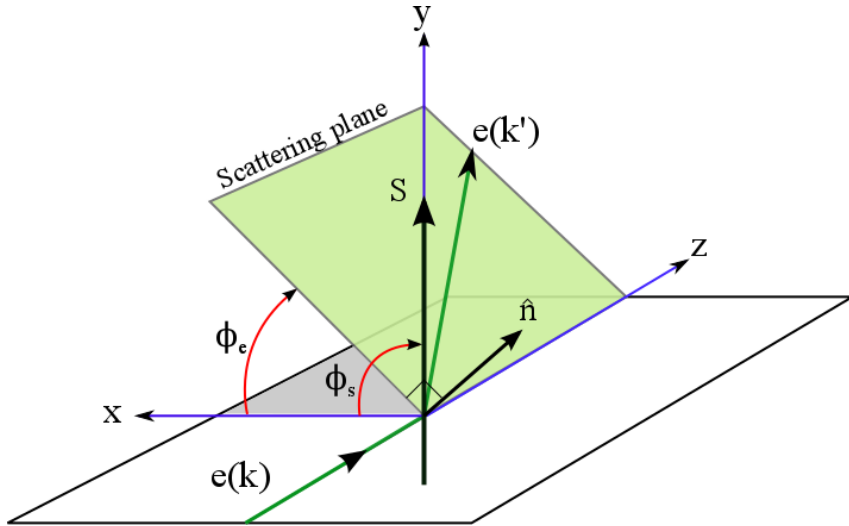


Figure 4.4: Schematic plot of transverse scattering.

measured transverse asymmetry. Experimentally, it is convenient to select the angle  $\phi_s - \phi_e$  being  $90^\circ$ , which usually is the scattering plane that overlaps with the xz plane and the electron spin is perpendicular to the scattering plane, as we did in PREX-II and CREX.

To achieve transverse polarization, we needed a different configuration of the double wien filter. Specifically, we just rotated the longitudinal spin originated from the source to vertically direction using the vertical wien filter, the following rotation we did for longitudinal polarization, as shown in Fig. ??, was omitted. Because the spin is parallel/anti-parallel to the magnetic field in the accelerator arc, there is no spin precession as in the case of longitudinal polarization.

Except the difference in configuration of the double wien filter, everything else was the same as in the case of longitudinal polarization. We spent

## 4.3 The Result

## 4.4 Acceptance Function

As we said before, the spectrometer acceptance was mainly defined by the Q1 collimator, but other devices may also have affects on it. And the accepted area was not tiny ( $0.00377\text{ sr}$ ), not every point within the acceptance had the same detection efficiency and cross section asymmetry, therefore what we measured was actually the average asymmetry over the acceptance:

$$\mathcal{A}_{mea} = \frac{\int d\theta \sin \theta A(\theta) \frac{d\sigma}{d\Omega} \epsilon(\theta)}{\int d\theta \sin \theta \frac{d\sigma}{d\Omega} \epsilon(\theta)} \quad (4.37)$$

Here  $\epsilon(\theta)$  is the acceptance function, which is defined as the ratio of electrons that reach the main detector over all scattered electrons, which depends on the scattering angle  $\theta$ :

$$\epsilon(\theta) = \frac{N_{det}(\theta)}{N_{sca}} \quad (4.38)$$

From Eq. 4.29, we see the importance of the acceptance function. Firstly, it will be a systematic uncertainty of our asymmetry measurement; and secondly, only with the acceptance function, can we compare our experimental measurement to theoretical predictions to interpret our result.

To extract the acceptance function, we had to turn to simulation. Then how did we know our simulation was correct? We will compare the simulation result to optics data, and precise match of various kinematic variables between simulation and data was required.

When we took optics data, we would put in the sieve slit collimators so that we could reconstruct electron trajectory using track info from VDCs to match holes in the sieve plane, therefore we could know the scattering angle and energy for each electron trajectory.

In terms of simulation, we tuned a few parameters to find out the best match: so called the best model, which was then used to calculate the acceptance function. The few parameters we explored were:

- Septum current
- Q1 collimator shift
- Pinch point shift

### 4.4.1 Transportation Matrix

Due to the existence of various magnetic fields (septum, HRS) from target to detector, there is no way to know the exact analytical expression of the transportation from target to detector, though we can approximate and measure it.

The electron's trajectory can be parameterized as:  $\mathbf{X} = (x, \theta, y, \phi, \delta)^T$  w.r.t. to a reference trajectory (usually the central ray). In the transport coordinate,  $\hat{z}$  is the

direction of reference trajectory;  $x$  is the displacement in the dispersive plane relative to the reference trajectory, and  $\theta$  is electron's 'velocity' in the dispersive plane:  $\theta = \frac{\partial x}{\partial z}$ ; similarly,  $y$  and  $\phi$  are displacement and 'velocity' in the y-z plane,  $\hat{y}$  is oriented such that  $\hat{x}, \hat{y}, \hat{z}$  are orthogonal to each other and they form a right-handed coordinate  $\hat{z} = \hat{x} \times \hat{y}$ .  $\delta = \frac{\Delta p}{p}$  represents the fractional deviation of momentum from that of the reference trajectory. With these definitions, we can express one electron's position along the optical path as a Fourier expansion of the initial position of  $\mathbf{X}_0$

$$x_i = \sum_j T_{ij} x_{j,0} + \sum_j \sum_k S_{ijk} x_{j,0} x_{k,0} + \dots \quad (4.39)$$

$T_{ij}$  is what we call the transportation matrix, whose elements indicate the reliance of beam position parameters on each other:  $T_{ij} = \frac{\partial x_i}{\partial x_j}$ . First order is a good approximation of the transportation formula. So that we have:

$$\begin{pmatrix} x \\ y \\ \theta \\ \phi \\ \delta \end{pmatrix} = T \begin{pmatrix} x_{tg} \\ y_{tg} \\ \theta_{tg} \\ \phi_{tg} \\ \delta_{tg} \end{pmatrix} = \begin{pmatrix} x|x_{tg} & x|y_{tg} & x|\theta_{tg} & x|\phi_{tg} & x|\delta_{tg} \\ y|x_{tg} & y|y_{tg} & y|\theta_{tg} & y|\phi_{tg} & y|\delta_{tg} \\ \theta|x_{tg} & \theta|y_{tg} & \theta|\theta_{tg} & \theta|\phi_{tg} & \theta|\delta_{tg} \\ \phi|x_{tg} & \phi|y_{tg} & \phi|\theta_{tg} & \phi|\phi_{tg} & \phi|\delta_{tg} \\ \delta|x_{tg} & \delta|y_{tg} & \delta|\theta_{tg} & \delta|\phi_{tg} & \delta|\delta_{tg} \end{pmatrix} \begin{pmatrix} x_{tg} \\ y_{tg} \\ \theta_{tg} \\ \phi_{tg} \\ \delta_{tg} \end{pmatrix} \quad (4.40)$$

The 'tg' subscript means corresponding values at the target plane. With this matrix, we can propagate backward (inverse of  $T$ ) to calculate electron position at the exit of the target from what we detect using VDCs. Usually we calculate the beam position on the focal plane  $\mathbf{X}_{fp}$ , then the beam position on the target plane will be:

$$\mathbf{X}_{tg} = T^{-1} \mathbf{X}_{fp} \quad (4.41)$$

The reason that we don't use BPM to 'measure' beam position/angle on target is that multiscattering/radiation inside the target foil will distort the beam trajectory.

A typical HRS transportation plot looks like Fig. 4.2:

Actually, we don't need to measure every element of  $T$ , some elements are obviously 0. E.g.  $\delta$  should not be changed by any magnetic field, so  $T_{5i,i \neq 5} = 0$ . The design of HRS tells us that the dispersion depends only on  $\delta$ , but not on  $\theta$  or  $\phi$ , so  $x|\theta = 0$ . Different planes should not interfere with each other, so that  $x|y = x|\phi = \theta|y = \theta|\phi = y|x = y|\theta = \phi|x = \phi|\theta = 0$ . This is a sparse matrix.

The matrix elements were measured using beam trajectory with sieve slit collimator inserted in. When the sieve slit collimator was put in, the electron trajectory from different holes were naturally separated on the focal plane, which allowed us to match them to sieve holes one by one. With a reasonable initial value of the transportation matrix (from previous experiments), we could reconstruct electron's trajectory on the sieve plane using Eq. 4.33. By tuning the matrix element, the one that minimizes the distance of each electron's trajectory on the sieve plane from its corresponding hole center was identified as the transportation matrix, so this is a linear regression problem. The

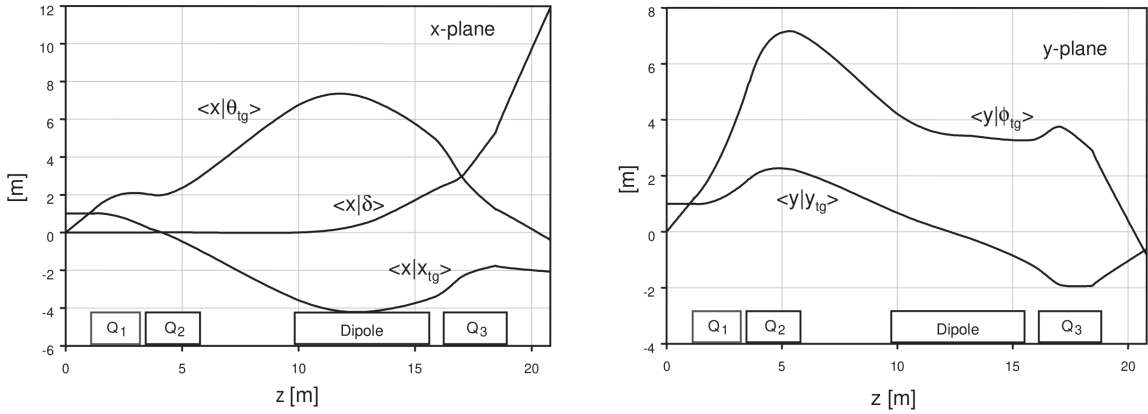


Figure 4.5: Transportation plot of HRS. One can clearly see the dispersion effect due to shift in momentum ( $\delta$ ) in the Dipole area and the convergent effect of Q3.

identification of the septum and HRS current was based on the sieve pattern calculated from the transportation matrix.

#### 4.4.2 Scattering Angle $\theta_{lab}$

The parameter that directly reflects the quality of simulation is the scattering angle, while it was more convenient to use the Target Coordinate System (TCS) than the Hall Coordinate System (HCS) in simulation, we finally were comparing the scattering angle in the lab frame. The 2 coordinate systems and the transportation between them are defined below.

- Hall Coordinate System: originated at the center of the hall and cross the beam line.  $\hat{Z}$  is along the beam line, pointing downstream;  $\hat{y}$  points up and  $\hat{x}$  points left to form a RH coordinate system.
- Target Coordinate System: each HRS specific, the transport coordinate at target position.  $\hat{z}$  is along the beam trajectory, pointing away the target,  $\hat{x}$  in the dispersive plane and points down,  $\hat{y}$  is perpendicular to the dispersive plane and points away (toward) the beamline for L-HRS (R-HRS).

The relationship between HCS and TCS is:

$$\begin{pmatrix} x_{tg} \\ y_{tg} \\ z_{tg} \end{pmatrix} = \begin{pmatrix} \cos(90^\circ) & -\sin(90^\circ) & 0 \\ \sin(90^\circ) & \cos(90^\circ) & 0 \\ 0 & 0 & 1 \end{pmatrix} \begin{pmatrix} \cos(-\theta_0) & 0 & -\sin(-\theta_0) \\ 0 & 1 & 0 \\ \sin(-\theta_0) & 0 & \cos(-\theta_0) \end{pmatrix} \begin{pmatrix} x \\ y \\ z \end{pmatrix} \quad (4.42)$$

$$\left. \begin{array}{l} x_{tg} = -y \\ y_{tg} = x \cos \theta_0 + z \sin \theta_0 \\ z_{tg} = -x \sin \theta_0 + z \cos \theta_0 \end{array} \right\} \iff \left. \begin{array}{l} x = y_{tg} \cos \theta_0 + z_{tg} \sin \theta_0 \\ y = -x_{tg} \\ z = -y_{tg} \sin \theta_0 + z_{tg} \cos \theta_0 \end{array} \right\} \quad (4.43)$$

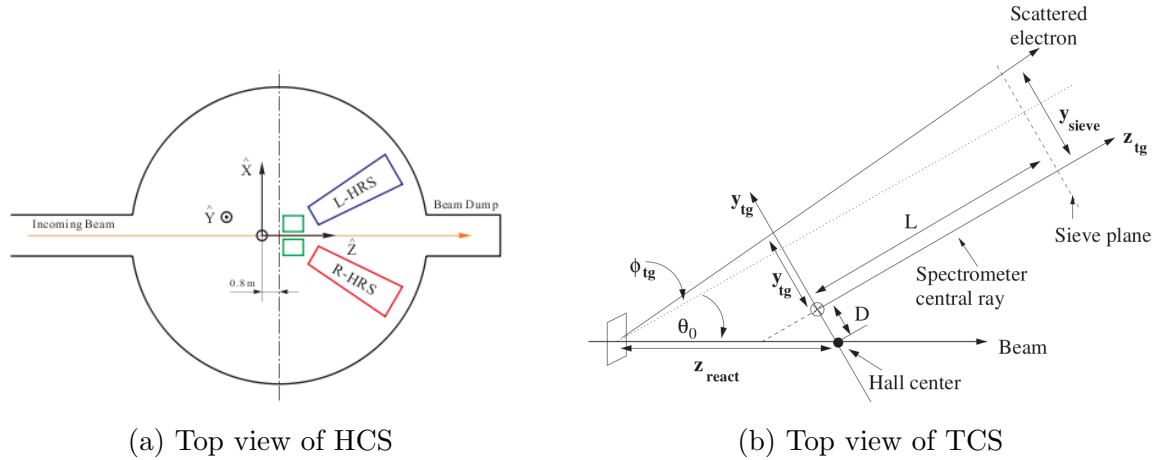


Figure 4.6: Schematic plot of HCS and TCS. The Hall center is the origin of the HCS, but the target doesn't necessary lie in the Hall center. The distance from the Hall center to the sieve plane L is constant, which is used to identify the origin of the TCS. In ideal case, the origins of both coordinate systems will overlap.

Define  $R = (x^2 + y^2 + z^2)^{1/2} = z_{tg} (\phi_{tg}^2 + \theta_{tg}^2 + 1)^{1/2}$ . So the scattering angle in the lab frame will be:

$$\cos \theta = \frac{z}{R} = \frac{-\phi_{tg} \sin \theta_0 + \cos \theta_0}{(\phi_{tg}^2 + \theta_{tg}^2 + 1)^{1/2}} \quad (4.44)$$

For data,  $\theta_0$  was identified to be  $4.789^\circ$  ( $4.771^\circ$ ) for L-HRS (R-HRS). In simulation, both arms used  $4.74^\circ$ . Note that  $\theta_{lab}$  is a post-target (apparent) quantity, which includes effect of post-vertex radiation and multi-scattering, not the 'real' scattering angle (vertex quantity) at the vertex where the interesting PV elastic scattering happens. The correction from the apparent distribution to the vertex distribution is about 1.5%.

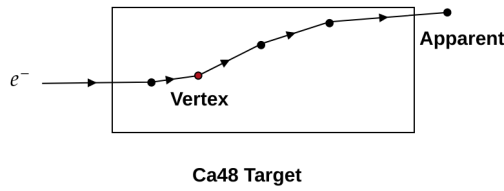


Figure 4.7: Schematic plot of vertex and apparent quantities.

#### 4.4.3 Data

To determine the new tune of septum and HRS settings for CREX, we started with PREX-II tune, scaled it to CREX momentum. To know the appropriate septum current that will bridge the central ray into HRS axis we tuned septum and Q1 current in 2

Exp	Arm	Dipole p0 (GeV)	Septum (A)	Q1 (A)	A2 (A)	Q3 (A)
PREX-II	Left	0.95285	333	118.50	407.70	450.76
	Right	0.95284	333	118.55	404.07	446.90
CREX	Left	2.183522	801	225.387	934.273	981.301
	Right	2.183499	801	230.916	925.955	981.301

Table 4.1: PREX-II and CREX tune

steps: coarse and fine tuning. During coarse tuning, we changed septum and Q1 current by a large step: 10% (**central ray search**); and then fine tuned the septum current in a smaller step: 2.5% to find out the largest acceptance (**inner edge search**).

During the central ray search, if the septum current was inappropriate, then when we changed the Q1 current, the central hole in reconstructed sieve pattern plot would shift, as shown in Fig. 4.5.

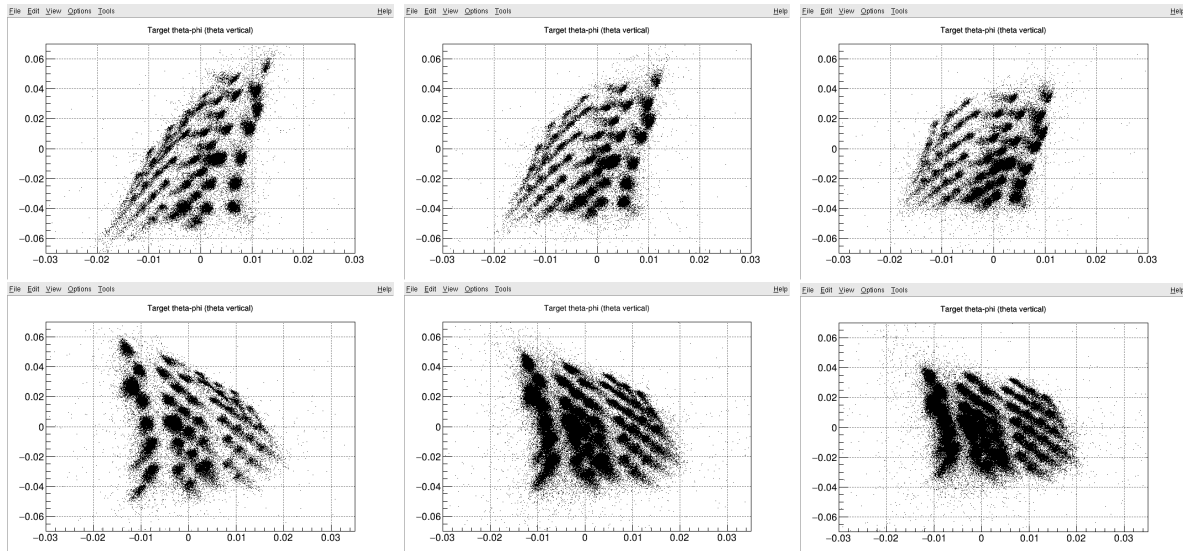


Figure 4.8: Sieve pattern plots for -10% septum current and varied Q1 current, from left to right: -10%, nominal and +10% Q1 current. With different Q1 current, the sieve pattern twist, and the central hole shifts in  $\theta$ , so the septum current is not a good value.

Fig. 4.6 told us the nominal septum current and HRS settings was not a bad choice, so we could move on to inner edge search with this septum nominal value: to see more inner holes – holes with largest (smallest) phi in Left (right) arm. It turned out a 5% increase from the nominal value gave us the largest acceptance, which corresponds to a septum current of:  $1.05 \times (333 * 2.183522 / 0.95285) = 801.25 \text{ A}$ .

With selected septum current, we continued to minimize beam spot size on the detector plane, a fine tune of Q1 and Q3 gave us the smallest detector spot size with Q1 -17% (-15%) from the nominal value on left (right) arm, and Q3 -5% from the nominal value on both arms, which led to the final CREX tune as shown in Table 4.1.

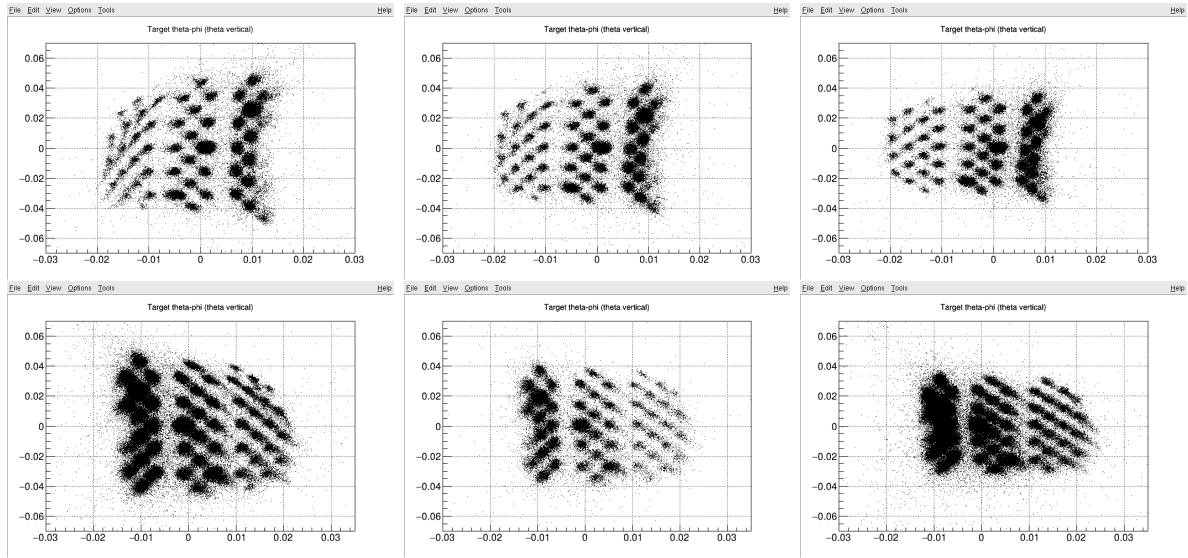


Figure 4.9: Sieve pattern plots for nominal (scaled from PREX-II setting) septum current and varied Q1 current, from left to right: -10%, nominal and +10% Q1 current. Top row is right arm and bottom row is left arm. With different Q1 current, the sieve pattern twist, but the central hole keeps at the same position, which means the central ray goes through the axis of the HRS.

#### 4.4.4 Simulation

The simulation was not exactly the reproduction of reality. We used GEANT4 to simulate the geometry of each component based on the designed values, the septum magnetic field was scaled from a field map file sampled from the septum at  $j_0 = -1320 \text{ A/cm}^2$ :

$$B'_{xyz} = \frac{J}{J_0} \times \frac{P}{P_0} \times B_{xyz} \quad (4.45)$$

The same for HRS field:

$$B'_{i=Q1,Q2,D,Q3} = \frac{P}{P_0} \times B_i \quad (4.46)$$

Using this construction, we could firstly vary the septum current to choose the one that most matched the data, then scaned through collimator shift and pinch point shift to select the best model.

Somewhat expected, a coarse scan through the septum told us the septum range for best model: around 0-5% above the nominal value.

Then we can scan throught the pinch point and collimator shift with a fine tune of the septum current (from -1% to +5%). The pinch point is the connection point between the septum beampipe and the collimator box, whose misalignment will affect the acceptance; another parameter we can tune is the collimator (TCS) y position, which of course has a large impact on the acceptance. For each simulation, we will compare the average scattering angle  $\theta_{lab}$ ,  $Q^2$  and asymmetry to that of optics data.

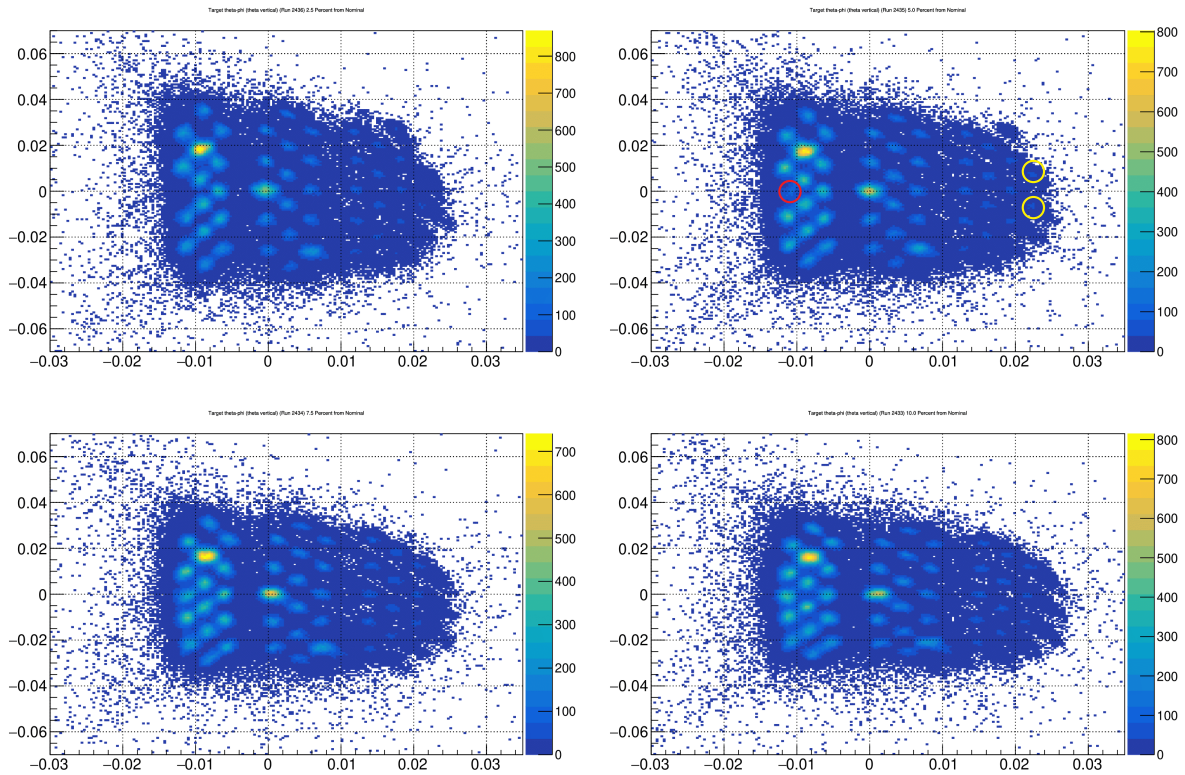


Figure 4.10: Inner edge search on the left arm. Septum current from top left to bottom right: +2.5%, +5%, +7.5%, +10%. The inner middle hole starts to appear since +5%, and outer holes disappear since 7.5%, so the best septum current was chosen to be +5%

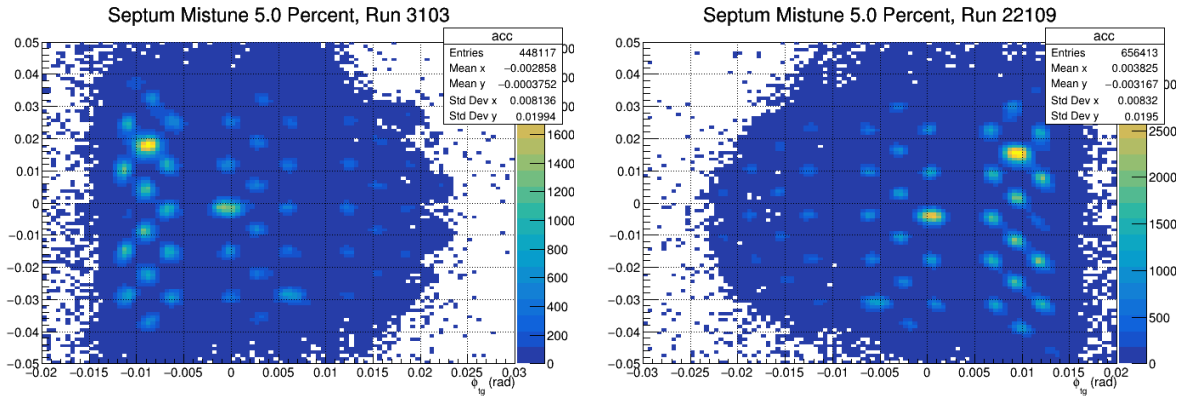


Figure 4.11: Sieve plot of CREX tune. Centered at  $(-0.3, -1.5)$ , the new beam position for the new target.

As shown in Fig. 4.11, when we shift the pinch point toward the beam pipe (from negative values to positive values for left arm, opposite for right arm), the acceptance increases until the nominal value, and then saturates. Similar trend was seen for shift of Q1 collimator.

		Left			Right		
Q1(%)	Q3 (%)	run	$\sigma_y$ (cm)	$\sigma_x$ (cm)	run	$\sigma_y$ (cm)	$\sigma_x$ (cm)
0	0	2524	0.9604	1.634	21604	0.009564	0.01503
-5	0	2525	0.955	1.188		Left arm only	
-10	0	2526	1.005	0.9063		Left arm only	
-15	0	2527	0.1078	0.7314		Left arm only	
-20	0	2528	1.182	0.6801		Left arm only	
-11	0	2529	1.012	0.8767	21609	0.009315	0.007337
-12	0	2530	1.012	0.8349	21610	0.009429	0.006957
-13	0	2531	1.033	0.7835	21611	0.009526	0.006682
-14	0	2532	1.057	0.7515	21612	0.009623	0.06367
-13	+10	2533	1.754	1.929	21613	0.0162	0.0215
-13	+5	2534	1.374	0.7282	21614	0.01276	0.01174
-13	-5	2535	0.8357	0.9751	21615	0.008422	0.008514
-13	-10	2536	0.8855	1.482	21616	0.008891	0.01387
-13	-2	2538	0.9415	0.8761	21618	0.9117	0.7078
-13	-4	2539	0.8602	0.9181	21619	0.8493	0.7912
-13	-7	2540	0.8182	1.154	21620	0.8304	1.027
-13	-9	2541	0.8445	1.389	21621	0.8545	1.268
-15	-5	2542	0.8354	0.8869	21622	0.827	0.7563
-15 (R);-17 (L)	-5	2543	0.8409	0.8315	21623	0.8382	0.7615

Table 4.2: Beam spot size with different HRS settings.

Various correction was applied to the simulation values. That includes the position difference between the production target and the calibration target, which was 20 mm downstream the production  $^{48}\text{Ca}$  target; and the correction caused by the database, which was optimized on one beam position ( $x_0, y_0$ ):

$$\phi_a = \phi_r + 0.5 \text{ mrad/mm} \times (x - x_0) + 0.5 \text{ mrad/mm} \times (y - y_0) \quad (4.47)$$

( $x, y$ ) is the actual beam position.  $\phi_a$  and  $\phi_r$  are actual and reconstructed  $\phi_{tg}$ . An extra acceptance was added to the right arm to get a better match.

From the ratio plot, we selected the best model which had the smallest difference between simulation and data in  $\theta_{lab}$  and  $Q^2$ :

	septum	col shift (mm)	pinch point shift (mm)
LHRS	+2%	-1	0
RHRS	+5%	2	0

We can check the  $\theta_{lab}$  for the best models

Using this best models, we can calculate the acceptance function as Eq. 4.30:

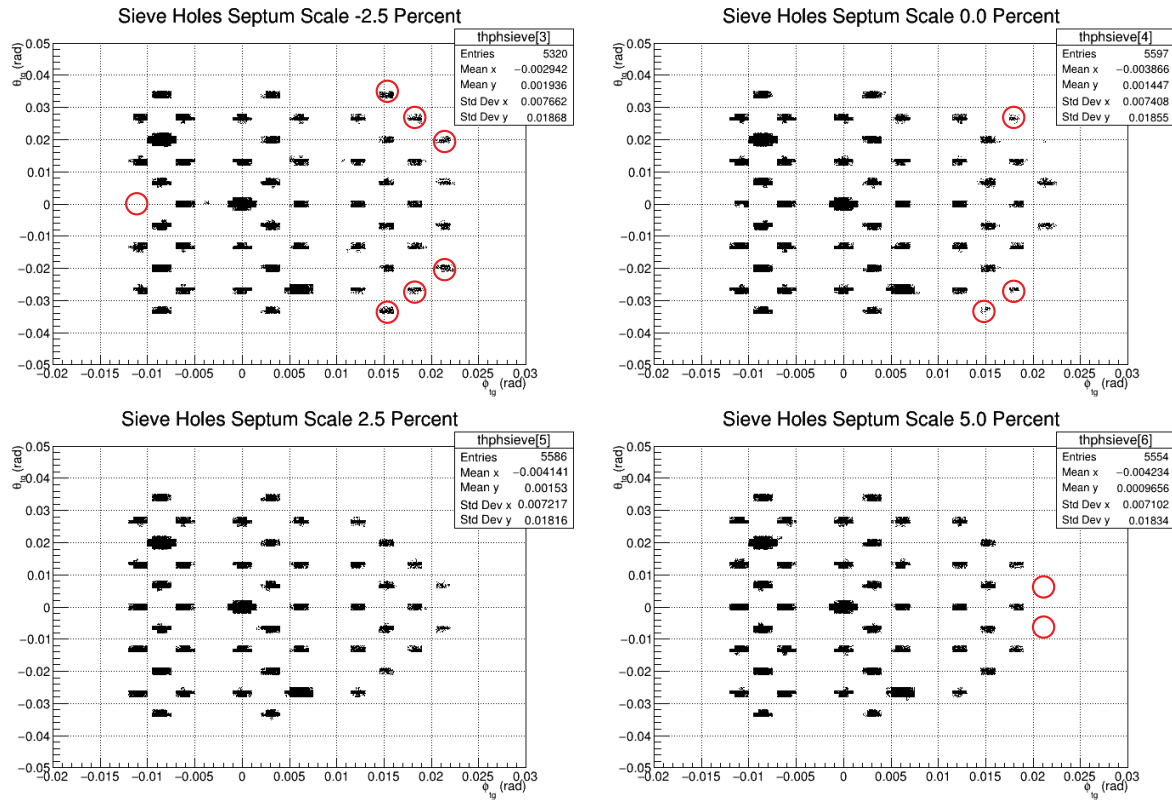


Figure 4.12: Sieve pattern plots from simulation with different septum current.

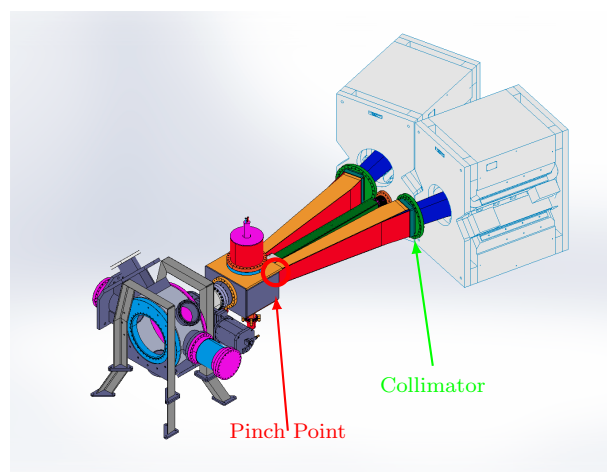


Figure 4.13: Position of the pinch point and the Q1 collimator.

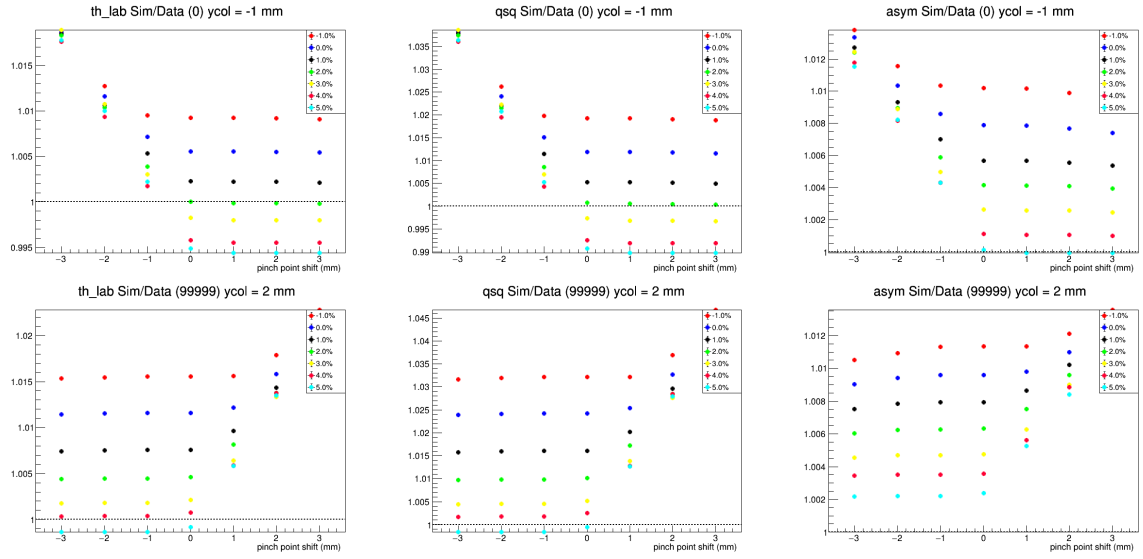
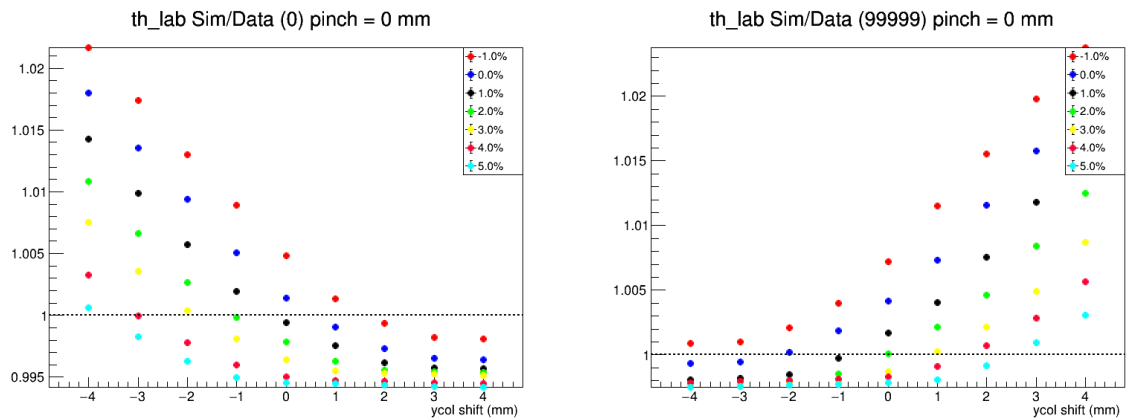


Figure 4.14: Ratio of simulation to data average value for  $\theta_{lab}$ ,  $Q^2$  and  $\mathcal{A}$ . Top (bottom) row for left (right) arm.



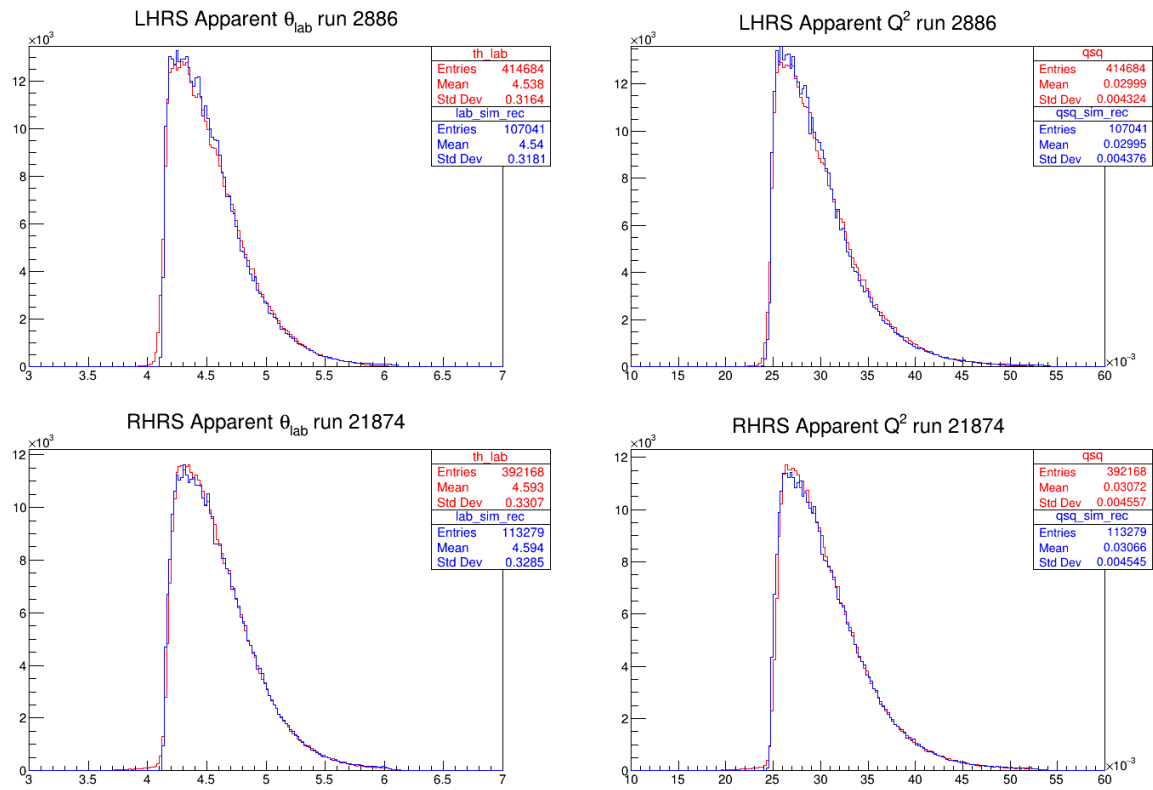


Figure 4.15:  $\theta_{lab}$  and  $Q^2$  comparison between best models and data (apparent values).

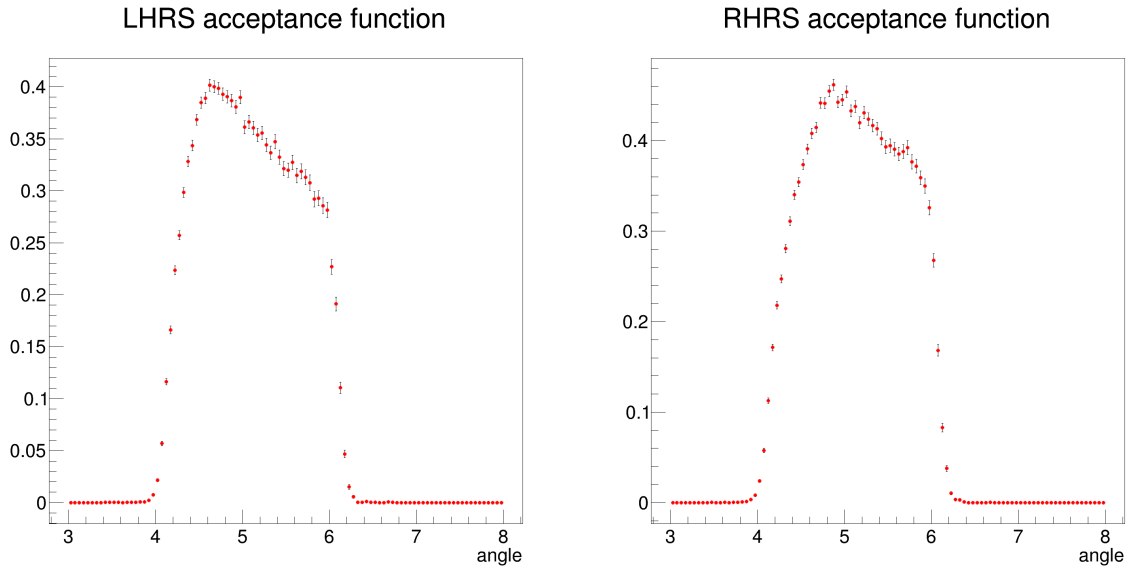


Figure 4.16: Acceptance function extracted using the best models.

# Chapter 5

## Results

### 5.1 Polarization

#### 5.1.1 Moller

#### 5.1.2 Compton

### 5.2 Final Number

### 5.3 Physical Implication

#### 5.3.1 Theoretical Models

Neither the nuclear interaction nor their wave functions are known to us. Unlike particle physics, there is no such a single Standard Model to describe general properties of a nuclear system, such as the ground state binding energy, nuclear size and excitation spectrum. Various models work well in their own territories. Ab-initio is mainly used to describe light nuclei while Density Functional Theory (DFT) provides very precise prediction for heavy nuclei.

#### ab-initio

Ab-initio is more like a theoretical approach, that needs to calculate the force between nucleons and then solve the quantum many-body equation from them. While DFT is more like an experimental approach, which uses experimental data to fit interactions in a given region of the nuclear landscape.

- Green's function Monte Carlo (GFMC)
- No-Core Shell Model (NCSM)
- Coupled-cluster

## Nuclear Density Functional Theory (DFT)

The basic idea is to construct a general functional, with nucleons density distribution as input, will output the ground-state energy and other properties of the nuclear system, the difficulty lies in that no single general functional can cover all nuclei. The basic idea is simple, once we know the density distribution function, then one can calculate the total energy of the system based on this distribution function, minimization of the total energy will be the ground state, and other static properties will be inferred from the ground state. Excitation properties can also be calculated from DFT. The only problem is how to know the density distribution function.

## Effective Field Theory (EFT)

Based on nucleons and pions, but still obey the symmetry of QCD. Various EFT models are based on an effective interacting Lagrangian, for example, FSUGold model has the following effective Lagrangian [27]:

$$\begin{aligned} \mathcal{L}_{\text{int}} = & \bar{\psi} \left[ g_s \phi - \left( g_v V_\mu + \frac{g_\rho}{2} \boldsymbol{\tau} \cdot \mathbf{b}_\mu + \frac{e}{2} (1 + \tau_3) A_\mu \right) \gamma^\mu \right] \psi \\ & - \frac{\kappa}{3!} (g_s \phi)^3 - \frac{\lambda}{4!} (g_s \phi)^4 + \frac{\zeta}{4!} (g_v^2 V_\mu V^\mu)^2 \\ & + \Lambda_v (g_\rho^2 \mathbf{b}_\mu \mathbf{b}^\mu) (g_v^2 V_\mu V^\mu) \end{aligned} \quad (5.1)$$

This Lagrangian density describes interactions of the nucleon field  $\psi$  to various meson fields and their self-interactions.  $\phi$  is a scalar.

The difference between different EFT models is just how many coupling they include in their effective Lagrangian density. With the Lagrangian density, one can calculate the properties of various nuclei, fitting predicted values to experimental results to get a parameter set for the coupling constant in the Lagrangian, which is called one model. Frequently used EFT models include NL3 [], FSUGold [] and

## Saturation

The invariance of binding energy per nucleon ( $E_b/A$ ) w.r.t.  $A$  means that the interaction between nucleons is not proportional to  $A(A-1)$ , but proportional to  $A$ , which means nucleons saturate.

### 5.3.2 Saturation Density

Nuclear Density Function Theory the basic idea is given a Lagrangian density function:

## Atomic Parity Violation Measurement

Accuracy of atomic PV measurement is about 0.3% (FIXME), which is important for the test of the SM and the search for physics beyond the SM. A higher (0.1%) precision

requires knowledge about the neutron radius better than 1%. [40]

## 5.4 Neutron Stars

Pb neutron radius is large  $\Rightarrow$  stiff EOS at low nuclear density (subnuclear density) combine NS radius measurement NS radius is small  $\Rightarrow$  soft EOS at high density these 2 measurements will mean softening of EOS with density  $\Rightarrow$  transition to an exotic high density phase such as quark matter, strange matter, color superconductor, kaon condensate

### URCA Cooling

proton fraction for matter in beat equilibrium depends on symmetry energy  $S(n)$ .o The larger  $R_n$  in Pb, the lower the threshold mass for direct URCA cooling. If  $R_n - R_p < 0.2 \text{ fm}$  all EOS models don't have direct URCA in  $1.4 M_{\text{sun}}$  stars If  $R_n - R_p > 0.25 \text{ fm}$ , all models do have URCA in  $1.4 M_{\text{sun}}$  stars

# Bibliography

- [1] J. B. Bellicard, P. Bounin, R. F. Frosch, R. Hofstadter, J. S. McCarthy, F. J. Uhrhane, M. R. Yearian, B. C. Clark, R. Herman, and D. G. Ravenhall. Scattering of 750-mev electrons by calcium isotopes. *Phys. Rev. Lett.*, 19:527–529, Aug 1967. doi: 10.1103/PhysRevLett.19.527. URL <https://link.aps.org/doi/10.1103/PhysRevLett.19.527>.
- [2] C. J. Horowitz. Parity violating elastic electron scattering and coulomb distortions. *Phys. Rev. C*, 57:3430–3436, Jun 1998. doi: 10.1103/PhysRevC.57.3430. URL <https://link.aps.org/doi/10.1103/PhysRevC.57.3430>.
- [3] C.Y. Prescott, W.B. Atwood, R.L.A. Cottrell, H. DeStaebler, Edward L. Garwin, A. Gonidec, R.H. Miller, L.S. Rochester, T. Sato, D.J. Sherden, C.K. Sinclair, S. Stein, R.E. Taylor, J.E. Clendenin, V.W. Hughes, N. Sasao, K.P. Schüler, M.G. Borghini, K. Lübelsmeyer, and W. Jentschke. Parity non-conservation in inelastic electron scattering. *Physics Letters B*, 77(3):347–352, 1978. ISSN 0370-2693. doi: [https://doi.org/10.1016/0370-2693\(78\)90722-0](https://doi.org/10.1016/0370-2693(78)90722-0). URL <https://www.sciencedirect.com/science/article/pii/0370269378907220>.
- [4] P. A. Souder, R. Holmes, D.-H. Kim, K. S. Kumar, M. E. Schulze, K. Isakovich, G. W. Dodson, K. W. Dow, M. Farkhondeh, S. Kowalski, M. S. Lubell, J. Bellanca, M. Goodman, S. Patch, Richard Wilson, G. D. Cates, S. Dhawan, T. J. Gay, V. W. Hughes, A. Magnon, R. Michaels, and H. R. Schaefer. Measurement of parity violation in the elastic scattering of polarized electrons from  $^{12}\text{C}$ . *Phys. Rev. Lett.*, 65:694–697, Aug 1990. doi: 10.1103/PhysRevLett.65.694. URL <https://link.aps.org/doi/10.1103/PhysRevLett.65.694>.
- [5] W. Heil, J. Ahrens, H.G. Andresen, A. Bornheimer, D. Conrath, K.-J. Dietz, W. Gasteyer, H.-J. Gessinger, W. Hartmann, J. Jethwa, H.-J. Kluge, H. Kessler, T. Kettner, L. Koch, F. Neugebauer, R. Neuhausen, E.W. Otten, E. Reichert, F.P. Schäfer, and B. Wagner. Improved limits on the weak, neutral, hadronic axial vector coupling constants from quasielastic scattering of polarized electrons. *Nuclear Physics B*, 327(1):1–31, 1989. ISSN 0550-3213. doi: [https://doi.org/10.1016/0550-3213\(89\)90284-8](https://doi.org/10.1016/0550-3213(89)90284-8). URL <https://www.sciencedirect.com/science/article/pii/0550321389902848>.
- [6] Sample at mit-bates. URL <https://bateslab.mit.edu/projects/sample>.

- [7] The g0 experiment. URL <http://research.npl.illinois.edu/exp/G0/publicWeb/>.
- [8] Happex collaboration. URL <https://hallaweb.jlab.org/experiment/HAPPEX/>.
- [9] A4 collaboration at mami. URL <https://www.blogs.uni-mainz.de/fb08-ag-maas/a4-collaboration-at-mami/>.
- [10] P. L. Anthony, R. G. Arnold, C. Arroyo, K. Bega, J. Biesiada, P. E. Bosted, G. Bower, J. Cahoon, R. Carr, G. D. Cates, J.-P. Chen, E. Chudakov, M. Cooke, P. Decowski, A. Deur, W. Emam, R. Erickson, T. Fieguth, C. Field, J. Gao, M. Gary, K. Gustafsson, R. S. Hicks, R. Holmes, E. W. Hughes, T. B. Humensky, G. M. Jones, L. J. Kaufman, L. Keller, Yu. G. Kolomensky, K. S. Kumar, P. LaViolette, D. Lhuillier, R. M. Lombard-Nelsen, Z. Marshall, P. Mastromarino, R. D. McKeown, R. Michaels, J. Niedziela, M. Olson, K. D. Paschke, G. A. Peterson, R. Pithan, D. Relyea, S. E. Rock, O. Saxton, J. Singh, P. A. Souder, Z. M. Szalata, J. Turner, B. Tweedie, A. Vacheret, D. Walz, T. Weber, J. Weisend, M. Woods, and I. Younus. Precision measurement of the weak mixing angle in möller scattering. *Phys. Rev. Lett.*, 95:081601, Aug 2005. doi: 10.1103/PhysRevLett.95.081601. URL <https://link.aps.org/doi/10.1103/PhysRevLett.95.081601>.
- [11] D. Androic, D. S. Armstrong, A. Asaturyan, T. Averett, J. Balewski, J. Beaufait, R. S. Beminiwattha, J. Benesch, F. Benmokhtar, J. Birchall, R. D. Carlini, G. D. Cates, J. C. Cornejo, S. Covrig, M. M. Dalton, C. A. Davis, W. Deconinck, J. Diefenbach, J. F. Dowd, J. A. Dunne, D. Dutta, W. S. Duvall, M. Elaasar, W. R. Falk, J. M. Finn, T. Forest, D. Gaskell, M. T. W. Gericke, J. Grames, V. M. Gray, K. Grimm, F. Guo, J. R. Hoskins, K. Johnston, D. Jones, M. Jones, R. Jones, M. Kargantoulakis, P. M. King, E. Korkmaz, S. Kowalski, J. Leacock, J. Leckey, A. R. Lee, J. H. Lee, L. Lee, S. MacEwan, D. Mack, J. A. Magee, R. Mahurin, J. Mammei, J. W. Martin, M. J. McHugh, D. Meekins, J. Mei, R. Michaels, A. Micherdzinska, A. Mkrtchyan, H. Mkrtchyan, N. Morgan, K. E. Myers, A. Narayan, L. Z. Ndukum, V. Nelyubin, Nuruzzaman, W. T. H. van Oers, A. K. Opper, S. A. Page, J. Pan, K. D. Paschke, S. K. Phillips, M. L. Pitt, M. Poelker, J. F. Rajotte, W. D. Ramsay, J. Roche, B. Sawatzky, T. Seva, M. H. Shabestari, R. Silwal, N. Simicevic, G. R. Smith, P. Solvignon, D. T. Spayde, A. Subedi, R. Subedi, R. Suleiman, V. Tadevosyan, W. A. Tobias, V. Tvaskis, B. Waidyawansa, P. Wang, S. P. Wells, S. A. Wood, S. Yang, R. D. Young, and S. Zhamkochyan. First determination of the weak charge of the proton. *Phys. Rev. Lett.*, 111:141803, Oct 2013. doi: 10.1103/PhysRevLett.111.141803. URL <https://link.aps.org/doi/10.1103/PhysRevLett.111.141803>.
- [12] D. Wang, K. Pan, R. Subedi, X. Deng, Z. Ahmed, K. Allada, K. A. Aniol, D. S. Armstrong, J. Arrington, V. Bellini, R. Beminiwattha, J. Benesch, F. Benmokhtar, A. Camsonne, M. Canan, G. D. Cates, J.-P. Chen, E. Chudakov, E. Cisbani, M. M. Dalton, C. W. de Jager, R. De Leo, W. Deconinck, A. Deur, C. Dutta, L. El Fassi, D. Flay, G. B. Franklin, M. Friend, S. Frullani, F. Garibaldi, A. Giusa,

- A. Glamazdin, S. Golge, K. Grimm, K. Hafidi, O. Hansen, D. W. Higinbotham, R. Holmes, T. Holmstrom, R. J. Holt, J. Huang, C. E. Hyde, C. M. Jen, D. Jones, H. Kang, P. King, S. Kowalski, K. S. Kumar, J. H. Lee, J. J. LeRose, N. Liyanage, E. Long, D. McNulty, D. J. Margaziotis, F. Meddi, D. G. Meekins, L. Mercado, Z.-E. Meziani, R. Michaels, M. Mihovilovic, N. Muangma, K. E. Myers, S. Nanda, A. Narayan, V. Nelyubin, Nuruzzaman, Y. Oh, D. Parno, K. D. Paschke, S. K. Phillips, X. Qian, Y. Qiang, B. Quinn, A. Rakhman, P. E. Reimer, K. Rider, S. Riordan, J. Roche, J. Rubin, G. Russo, K. Saenboonruang, A. Saha, B. Sawatzky, A. Shahinyan, R. Silwal, S. Sirca, P. A. Souder, R. Suleiman, V. Sulkosky, C. M. Sutera, W. A. Tobias, G. M. Urciuoli, B. Waidyawansa, B. Wojtsekhowski, L. Ye, B. Zhao, and X. Zheng. Measurements of parity-violating asymmetries in electron-deuteron scattering in the nucleon resonance region. *Phys. Rev. Lett.*, 111:082501, Aug 2013. doi: 10.1103/PhysRevLett.111.082501. URL <https://link.aps.org/doi/10.1103/PhysRevLett.111.082501>.
- [13] Solid. URL <https://solid.jlab.org/>.
- [14] Moller. URL [https://moller.jlab.org/moller\\_root/](https://moller.jlab.org/moller_root/).
- [15] Mesa-p2. URL <https://www.blogs.uni-mainz.de/fb08p2/>.
- [16] The Hall A Collaboration. Jefferson lab hall a standard equipment manual. Jun 2019. URL <https://hallaweb.jlab.org/github/halla-osp/version/Standard-Equipment-Manual.pdf>.
- [17] L.S. Cardman. Polarized electron sources for the 1990's. *Nuclear Physics A*, 546(1):317–336, 1992. ISSN 0375-9474. doi: [https://doi.org/10.1016/0375-9474\(92\)90518-O](https://doi.org/10.1016/0375-9474(92)90518-O). URL <https://www.sciencedirect.com/science/article/pii/0375947492905180>.
- [18] Philip A. Adderley, Steven Covert, Joseph Grames, John Hansknecht, Kenneth Surles-Law, Danny Machie, Bernard Poelker, Marcy L. Stutzman, Riad Suleiman, and James Clark. Photoinjector improvements at cebaf in support of parity violation experiments. *Nuovo Cimento C*, 35(4), 7 2012. ISSN 1826-9885.
- [19] J. M. Grames, C. K. Sinclair, M. Poelker, X. Roca-Maza, M. L. Stutzman, R. Suleiman, Md. A. Mamun, M. McHugh, D. Moser, J. Hansknecht, B. Moffit, and T. J. Gay. High precision 5 mev mott polarimeter. *Phys. Rev. C*, 102:015501, Jul 2020. doi: 10.1103/PhysRevC.102.015501. URL <https://link.aps.org/doi/10.1103/PhysRevC.102.015501>.
- [20] J. M. Grames, C. K. Sinclair, J. Mitchell, E. Chudakov, H. Fenker, A. Freyberger, D. W. Higinbotham, M. Poelker, M. Steigerwald, M. Tiefenback, C. Cavata, S. Escoffier, F. Marie, T. Pussieux, P. Vernin, S. Danagoulian, V. Dharmawardane, R. Fatemi, K. Joo, M. Zeier, V. Gorbenko, R. Nasseripour, B. Raue, R. Suleiman, and B. Zihlmann. Unique electron polarimeter analyzing power

comparison and precision spin-based energy measurement. *Phys. Rev. ST Accel. Beams*, 7:042802, Apr 2004. doi: 10.1103/PhysRevSTAB.7.042802. URL <https://link.aps.org/doi/10.1103/PhysRevSTAB.7.042802>.

- [21] J.-C. Denard, A. Saha, and G. Laveissiere. High accuracy beam current monitor system for cebaf's experimental hall a. In *PACS2001. Proceedings of the 2001 Particle Accelerator Conference (Cat. No.01CH37268)*, volume 3, pages 2326–2328 vol.3, 2001. doi: 10.1109/PAC.2001.987367.
- [22] Hall a images. URL <https://www.jlab.org/help/Ghelp/halla3d.html>.
- [23] K.G Fissum, W Bertozzi, J.P Chen, D Dale, H.C Fenker, J Gao, A Gavalya, S Gilad, C.R Leathers, N Liyanage, R.O Michaels, E.A.J.M Offermann, J Segal, J.A Templon, R Wechsler, B Wojtsekowski, and J Zhao. Vertical drift chambers for the hall a high-resolution spectrometers at jefferson lab. *Nuclear Instruments and Methods in Physics Research Section A: Accelerators, Spectrometers, Detectors and Associated Equipment*, 474(2):108–131, 2001. ISSN 0168-9002. doi: [https://doi.org/10.1016/S0168-9002\(01\)00875-0](https://doi.org/10.1016/S0168-9002(01)00875-0). URL <https://www.sciencedirect.com/science/article/pii/S0168900201008750>.
- [24] H. De Vries, C.W. De Jager, and C. De Vries. Nuclear charge-density-distribution parameters from elastic electron scattering. *Atomic Data and Nuclear Data Tables*, 36(3):495–536, 1987. ISSN 0092-640X. doi: [https://doi.org/10.1016/0092-640X\(87\)90013-1](https://doi.org/10.1016/0092-640X(87)90013-1). URL <https://www.sciencedirect.com/science/article/pii/0092640X87900131>.
- [25] I. Angeli. A consistent set of nuclear rms charge radii: properties of the radius surface  $r(n,z)$ . *Atomic Data and Nuclear Data Tables*, 87(2):185–206, 2004. ISSN 0092-640X. doi: <https://doi.org/10.1016/j.adt.2004.04.002>. URL <https://www.sciencedirect.com/science/article/pii/S0092640X04000166>.
- [26] L. C. Maximon and R. A. Schrack. The form factor of the Fermi model spatial distribution. *J. Res. Natl. Bur. Stand. B*, 70(1), 1966. doi: 10.6028/jres.070b.007.
- [27] B. G. Todd-Rutel and J. Piekarewicz. Neutron-rich nuclei and neutron stars: A new accurately calibrated interaction for the study of neutron-rich matter. *Phys. Rev. Lett.*, 95:122501, Sep 2005. doi: 10.1103/PhysRevLett.95.122501. URL <https://link.aps.org/doi/10.1103/PhysRevLett.95.122501>.
- [28] J. M. Lattimer and M. Prakash. Neutron star structure and the equation of state. *The Astrophysical Journal*, 550(1):426–442, mar 2001. doi: 10.1086/319702. URL <https://doi.org/10.1086/319702>.
- [29] B. Alex Brown. Neutron radii in nuclei and the neutron equation of state. *Phys. Rev. Lett.*, 85(0):5296–5299, Dec 2000. doi: 10.1103/PhysRevLett.85.5296. URL <https://link.aps.org/doi/10.1103/PhysRevLett.85.5296>.

- [30] M. Goldhaber, L. Grodzins, and A. W. Sunyar. Helicity of neutrinos. *Phys. Rev.*, 109:1015–1017, Feb 1958. doi: 10.1103/PhysRev.109.1015. URL <https://link.aps.org/doi/10.1103/PhysRev.109.1015>.
- [31] F.J. Hasert, S. Kabe, W. Krenz, J. Von Krogh, D. Lanske, J. Morfin, K. Schultze, H. Weerts, G. Bertrand-Coremans, J. Sacton, W. Van Doninck, P. Vilain, R. Baldi, U. Camerini, D.C. Cundy, I. Danilchenko, W.F. Fry, D. Haidt, S. Natali, P. Musset, B. Osculati, R. Palmer, J.B.M. Pattison, D.H. Perkins, A. Pullia, A. Rousset, W. Venus, H. Wachsmuth, V. Brisson, B. Degrange, M. Haguenuuer, L. Kluberg, U. Nguyen-Khac, P. Petiau, E. Bellotti, S. Bonetti, D. Cavalli, C. Conta, E. Fiorini, M. Rollier, B. Aubert, D. Blum, L.M. Chouinet, P. Heusse, A. Lagarrigue, A.M. Lutz, A. Orkin-Lecourtois, J.P. Vialle, F.W. Bullock, M.J. Esten, T.W. Jones, J. McKenzie, A.G. Michette, G. Myatt, and W.G. Scott. Observation of neutrino-like interactions without muon or electron in the gargamelle neutrino experiment. *Nuclear Physics B*, 73(1):1–22, 1974. ISSN 0550-3213. doi: [https://doi.org/10.1016/0550-3213\(74\)90038-8](https://doi.org/10.1016/0550-3213(74)90038-8). URL <https://www.sciencedirect.com/science/article/pii/0550321374900388>.
- [32] C. S. Wu, E. Ambler, R. W. Hayward, D. D. Hoppes, and R. P. Hudson. Experimental test of parity conservation in beta decay. *Phys. Rev.*, 105:1413–1415, Feb 1957. doi: 10.1103/PhysRev.105.1413. URL <https://link.aps.org/doi/10.1103/PhysRev.105.1413>.
- [33] B. Zel'dovich Ya. Parity nonconservation in the first order in the weak-interaction constant in electron scattering and other effects. *Journal of Experimental and Theoretical Physics (USSR)*, 36:964–966, March 1959. URL [http://jetp.ras.ru/cgi-bin/dn/e\\_009\\_03\\_0682.pdf](http://jetp.ras.ru/cgi-bin/dn/e_009_03_0682.pdf).
- [34] X. Roca-Maza, M. Centelles, X. Viñas, and M. Warda. Neutron skin of  $^{208}\text{Pb}$ , nuclear symmetry energy, and the parity radius experiment. *Phys. Rev. Lett.*, 106:252501, Jun 2011. doi: 10.1103/PhysRevLett.106.252501. URL <https://link.aps.org/doi/10.1103/PhysRevLett.106.252501>.
- [35] Prex-ii proposal.
- [36] Crex proposal.
- [37] E. L. Garwin D. T. Pierce and H. C. Siegmann. *Helv. Phys. Acta*, 47:393, 1974.
- [38] G. Lampel and C. Weisbuch. Proposal for an efficient source of polarized photo-electrons from semiconductors. *Solid State Communications*, 16(7):877–880, 1975. ISSN 0038-1098. doi: [https://doi.org/10.1016/0038-1098\(75\)90884-4](https://doi.org/10.1016/0038-1098(75)90884-4). URL <https://www.sciencedirect.com/science/article/pii/0038109875908844>.
- [39] Noah Sherman. Coulomb scattering of relativistic electrons by point nuclei. *Phys. Rev.*, 103:1601–1607, Sep 1956. doi: 10.1103/PhysRev.103.1601. URL <https://link.aps.org/doi/10.1103/PhysRev.103.1601>.

- [40] S. J. Pollock, E. N. Fortson, and L. Wilets. Atomic parity nonconservation: Electroweak parameters and nuclear structure. *Phys. Rev. C*, 46:2587–2600, Dec 1992. doi: 10.1103/PhysRevC.46.2587. URL <https://link.aps.org/doi/10.1103/PhysRevC.46.2587>.

# Appendix A

## Symmetry Energy

$$E_k = C(N^{5/3} + Z^{5/3})$$

Let:  $A = N + Z$  and  $B = N - Z$ , then we have  $N + \frac{A+B}{2}$ ,  $Z = \frac{A-B}{2}$  and  $B \ll A$ :

$$\begin{aligned} E_k &= C \left( \left( \frac{A+B}{2} \right)^{5/3} + \left( \frac{A-B}{2} \right)^{5/3} \right) \\ &= C \left( \frac{A}{2} \right)^{5/3} \left( \left( 1 + \frac{B}{A} \right)^{5/3} + \left( 1 - \frac{B}{A} \right)^{5/3} \right) \\ &= C \left( \frac{A}{2} \right)^{5/3} \left( \left( 1 + \frac{5}{3} \frac{B}{A} + \frac{1}{2!} \frac{5}{3} \frac{2}{3} \left( \frac{B}{A} \right)^2 + \dots \right) + \left( 1 + \frac{5}{3} \left( -\frac{B}{A} \right) + \frac{1}{2!} \frac{5}{3} \frac{2}{3} \left( -\frac{B}{A} \right)^2 + \dots \right) \right) \\ &= 2^{-2/3} C \left( A^{5/3} + \frac{5}{9} \frac{B^2}{A^{1/3}} \right) + O(\frac{B^4}{A^{7/3}}) \\ &= 2^{-2/3} C \left( A^{5/3} + \frac{5}{9} \frac{(N-Z)^2}{A^{1/3}} \right) + O((N-Z)^4) \end{aligned}$$

### A.1 Resource

- hall A equipment: <https://hallaweb.jlab.org/equipment/>